Chem Soc Rev

Chemical Society Reviews

rsc.li/chem-soc-rev
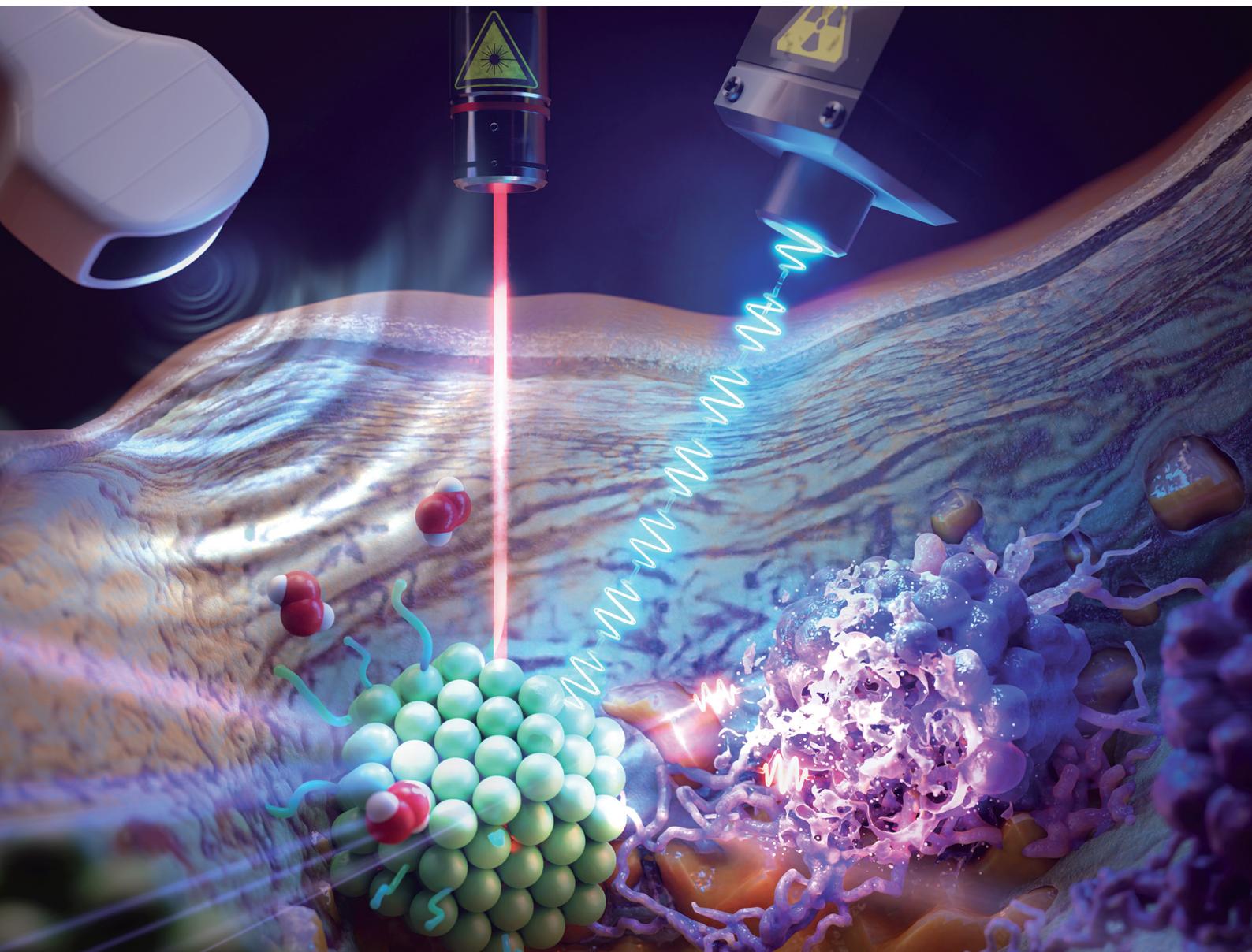
ROYAL SOCIETY
OF **CHEMISTRY**

REVIEW ARTICLE
Chung Yin Tsang and Yong Zhang
Nanomaterials for light-mediated therapeutics in deep tissue

Check for updates

Nanomaterials for light-mediated therapeutics in deep tissue

Chung Yin Tsang [ID] [a] and Yong Zhang [ID] *[b]

Light-mediated therapeutics, including photodynamic therapy, photothermal therapy and light-triggered drug delivery, have been widely studied due to their high specificity and effective therapy. However, conventional light-mediated therapies usually depend on the activation of light-sensitive molecules with UV or visible light, which have poor penetration in biological tissues. Over the past decade, efforts have been made to engineer nanosystems that can generate luminescence through excitation with near-infrared (NIR) light, ultrasound or X-ray. Certain nanosystems can even carry out light-mediated therapy through chemiluminescence, eliminating the need for external activation. Compared to UV or visible light, these 4 excitation modes penetrate more deeply into biological tissues, triggering light-mediated therapy in deeper tissues. In this review, we systematically report the design and mechanisms of different luminescent nanosystems excited by the 4 excitation sources, methods to enhance the generated luminescence, and recent applications of such nanosystems in deep tissue light-mediated therapeutics.

1. Introduction

Light-mediated therapeutics have emerged significantly over the past few decades due to their specificity, non-invasiveness and high therapeutic efficacy. Typically, a photosensitive molecule is delivered to the target tissue, while light is directed onto the target tissue to activate the molecule for specific therapy. For example, photodynamic therapy involves the light activation of a photosensitizer delivered into the target tissue. Upon activation, reactive oxygen species (ROS) such as singlet oxygen ($^1O_2$) or hydroxyl radicals ($^\bullet OH$) are generated, damaging the target cells.[1] However, most photosensitizers are only activated by UV or visible light.[2] Another well-studied light-mediated therapy involves light-triggered drug release, which generally involves nanoparticles conjugated with drug molecules through photocleavable linkers or bonds. Light in the UV/visible spectrum usually has enough energy to cleave such linkers and release the drug into the target tissue.[3] Light-based therapeutics ensure the activation of nanomaterials only in the target tissue, while having minimal effects in other healthy tissues.

However, light in the UV/visible spectrum exhibits poor penetration of just a few millimetres in biological tissue and would not be suitable for deep tissue light-mediated therapy.[4]

[a] *Department of Biomedical Engineering, College of Design and Engineering, National University of Singapore, Singapore 117583, Singapore. E-mail: e0974156@u.nus.edu*

[b] *Department of Biomedical Engineering, The City University of Hong Kong, 83 Tat Chee Avenue, Kowloon, Hong Kong. E-mail: yozhang@cityu.edu.hk*

Chung Yin Tsang completed his bachelor's degree in biomedical engineering from the Chinese University of Hong Kong in 2022. Currently, he is pursuing a PhD degree in biomedical engineering at National University of Singapore (NUS). His research focuses on the design, synthesis and therapeutic applications of luminescent nanomaterials.

Chung Yin Tsang

Yong Zhang is currently the Chair Professor of Biomedical Engineering and Head of the Department of Biomedical Engineering at City University of Hong Kong. Professor Zhang has authored over 300 peer-reviewed research papers in international journals. His current research interests include nanobiophotonics, nanomedicine, and microfluidic devices.

Yong Zhang

Therefore, recently, certain nanosystems have been engineered to produce UV/visible light upon activation with excitation sources that exhibit deeper penetration in biological tissues. This enables the implementation of light-mediated therapies in deep tissue.

Near-infrared (NIR) light, possessing a tissue penetration depth of 1–2 cm, can produce visible light through upconversion processes through excitation with NIR-I (700–1000 nm) or NIR-II light (1000–1700 nm).[5–7] In addition, NIR-II light can also be generated in other NIR-excited nanosystems through downconversion processes.[8] The visible light produced is usually utilised for therapeutic purposes, while the NIR-II light serves as an imaging modality given its lower tissue attenuation.[6,9] Ultrasound, with a tissue penetration depth exceeding 10 cm, could also activate certain nanomaterials to produce light in the visible range.[10] Ultrasound generates luminescence either through sonoluminescence (cavitation of bubbles in a liquid medium) or through the deformation of mechanoluminescent nanomaterials.[11,12] X-rays have the deepest penetration depth compared to NIR and ultrasound, with almost unlimited penetration depth in biological tissue.[13] More importantly, X-rays can pass through very dense body structures like bone, enabling therapies in organs protected by bone such as the brain.[14] X-rays also carry sufficient energy to cause direct band-to-band excitation in many nanosystems, resulting in the generation of strong light in the UV/visible range and the activation of most photosensitive molecules. Finally, certain nanomaterials could enhance chemiluminescence produced from chemical reactions without the need for external activation.[15] This allows the therapy to be carried out in deep tissue regions without considering light scattering.

Therefore, it is of great essence that we summarise the strategies reported that enable the activation of light-mediated therapies in deep tissue. In this review, we systematically discuss the design and mechanism of different nanomaterials that enable emission of chemiluminescence, NIR-, X-ray- and ultrasound-excited luminescence (Fig. 1). In addition, we will also report methods for enhancing luminescence intensity, applications of the nanosystems in deep tissue therapy, as well as the comparison between strengths and weaknesses of the 4 excitation modes.

2. Chemiluminescence

Chemiluminescence is the phenomenon characterized by the generation of light through chemiexcitation occurring within a chemical reaction, without external light excitation.[16] By harnessing the light emission generated through chemiluminescent reactions, it becomes possible to overcome the limitations of traditional light-mediated therapy with UV/visible light sources, such as low tissue penetration and potential damage to surrounding tissues. There are 2 major mechanisms of chemiluminescence: direct chemiluminescence and indirect chemiluminescence.[17]
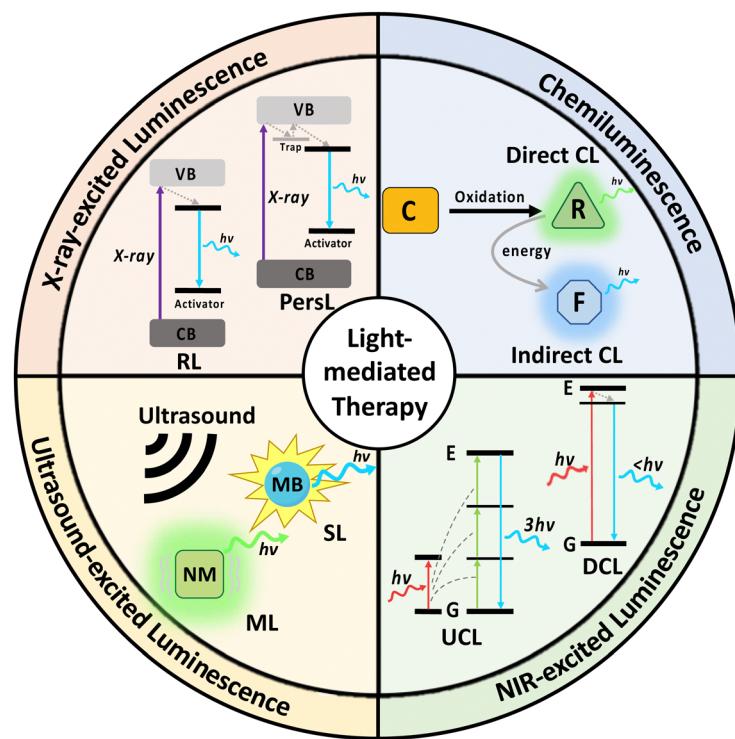
Fig. 1 Schematic illustration of the different mechanisms of light generation with chemi-excitation, NIR-excitation, ultrasound-excitation and X-ray-excitation that support deep-tissue light-mediated therapeutics. (C: chemiluminophore; CL: chemiluminescence; DCL: downconversion luminescence; F: fluorophore; MB: microbubble; ML: mechanoluminescence; NM: nanomaterial; PersL: persistent luminescence; R: radical; RL: radioluminescence; SL: sonoluminescence; and UCL: upconversion luminescence).

This journal is © The Royal Society of Chemistry 2024

Chem. Soc. Rev., 2024, **53**, 2898–2931 | **2899**
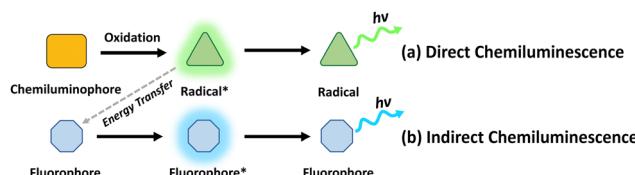
Fig. 2 Schematic illustrations of the mechanisms of (a) direct chemiluminescence and (b) indirect chemiluminescence.

Direct chemiluminescence refers to the emission of light directly from the excited state of a chemical species formed during a chemical reaction (Fig. 2a). Examples of direct chemiluminescence involve the oxidation of chemiluminescent substrates (C), such as luminol, or its derivatives. They can be directly oxidized by reactive oxygen species, such as superoxide anions (O_2^-) and hydrogen peroxide (H_2O_2), resulting in the generation of excited radicals (R^*). These radicals emit photons while returning to the ground state (R). A classic example of direct chemiluminescence is the reaction between luminol and hydrogen peroxide, producing light at 440 nm.[18] In indirect chemiluminescence, the excited radicals do not return to the ground state directly. Instead, they interact with a nearby auxiliary species, such as fluorophores (F), to generate light. Indirect chemiluminescence relies on energy transfer processes between the chemiexcited species and the luminophore, normally achieved through chemiluminescence resonance energy transfer (CRET). Typical examples involve the oxidation of peroxyoxalate esters, certain ruthenium complexes or dioxetanes, generating high-energy radicals that can excite a nearby luminophore.

Traditionally, chemiluminescence occurs randomly as a result of the interaction between reactants at low concentration. By leveraging nanomaterials, we can control the rate, location and enhance the intensity of chemiluminescence for therapeutic purposes. Nanomaterials, such as metal nanoparticles, quantum dots, and organic nanomaterials play important roles in the delivery and enhancement of chemiluminescence for deep tissue applications. Nanomaterials with high loading capacity and surface tunability, such as mesoporous silica nanoparticles (MSNs) or polymers, facilitate the targeted delivery of chemiluminophores or catalysts into deep tissues.[19,20] On the other hand, other nanomaterials actively participate in chemiluminescence reactions by catalysing the necessary reactions or acting as a chemiluminophore.[21,22] Through this strategic approach, nanomaterials pave the way for light generation in deep tissue regions for light-based therapeutics.

2.1 Nanomaterials as delivery agents

To generate chemiluminescence in specific areas, nanomaterials have been utilised as delivery agents of chemiluminophores, oxidizers, or catalysts that catalyse the chemiluminescence reaction. This enables control over the location of chemiluminescence.

Guo *et al.* encapsulated luminol with the photosensitiser chlorin e6 (Ce6) in poly(ethylene glycol).[18] Following the reaction between luminol and H_2O_2, light emission occurs at 440 nm, which overlaps with the absorption spectra of Ce6

for the initiation of photodynamic therapy. Apart from delivering chemiluminophores, delivering oxidizers could also enhance chemiluminescence. Certain Fe^{3+}-containing nanomaterials could generate H_2O_2 endogenously through the Fenton reaction, which increases the rate of chemiluminophore oxidation. For example, the $MnFe_2O_4$ core was encapsulated in the Zr-based MOF, where Fe^{3+} acted as a catalyst to generate H_2O_2 *via* the Fenton reaction.[23] H_2O_2 then reacted with the encapsulated luminol, resulting in enhanced chemiluminescence, while the Zr-based MOF acted as a photosensitiser. The system exhibited significant enhancement in chemiluminescence and high anti-tumour efficacy *in vivo*.

Catalysts for chemiluminescence reactions can also be delivered by nanomaterials to enhance their catalytic activity. Ren *et al.* conjugated hemin, a catalyst of luminol–H_2O_2 reaction, onto polymer dots (hemin–Pdots), resulting in a 700-fold enhancement in chemiluminescence (CL) intensity and 20-fold prolonged emission.[24] The surface of the nanomaterial could be further engineered for targeting. For example, the surface of a PEGylated chemiluminophore could be modified with folic acid (FA), allowing specific binding to cancer cells due to the overexpressed folate receptor (FR).[20]

To ensure specifically targeted chemiluminescence, Cao *et al.* developed hemin–MSN@DNA, incorporating DNA gates onto the pores of mesoporous silica nanoparticles (MSNs) loaded with hemin.[25] Upon degradation of DNA gates by specific bacteria, hemin was released from the pores, enhancing the chemiluminescence signal (Fig. 3a). The authors assessed the CL intensity on *E. coli* and *S. aureus*, and the results revealed a strong correlation between bacterial concentration and CL intensity (Fig. 3b and c), confirming specific chemiluminescence generation. In addition, the DNA gating on the pores of MSNs allows for a hybridization chain reaction on their surface, enabling the formation of a hydrogel coating.[26] This further
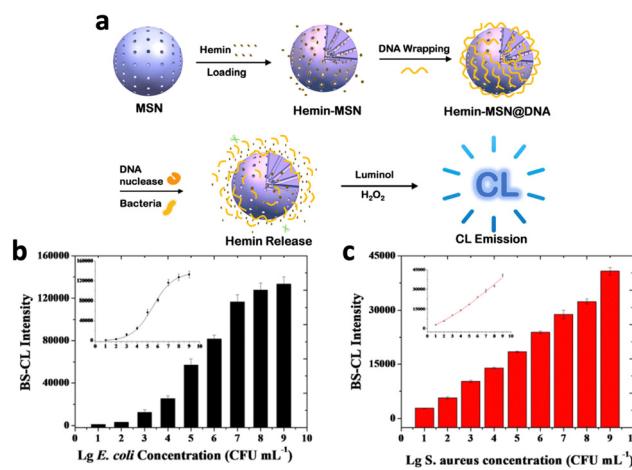
Fig. 3 (a) Schematic representation of the mechanism of chemiluminescence generation from hemin–MSN@DNA. Correlation between chemiluminescence intensity of hemin-MSN@DNA and (b) *E. coli* and (c) *S. aureus* concentration. Reproduced with permission from ref. 25. Copyright 2019, American Chemical Society.

improved stability and loading capacity compared to traditional gated mesoporous silica systems.

2.2 Nanomaterials as catalysts for chemiluminescence enhancement

Instead of delivering the catalyst to the chemiluminescence reaction site, many metal-based nanomaterials offer intrinsic catalytic properties. In this section, we will discuss the nanomaterials that offer catalytic properties for different chemiluminescence reactions, including metal-based nanomaterials, organic nanomaterials and semiconducting nanomaterials.

2.2.1 Metal-based nanomaterials. Gold nanoparticles (Au NPs) were first reported by Liu *et al.* as catalysts for the luminol–H_2O_2 reaction, where gold nanoparticles of around 38 nm in diameter enhanced the chemiluminescence intensity of the luminol–H_2O_2 reaction by 10 times.[15] Basically, AuNPs catalyse the breaking of the O–O bond in H_2O_2, resulting in the formation of double hydroxyl radicals ($^\bullet$OH) as intermediates. The $^\bullet$OH radicals react with luminol anions and HO_2^- to facilitate the formation of luminol radicals ($L^{\bullet -}$) and superoxide radical anions ($O_2^{\bullet -}$), resulting in the formation of an unstable endoperoxide and subsequent 3-aminophthalate* (3-APA*). When the excited-state 3-APA returned to the ground state, an enhanced CL was observed. Following the discovery of catalytic properties in gold nanoparticles, extensive efforts have been undertaken to enhance and optimize their catalytic performance. For example, Au NPs modified with ethandiamine exhibited a fivefold improvement in the catalytic activity of Au NPs, due to the enhanced interaction with reactive oxygen species, resulting in the generation of singlet oxygen ($^1O_2$).[27] The negative anions also attracted endogenous luminol anions, which were readily oxidised by the $^1O_2$ on the surface of Au NP, leading to enhanced chemiluminescence. *P*-iodophenol (PIP)-capped Au NPs further improved CL by 29-fold due to elevated production of $O_2^{\bullet -}$ radicals, $^1O_2$, and H_2O_2 for enhanced oxidation of luminol.[28] Different morphologies of gold nanoparticles were also studied. It was found that gold nanostars are more beneficial for catalysing CL due to their sharp branches, which exhibit high electron density at the tips for enhanced catalytic activity.[29] Gold nanoflowers are also beneficial for catalysis, since they exhibit a larger specific surface area, providing more active sites for catalytic reactions. Additionally, they generate a stronger local electromagnetic field enhancement effect, further promoting the catalytic process.[30]

Chemiluminescence could also be increased through the aggregation of catalysts. For example, chemiluminescence was enhanced by aggregating Au NPs with complex DNA networks (CDNs).[21] A hairpin (H_1) exposed to the CDN is cleaved by a specific DNAzyme (BB') in the network, forming a single-stranded hairpin (H_{1-1}). Simultaneously, Au NPs that are tagged with nucleic acids complementary to H_{1-1}(p,q) would be assembled by H_{1-1} to form an aggregated state (Fig. 4a). At a higher DNAzyme (BB') level, the absorption band of the CDN decreased more quickly, indicating more efficient Au NP aggregation (Fig. 4b and c). In addition, aggregated Au NPs also produced stronger chemiluminescence compared to the un-aggregated ones
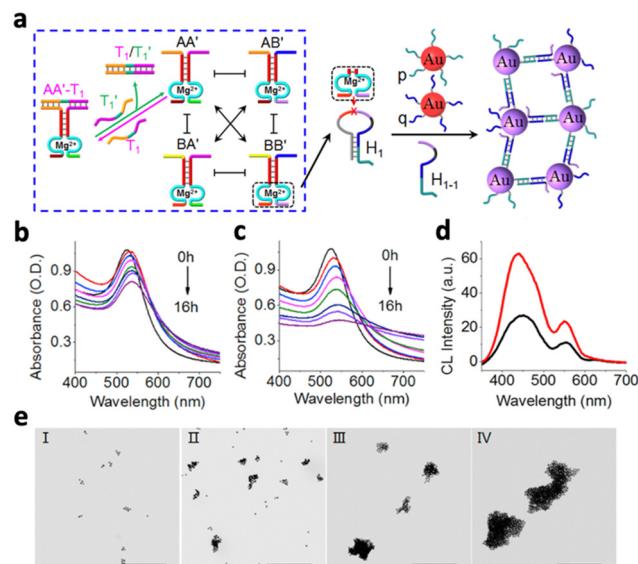
Fig. 4 (a) Schematic illustration of the time-dependent aggregation of Au NPs. Time-dependent absorbance spectra of the complex DNA network with (b) low concentration of BB' DNAzyme and (c) high concentration of BB' DNAzyme. (d) Chemiluminescence emission spectra generated by the control (black curve) and the aggregated Au NPs (red curve). (e) TEM image corresponding to the aggregates of the Au NPs generated by CDN with a low BB' level after 4 h (panel I) and 8 h (panel II) of aggregation and by CDN with a high BB' level after 4 h (panel III) and 8 h (panel IV) of aggregation, respectively. Reproduced with permission from ref. 21. Copyright 2018, American Chemical Society.

(Fig. 4d). Finally, the TEM image validated the stronger aggregation of Au NPs in the CDN with a higher BB' level (Fig. 4eIII and IV) as compared to a lower BB' level (Fig. 4eI and II).

Silver and platinum nanoparticles also enhance the luminol–H_2O_2 reaction, with a similar catalytic mechanism to Au NPs.[31,32] It was also found that the catalytic activity of silver nanoparticles (AgNPs) increased with the aggregation of small Ag NPs, due to the increase in the electron density in the Ag NPs' conduction bands.[33] Other than gold, silver and platinum, copper(II) compounds like $CuFe_2O_4$ nanospheres could also act as efficient catalysts for luminol-based chemiluminescence reactions.[34] This is because Cu^{2+} catalyses the formation of CL intermediates such as superoxide radicals ($O_2^{\bullet -}$) and hydroxyl radicals ($^\bullet$OH).

Since metal–organic frameworks (MOFs) provide a high surface area for catalysis, constructing MOFs with catalytic metal ions would be more effective in enhancing chemiluminescence. For example, metal–organic framework (MOF) nanoparticles composed of Zr^{4+} and Cu^{2+} ions bridged by 2,2′-bipyridine-5,5′-dicarboxylic acid ligands provided almost 20-fold improvement in catalytic activity compared to Cu^{2+} ions alone.[35] In addition, Fe-based MOFs modified with AuNPs showed around 110-fold enhancement in CL intensity compared to AuNPs alone.[36]

2.2.2 Organic nanomaterials. Organic nanomaterials could also catalyse chemiluminescence reactions through the generation of radicals. For example, layered double hydroxides (LDHs) could catalyse the TCPO–H_2O_2 system to produce enhanced

This journal is © The Royal Society of Chemistry 2024

Chem. Soc. Rev., 2024, **53**, 2898–2931 | **2901**

CL.[37] LDHs accelerated the generation of OOH radicals, which promoted the formation of a 1,2-dioxetanedione intermediate and 2,4,6-trichlorophenol, resulting in the emission of CL.

Instead of relying on radical generation, certain DNAzymes exhibit peroxidase-like activity and can be applied to catalyse the luminol–H_2O_2 reaction. For example, the microRNA (miRNA)-responsive DNAzyme system could enhance chemiluminescence intensity by 3 fold at 100 pm.[38] The presence of a target microRNA triggered the assembly of the G4 DNAzyme following binding with specific hairpin probes, resulting in the specific catalysis of CL from the luminol–H_2O_2 reaction. However, a G4 DNAzyme has limited stability, as it is susceptible to many degradation pathways like nuclease attack. Instead of using DNA networks, DNAzymes can be conjugated on the surface of a gold nanoparticle (SNAzymes), protecting them from degradation.[39] The SNAzymes not only displayed an improved resistance to nuclease degradation as compared to the G4 DNAzyme, but also improved the density of DNA on the nanoparticle ($\sim$150 nucleic acids per particle). This eventually showed 100-fold CL signal enhancement compared to 1 molecule of G4 DNAzyme.

2.2.3 Semiconducting nanomaterials. Semiconductors catalyse chemiluminescence through charge separation and production of radicals. A mixture of graphene quantum dots and molybdenum disulphide quantum dots (GQDs/MoS$_2$ QDs) catalysed the rhodamine B (RB)-H_2O_2 reaction, resulting in a 9-fold enhancement.[40] This is due to the charge separation between GQDs and MoS$_2$ QDs, with GQDs becoming p-type doped and MoS$_2$ QDs becoming n-type doped. Hence, RB was oxidized by the holes in GQDs while the electrons in MoS$_2$ QDs reacted with H_2O_2, creating more hydroxyl radicals ($^{\bullet}OH$) responsible for the oxidation of RB.

TGA-capped CdTe quantum dots (QDs) catalysed the luminol–KIO_4 CL system by generating radicals.[41] KIO_4 is stongly oxidizing and injected a hole into the valence band of CdTe QDs, producing $O_2^{\bullet-}$. The presence of a reducer, hydroxide ions (OH^-), injected an electron into the conduction band of CdTe QDs, producing $^{\bullet}OH$. These active oxygen-containing reactant intermediates accelerated the oxidation reaction of luminol and increased CL emission.

2.3 Nanomaterials as chemiluminophores

Certain nanomaterials can absorb energy from various CL systems to emit light. There are 2 major mechanisms: first, the nanomaterial could be injected with electrons and holes by the radicals in the CL system, where the electron–hole combination results in light emission. Otherwise, the nanomaterial accepts energy from excited radicals in the CL system through chemiluminescence resonance energy transfer (CRET).

2.3.1 Electron/hole injection. Some nanomaterials could be injected with electrons or holes by radicals in the CL system, resulting in light emission. For example, oxidizing agents like $K_3Fe(CN)_6$ or $KMnO_4$ injected holes into carbon dots, resulting in the generation of positively-charged carbon dots (C-dot$^{\bullet+}$).[42,43] On the other hand, dissolved oxygen injected electrons into the carbon dots, generating negatively-charged carbon dots (C-dot$^{\bullet-}$). Subsequently, electron–hole recombination gave rise to CL emission at 515 nm or 430 nm when oxidized by $K_3Fe(CN)_6$ or $KMnO_4$, respectively. $^{\bullet}O_2^-$ and $^{\bullet}OH$ radicals resulting from the H_2O_2–IO_4^- system also acted as hole and electron injectors on cobalt and nitrogen co-doped carbon dots (Co,N-CDs) for CL emission at 504 nm.[44]

2.3.2 Chemiluminescence resonance energy transfer (CRET). Certain quantum dots can directly harvest the energy from excited radicals, such as excited singlet oxygen ($^1O_2$)* in the CL system, through chemiluminescence resonance energy transfer (CRET) to emit light. For example, black phosphorus quantum dots (BPQDs) emitted light at 490 nm when incubated with the H_2O_2–$NaHSO_3$ CL system.[22] Moreover, carbon nitrogen quantum dots (CNQDs) emitted at 480 nm in the IO_4^-–H_2O_2 system.[45] Apart from accepting energy from ($^1O_2$)*, carbon dots accepted energy from excited carbon dioxide (CO_2)* in the $NaNO_2$–H_2O_2–carbonate system, emitting light at 500 nm.[46] More recently, it was discovered that doping sulphur on quantum dots could further enhance CL. This is because doping of sulphur into quantum dots can introduce S-related energy levels between π and $\pi^\star$, resulting in efficient emission peaks.[47,48] Sulphur and nitrogen co-doped graphene quantum dots (SN-GQDs) were found to absorb energy from excited oxygen (O_2)* in the H_2O_2–KIO_4 system, resulting in a 200-fold enhancement of CL at 416 nm.[49] SN-GQDs could also improve the CL at 480 nm from the $Mn(\text{IV})$–SO_3^{2-} system by 900-fold through accepting energy from (SO_2)*.[50] Moreover, a polymer with a low band gap (DPAeCNePPV) could also accept the energy from the reaction between bis(2-carbopentyloxy-3,5,6-trichlorophenyl) oxalate (CPPO) and H_2O_2 to emit light at 700 nm.[51] Further doping with BODIPY leads to roughly 50-fold enhancement in CL emission in the system since it bridges the energy gap between the chemiluminescence reaction and DPAeCNePPV.

$NaYF_4$:Yb^{3+}/Er^{3+} nanoparticles, although being widely studied for their light upconversion properties, were shown to be able to absorb the energy from radicals in the $NaHCO_3$–NH_4OH–H_2O_2 CL system and emit light.[52] The reaction between H_2O_2 and $NaHCO_3$ yields reactive species such as $^{\bullet}OH$, $^{\bullet}CO_3^-$, and $^{\bullet}O_2^-$ radicals, normally emitting luminescence at 441, 480, 580 and 634 nm (Fig. 5b). Following incubation with $NaYF_4$:Yb^{3+}/Er^{3+}, Yb^{3+} sensitized the CL emission and transferred energy to the activator ion Er^{3+} (Fig. 5a). Relaxation of Er^{3+} resulted in enhanced CL emissions at 523, 544, and 653 nm, corresponding to the $^2H_{11/2}$–$^4I_{15/2}$, $^4S_{3/2}$–$^4I_{15/2}$, and $^4F_{9/2}$–$^4I_{15/2}$ transitions of Er^{3+} (Fig. 5c). The disappearance of emission peaks from the original CL system indicated efficient energy transfer to $NaYF_4$:Yb^{3+}/Er^{3+}, while CL intensity was enhanced by 334 fold.

2.4 Chemiluminescence-mediated light therapy

The ability of chemiluminescence to generate light endogenously without external light activation made many deep-tissue light-mediated therapies possible, including photodynamic therapy (PDT), photothermal therapy (PTT) and drug delivery. The efficacy of PDT is mainly based on the intensity of CL, which ultimately depends on the intracellular concentration of

2902 | Chem. Soc. Rev., 2024, **53**, 2898–2931

This journal is © The Royal Society of Chemistry 2024
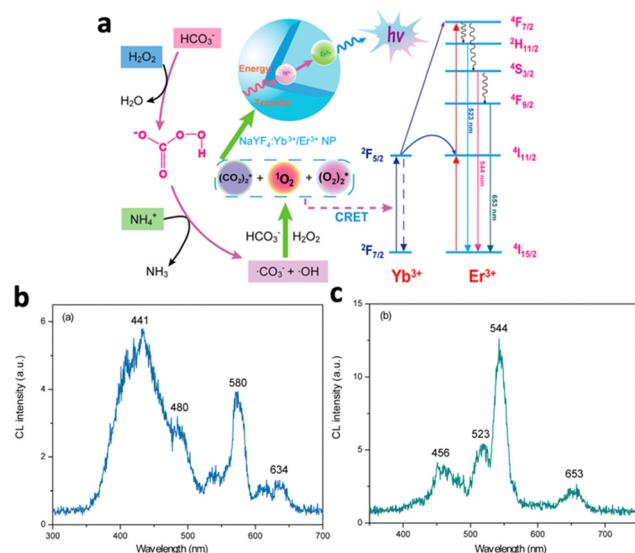
Fig. 5 (a) Schematic illustration of the chemiluminescence mechanism of NaYF$_4$:Yb^{3+},Er^{3+}. Yb^{3+} absorbs energy from radicals and transfers energy to excite Er^{3+}, which eventually relaxes and emits 3 characteristic wavelengths. (b) Emission spectrum of the NaHCO$_3$−NH$_4$OH−H$_2$O$_2$ system. (c) Emission spectrum of the NaHCO$_3$−NH$_4$OH−H$_2$O$_2$ system in the presence of NaYF$_4$:Yb^{3+}/Er^{3+}. Reproduced with permission from ref. 52. Copyright 2012, American Chemical Society.

oxidizers like H$_2$O$_2$. However, intracellular H$_2$O$_2$ is limited and efforts have been undertaken to augment H$_2$O$_2$ levels to enhance the efficacy of PDT. For PTT and drug delivery, chemiluminescence is primarily employed for tracking the localization of photothermal agents or drugs. Therefore, current studies are primarily focused on the development of H$_2$O$_2$-generating nanoystems, nanosystems that emit near-infrared (NIR) chemiluminescence and "turn-on" nanoprobes that exclusively activate within the vicinity of the target tissue.

2.4.1 Photodynamic therapy. Photodynamic therapy involves the delivery of photosensitizers into the target tissue followed by light activation of a specific wavelength, which leads to the generation of reactive oxygen species (ROS), killing the target cells.[1] Taking advantage of the upregulated H$_2$O$_2$ level in tumour cells, the chemiluminophore delivered could generate a stronger CL to activate the co-delivered photosensitizer.

In 2011, Jiang et al. produced a novel PDT system, which leveraged the chemiluminescence reaction between peroxalate ester and H$_2$O$_2$.[53] They prepared polyoxometalate (POM) by encapsulating a peroxalate ester oligomer, a fluorescent dye (rubrene) and photosensitiser TPP within PEG–PCL copolymer micelles. Peroxalate in POMs reacted specifically with the enriched-H$_2$O$_2$ around the tumour area and formed 1,2-dioxetanedione, which emitted light to excite rubrene and TPP. This system was shown to exhibit significant anti-cancer efficacy against C$_6$ and Lovo cells lines in vitro. To ensure more specific tumour targeting, Zhang et al. reported an active-targeting nanosystem (POCL) that uses folate as a targeting ligand.[20] They co-delivered bis(2-carbopentyloxy-3,5,6-trichlorophenyl)oxalate (CPPO) and the photosensitizer tetraphenylporphyrin (TPP), where the CL from the reaction between CPPO

and H$_2$O$_2$ excited TPP, generating ^{1}O$_2$. In vivo studies demonstrated a higher accumulation of this nanosystem in the tumour area, which was 3-fold greater compared to POCL without folate. After 21 days of treatment on tumour-bearing mice, the average tumour weight in the POCL group was significantly reduced by 85% compared to the untreated group.

However, the efficacy of CL-triggered PDT was still limited by the intracellular H$_2$O$_2$ level, which is often less than 100 μm. Hence, Li et al. proposed a CPPO-based nanoplatform (C$_1$@M@C$_2$G) that could self-generate H$_2$O$_2$ to improve treatment efficacy.[54] The nanoplatform consisted of CPPO and the photosensitizer porphyrin encapsulated by Fe-MOF nanoparticles and glucose oxidase (GOD). GOD catalysed the decomposition of glucose from the tumour area, generating H$_2$O$_2$ and gluconic acid, which created a H$_2$O$_2$-rich and acidic microenvironment. A portion of the increased H$_2$O$_2$ underwent Fenton reaction catalysed by Fe in the MOF under a low pH environment, generating oxygen to combat hypoxia in the tumour area (Fig. 6a). The remaining H$_2$O$_2$ reacted with CPPO to produce CL that excited the porphyrin photosensitizers in the MOF, resulting in the generation of ^{1}O$_2$ (Fig. 6a). The incubation of the nanoplatform with more glucose resulted in higher H$_2$O$_2$ production, accompanied by a drop in pH from 6.8 to 2.6 after 10 minutes (Fig. 6b and c). In addition, ^{1}O$_2$ production was enhanced around 2-fold in the presence of glucose at 1 mg mL^{-1}, accompanied by the greatest tumour inhibition compared to the control groups without GOD (Fig. 6d and e). Other than relying on glucose to generate H$_2$O$_2$, a recent study demonstrated the possibility to generate H$_2$O$_2$ by reacting with intracellular water.[55] A nanosystem (mSCCC@SA) combining CaO$_2$, CPPO and the photosensitiser Ce6 was introduced, where CaO$_2$ reacted with intracellular water to generate H$_2$O$_2$ and O$_2$, resulting in stronger CL and enhanced PDT efficacy. This nanosystem reduced the cell viability of HepG2 cells to 40%
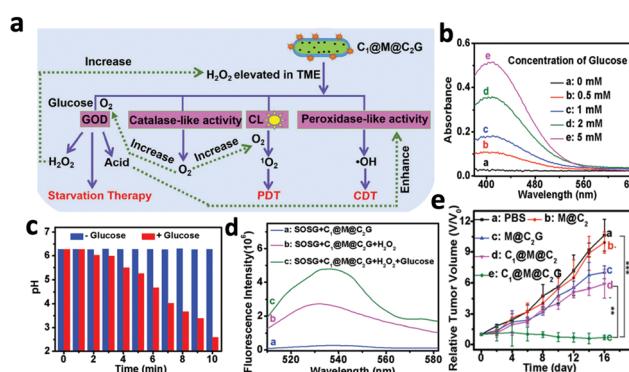

Fig. 6 (a) Schematic illustrations of the enhanced PDT by C$_1$@M@C$_2$G through enhanced generation of H$_2$O$_2$ combined with other therapies. (b) Absorption spectra of C$_1$@M@C$_2$G particles and glucose, where higher absorbance refers to higher H$_2$O$_2$ content. (c) pH measurement of the C$_1$@M@C$_2$G particle following addition of glucose (1 mg mL^{-1}) over time. (d) Fluorescence spectra of SOSG (^{1}O$_2$ indicator) added to C$_1$@M@C$_2$G after mixing with H$_2$O$_2$ and glucose, where higher fluorescence indicates higher ^{1}O$_2$ production. (e) In vivo tumour growth curves of mouse groups with different treatments. Reproduced with permission from ref. 54. Copyright 2021, Royal Society of Chemistry.

This journal is © The Royal Society of Chemistry 2024

Chem. Soc. Rev., 2024, **53**, 2898–2931 | **2903**

while the control groups without CaO_2 maintained a cell viability close to 90%.

2.4.2 Photothermal therapy. Photothermal therapy (PTT) involves the use of an NIR laser to activate nanoparticles delivered to the tumour area, which results in a temperature increase in the tumour and possibly tumour ablation.[56] Chemiluminescent nanoparticles are usually applied to enhance the photothermal effect or provide imaging guidance for the therapy.

Gold nanoparticles (AuNPs) have been applied for photothermal therapy due to their ability to generate heat upon NIR activation. However, these small AuNPs are easily excreted from the body, resulting in low tumour accumulation and poor therapeutic efficacy. A recent study by Shi *et al.* demonstrated the possibility of photo-cross-linking small Au NPs by CL to prevent rapid clearance from the tumour area.[57] Small AuNPs (25 nm) were covalently conjugated with photolabile molecules and luminol (t&mAuNP/Lu). Under the reaction between luminol and H_2O_2, the luminescent nanoparticles emitted chemiluminescence and induced cross-linking of the AuNPs, forming covalently cross-linked AuNP aggregates (Fig. 7a). Tumours treated with t&mAuNP/Lu nanoparticles showed a local temperature increase to 55.4 °C following 10 minutes of 808 nm laser irradiation, while other treatment groups without luminol remained below 45 °C (Fig. 7b). *In vivo* studies with mice bearing $4T_1$ tumours showed significant growth inhibition following PTT with t&mAuNP/Lu (Fig. 7c). Apart from improving therapeutic efficacy, chemiluminescent nanoparticles could also provide image guidance to PTT. Li *et al.* developed a nanoplatform (ALPBs) that incorporates luminol and PCPDTBT, which is a photothermal agent with NIR

emission.[58] The CL generated from the luminol–H_2O_2 reaction activated PCPDTBT to produce NIR luminescence, which exhibited a strong intensity of several magnitudes higher than the CL *in vivo*. In addition, CL diminished after 5 hours while the NIR luminescence still exhibited high intensity after 7 hours. This enabled the monitoring of photothermal therapy in deep tissues using CL.

2.4.3 Drug delivery. Chemiluminescent nanomaterials could offer therapeutic choices by triggering drug delivery at specific locations or providing imaging-monitored drug delivery. For example, a target-catalysed DNA nanohydrogel loaded with a drug relied on chemiluminescence for imaging/monitoring of the drug release location.[38] The DNA nanohydrogels have a high drug loading capacity, with each unit providing approximately 30 specific loading sites for Dox. Once the target microRNA binds to the DNA structure, the structure collapses and generates DNAzyme that catalyses the CL between luminol and H_2O_2. This results in targeted drug release and enhanced CL for the monitoring of drug release. *In vitro* confocal fluorescence showed that sgc8-DNA nanohydrogels loaded with Dox only caused chemiluminescence in the target cells CCEF-CEM, but not in the control cells Ramos.

Chemiluminescent nanomaterials could also trigger the release of light-sensitive drug for the treatment of inflammatory diseases. Wang *et al.* devised a ROS-responsive drug delivery system using covalently self-assembled polymer nanocapsules (Azo-NCs), which were formed through the cross-linking of macrocyclic cucurbit[6]urils with a photosensitive azobenzene derivative (Azo).[59] Luminol was co-loaded into the Azo-NCs along with a therapeutic payload. Under inflammatory conditions, the upregulated H_2O_2 reacted with luminol to produce enhanced CL which induced photoisomerization of the Azo groups within the Azo-NCs, releasing the encapsulated payload. *In vivo* studies with a zebrafish model demonstrated a 5.5-fold higher CL intensity accompanied by enhanced drug release in the inflammatory regions compared to the healthy regions.

2.5 Strengths and weaknesses of chemiluminescence-mediated light therapy

Chemiluminescence-mediated light therapy has emerged as an intriguing therapeutic approach that offers deep tissue light-based therapies without the need for external light irradiation. Unlike traditional light-based therapies, light penetration depth is no longer a concern as it harnesses intrinsic chemiluminescent properties to generate light. Moreover, chemiluminescence-mediated light therapy could passively target inflammation-related diseases, including cancer, cardiovascular diseases, and autoimmune conditions. In most inflammatory conditions, reactive oxygen species like H_2O_2 are upregulated, which can react more rapidly with the chemiluminophores to generate stronger CL.

However, there are several limitations to chemiluminescence that should be considered. For example, chemiluminescence-mediated light therapy lacks external control over CL generation. Unlike other light-based therapies excited with external sources, controlling the intensity and duration of chemiluminescent
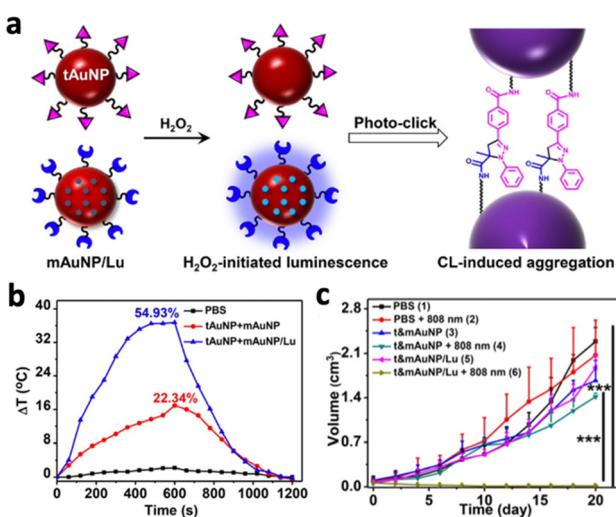
Fig. 7 (a) Schematic illustration showing the chemiluminescence reaction between luminol on Au NPs that led to photoclicking of Au NPs. (b) Temperature changes following 808 nm irradiation on PBS, t&mAuNP and t&mAuNP/Lu. (c) Change in tumour volume of mice following 21 days of photothermal treatments with different systems. Reproduced with permission from ref. 57. Copyright 2021, Wiley-VCH Verlag GmbH & Co. KGaA, Weinheim.

2904 | *Chem. Soc. Rev.*, 2024, **53**, 2898–2931

This journal is © The Royal Society of Chemistry 2024

reactions is difficult. Furthermore, the therapeutic efficacy is highly dependent on the availability of intracellular ROS, which could be insufficient to generate a strong CL. Hence, the produced CL is usually too weak to serve as an effective therapy alone or to be detected *in vivo*. Although certain approaches have been developed to generate ROS endogenously, it highly depends on the reaction rate and kinetics. Moreover, the lack of NIR-emitting chemiluminophores also limits the imaging and tracking of deep tissue therapy.

3. NIR-excited luminescence

Using an external excitation source gives better control over the intensity and duration of the light generated *in vivo*. As mentioned before, both UV and visible light possess low tissue penetration and would not be suitable for deep tissue therapy. However, biological tissues possess an "optical transparency window" for light with wavelength ranging from 800–1000 nm, where they experience less light scattering and attenuation.[60] Hence, studies have been conducted to engineer nanosystems that could be activated by NIR-I light (700–1000 nm), especially at 808 nm or 980 nm.[61,62] Typically, NIR light excites nanomaterials to emit luminescence through 4 major mechanisms: two-photon excitation (TPE), energy transfer upconversion (ETU), downconversion (DC) and persistent luminescence (PersL) (Fig. 8).

Upconversion nanomaterials exhibit anti-Stokes behaviour and are activated by NIR light to emits light at a shorter wavelength.[63] They emit in the UV/visible wavelength range to activate various light-sensitive molecules, such as photosensitizers, for light-mediated therapy. More recently, it was realised that NIR-II light (1000–1700 nm) possesses even less scattering in biological tissues and demonstrates deep tissue imaging ability at higher resolution than NIR-I light.[9] Hence, downconversion nanomaterials were also engineered to be excited by NIR-I light to emit in the NIR-II region for deep tissue imaging and monitoring of therapeutic process.[64,65] Due to the low tissue attenuation of NIR-II light, they were also used to excite certain upconversion nanosystems to increase the tissue depth for therapy.[7]

In this section, we will discuss the utilisation of NIR light located in the range of 700–1700 nm on activating upconversion or downconversion nanosystems and their application in deep tissue light-mediated therapy. Moreover, we will also summarise the strategies to enhance the luminescence produced by various nanosystems.

3.1 Upconversion luminescence

Upconversion luminescence typically refers to the anti-stoke shifts in emission, where the emission wavelength is always shorter than the excitation wavelength.[63] Many mechanisms of upconversion luminescence exist, including two-photon excitation (TPE), frequency upconversion (FU) and energy transfer upconversion (ETU) (Fig. 8a–c).[66–68] In the following section, we will review nanomaterials that exhibit upconversion luminescence and their corresponding mechanisms.

3.1.1 Metal-based nanomaterials. Metal-based nanomaterials are known to possess upconversion properties with two-photon excitation, where 2 photons of the same energy excite the atom simultaneously to a higher energy level and emit photons of a shorter wavelength (Fig. 8a).[66] For example, Ag–TiO$_2$ composites could be excited by two 800 nm NIR photons to emit upconversion luminescence at 552 nm.[66] This is due to the band-to-band radiative transition in Ag$_2$O with a band gap of 2.25 eV. In addition, gold nanoshells could also be excited at 780 nm by 2-photon excitation and emit upconversion luminescence at 610 nm.[69]

3.1.2 Organic nanomaterials. Certain inorganic nanomaterials also exhibit upconversion properties through two-photon excitation. Examples include carbon nanotubes emitting upconversion luminescence at 980 nm following 1100 nm excitation, and helicine-based nanographene emitting light at 680 nm following 900 nm excitation.[70,71] With Eu^{3+} doping, the organic complex [Eu(THA)$_3$(phen)] (HTHA = 4,4,4-trifluoro-1-(9-hexylcarbazole-3-yl)-1,3-butanedione, phen = 1,10-phenanthroline) also exhibited upconversion luminescence at 612 nm following 808 nm excitation.[72]

However, the efficiency of two-photon excitation is low due to the low probability of 2 photons exciting the nanomaterial simultaneously. Hence, Peng *et al.* developed an organic upconversion nanomaterial that depends on single-photon excitation.[68] The organic nanomaterial (FUCP-1) contains a rhodamine derivative (FUCP-1) and produces upconversion luminescence through frequency upconversion (Fig. 9a). FUCP-1 was first excited from the ground electronic state (S$_0$) to thermally vibrational–rotational states (S$_t$) with the heat derived from the Boltzmann
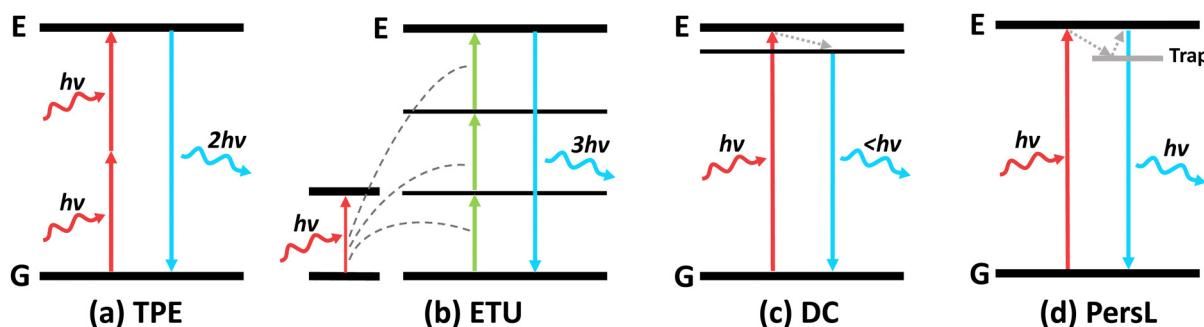
Fig. 8 Schematic illustrations of the energy transfer mechanisms of (a) two-photon excitation (TPE), (b) energy transfer upconversion (ETU), (c) downconversion luminescence (DC) and (d) persistent luminescence (PersL) in NIR-excitable nanomaterials.

This journal is © The Royal Society of Chemistry 2024

Chem. Soc. Rev., 2024, **53**, 2898–2931 | 2905
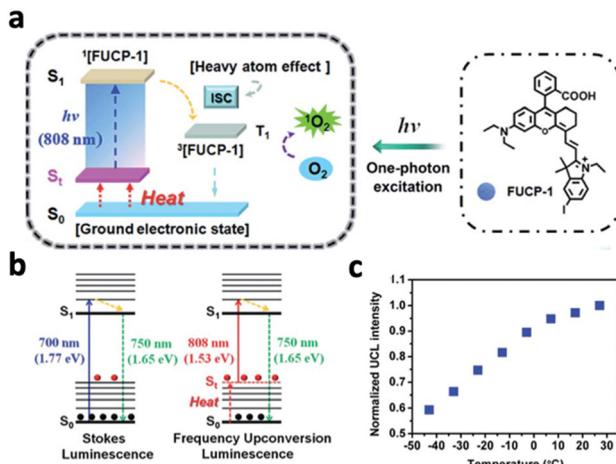
Fig. 9 (a) Schematic diagram of upconversion luminescence and PDT mechanism of FUCP-1. (b) Schematic energy level demonstration of the mechanisms of traditional Stokes luminescence and frequency upconversion luminescence (FUCL). (c) Upconversion luminescence intensity changes of FUCP-1 at different temperatures. Higher temperature results in stronger UCL due to more S_t states. Reproduced with permission from ref. 68. Copyright 2019, Royal Society of Chemistry.

distribution of molecules (Fig. 9b). Therefore, a higher temperature enhances upconversion luminescence intensity (Fig. 9c). Following 808 nm excitation, FUCP-1 is excited from S_t to S_1 and returns to the ground state, producing emission at 750 nm. FUCP-1 was shown to effectively sensitize O_2 to $^1O_2$ and presented superior inhibition of $4T_1$ cells. Although this nanosystem exhibited higher efficiency than most two-photon-excited nanomaterials, the emission wavelength was located near the excitation wavelength. This is due to the small energy level difference between S_t and S_0, which limits its upconversion ability for application in deep tissue therapy.

3.1.3 Lanthanide-based nanomaterials. Lanthanide-doped upconversion nanoparticles (UCNPs) make use of the energy transfer upconversion (ETU) mechanism, which is more efficient and enables stronger upconversion ability. The trivalent lanthanide ions incorporated in the host crystal have long lifetime and distinct energy levels, enabling the sequential absorption of multiple excitation photons (Fig. 8b).[73] In addition, they possess strong upconversion abilities and can generate upconversion emission in the visible or even UV wavelength range.[74,75] Lanthanide-based nanomaterials predominantly occur as fluorides, oxides, or oxofluorides. Among these materials, $NaLnF_4$ (Ln = Y, Gd, Yb, Lu, and Er) was the most studied upconversion nanosystem.

Upconversion $NaYF_4$:20% Yb^{3+},2% Tm^{3+} nanocrystals were first reported by Chow et al. in 2006.[76] Yb^{3+} acted as the sensitiser, absorbing NIR photons at 980 nm and transferring the energy to the activator Tm^{3+}. Following 980 nm NIR excitation, $NaYF_4$:20% Yb^{3+},2% Tm^{3+} exhibited blue fluorescence at 450.5 ($^1G_4$–$^3H_6$), 475 nm ($^1G_4$–$^3H_6$) and 800 nm. By changing the lanthanide dopants in the crystal, excitation and emission wavelengths can be altered. For example, substituting Tm^{3+} in $NaYF_4$:Yb^{3+},Tm^{3+} with Nd^{3+} resulted in emission at 803 nm

following 980 nm laser irradiation, due to the $^2H_{9/2}$,$^4F_{5/2}$–$^4I_{9/2}$ transition of Nd^{3+}.[77] Exciting $NaYF_4$:Yb^{3+},Tb^{3+} at 980 nm resulted in green upconversion emission at 480 nm, corresponding to Tb^{3+} transition at $^5D_4$–$^7F_6$.[75] In addition, doping Er^{3+} into $NaYF_4$:Yb^{3+} resulted in visible emissions at 550 nm, 660 nm and 800 nm and 1000 nm, corresponding to $^4S_{3/2}$–$^4I_{15/2}$, $^4F_{9/2}$–$^4I_{15/2}$, $^4I_{9/2}$–$^4I_{15/2}$ and $^4I_{11/2}$–$^4I_{15/2}$ transitions of Er^{3+}, respectively.[76] Apart from acting as an activator, Er^{3+} could also act as a sensitizer by absorbing NIR-II light at 1500 nm due to its transition from $^4I_{15/2}$ to $^4I_{13/2}$.[78] Therefore, exciting $NaYF_4$:Er^{3+} at 1500 nm results in the same emissions at 550 nm, 660 nm and 800 nm and 1000 nm. The ability of Er^{3+} to be excited by NIR-II light is beneficial since NIR-II light exhibits higher tissue penetration depth than NIR-I light, allowing the nanosystems to be activated in deep tissue. However, despite its ability to be excited at 1500 nm, Er^{3+} is not efficient in transferring its energy to other activators due to its highly efficient upconversion (Fig. 10a). Therefore, Tian et al. constructed a multi-layered nanocrystal that was composed of a Yb^{3+}-rich core doped with activators ($NaYbF_4$:Ln, Ln = Ho and Tm), with the Er^{3+}-doped $NaYF_4$ coated on top.[79] Upon excitation at 1550 nm, the localized enrichment of Yb^{3+} enables efficient energy transfer from Er^{3+} to Yb^{3+} ions via inter-ion energy transfer, effectively suppressing the multi-photon upconversion of Er^{3+} (Fig. 10b). Enhanced emissions at 1200 nm for Ho^{3+} and 1470 nm for Tm^{3+} were observed (Fig. 10c and d). Given that Ho^{3+} and Tm^{3+} also have emission peaks in the visible spectrum, this nanosystem was able to emit both visible and NIR-II photons following NIR-II activation, which would be beneficial for the simultaneous activation of phototherapeutic systems and imaging modes.
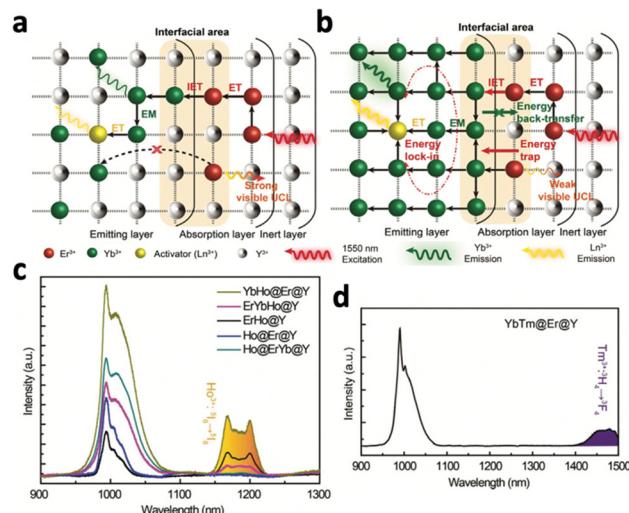
Fig. 10 Schematic illustration of energy transfer in the Er^{3+}-sensitized nanomaterial under 1550 nm excitation. (a) Common strategy of low Yb^{3+} doping and relying on Er^{3+} to relay energy, which results in low ET efficiency. (b) Proposed design strategy using the locally enriched Yb^{3+} embedded in the emitting layer relays the excitation energy from the Er^{3+}-sensitized absorption layer to Ln^{3+}. NIR upconversion emission spectra of (c) Yb,Ho@Er@Y, Er,Ho@Y, Er,Yb,Ho@Y, Ho@Er@Y, Ho@Er,Yb@Y and (d) YbTm@Er@Y. Reproduced with permission from ref. 79. Copyright 2022, Royal Society of Chemistry.

2906 | Chem. Soc. Rev., 2024, **53**, 2898–2931

This journal is © The Royal Society of Chemistry 2024

It was reported that the hexagonal phase of $NaYF_4$ favours upconversion luminescence due to a significant electron cloud distortion of the cations.[76] Aiming to stabilize the hexagonal phase of $NaLnF_4$ nanocrystals, Gd^{3+} was doped into different systems like $NaYF_4$:Yb^{3+},Er^{3+} and $NaYbF_4$:Tm^{3+}.[61,80] Higher Gd^{3+} doping resulted in a higher population of the hexagonal phase, corresponding to a 40-fold stronger upconversion intensity for $NaYbF_4$:Tm^{3+}. This raised interest in the complete substitution of Y^{3+} ions in $NaYF_4$ with Gd^{3+} ions to improve upconversion luminescence, producing $NaGdF_4$:Yb^{3+},Er^{3+} and $NaGdF_4$:Yb^{3+}, Tm^{3+}.[74,81] In addition, high upconversion efficiency was observed in $NaGdF_4$-based nanosystems, since the lowest excited level ($^6P_{7/2}$) of Gd^{3+} is in the ultraviolet region. This energy level is significantly higher than the excited levels of most sensitizers and activators like Yb^{3+} and Er^{3+}.[81] Therefore, energy loss through energy transfer from Yb^{3+} and Er^{3+} to the 4f levels of Gd^{3+} is avoided.

Apart from $NaLnF_4$, certain other lanthanide-based hosts possessing low phonon energy could also be doped with a sensitizer and activator to exhibit upconversion luminescence. Examples include KYb_3F_{10}:Yb^{3+},Tm^{3+}, Y_2O_3:Yb^{3+},Tm^{3+}, Y_2O_3:Yb^{3+}, Er^{3+} or Gd_2O_3:Yb^{3+},Er^{3+} and $GdOF$:Yb^{3+},Er^{3+}, which possess high stability in the hexagonal phase.[82–86] Certain non-lanthanide-based hosts could also emit upconversion luminescence following lanthanide doping, including $ZnGa_2O_4$:Yb^{3+},Tm^{3+},Eu^{3+}-doped [$Eu(THA)_3(phen)$] (HTHA = 4,4,4-trifluoro-1-(9-hexylcarbazole-3-yl)-1,3-butanedione, phen = 1,10-phenanthroline) and SrF_2:Ho^{3+}.[87,88] Similar to Er^{3+}, Ho^{3+} could also act as both the sensitizer and activator. Under 1156 nm excitation, Ho^{3+} exhibited upconversion luminescence at 554 nm, 653 nm, 755 nm, and 900 nm due to the $^5S_2$,$^5F_4$–$^5I_8$, $^5F_5$–$^5I_8$, $^5S_2$,$^5F_4$–$^5I_7$ and $^5I_5$–$^5I_8$ transitions.[87]

By bridging Yb^{3+}, Er^{3+} and Y^{3+} with the organic linker pyrazine, an upconverting organic–inorganic hybrid was constructed.[89] Possessing high surface area and porosity, the upconversion luminescence produced by organic–inorganic hybrids interact more strongly and in closer proximity with biomolecules for therapeutic applications. The nanohybrid absorbed NIR photons of 974 nm with the sensitiser Yb^{3+}, which transferred the energy to the activator Er^{3+}, resulting in efficient emission of red and green upconversion luminescence. The hybrid also enabled the creation of Yb^{3+}–Er^{3+} pairs, facilitating efficient energy transfer while shielding the energy transfer and relaxation processes from the vibrations of the ligands.

3.2 Downconversion luminescence

Downconversion luminescence refers to conventional fluorescence, where the emission wavelength is longer than the excitation wavelength due to Stoke's shift. Downconversion luminescence can be useful in monitoring deep-tissue therapy as it can potentially produce emissions in the NIR-II region that possess deep biological penetration. In this section, we will discuss the nanomaterials that exhibit downconversion luminescence, especially in the NIR-II region, following NIR activation.

3.2.1 Organic-based nanomaterials.
Certain organic-based nanomaterials could absorb NIR photons and emit photons at a longer wavelength. For example, carbon dots were reported to emit light at 925 nm following 808 nm excitation.[90] In addition, the carbon nanodots also exhibited high photothermal conversion efficiency (30.6%), which led to almost a complete disappearance of mice tumour in vivo. Certain organic dyes or photosensitisers could also be excited by NIR. For example, cyanine-based nanomicelles exhibited emission at 812 nm following 730 nm irradiation.[91] More recently, Jiang's group reported that the photosensitiser BODIPY could be activated by 808 nm NIR light to emit NIR-II photons.[64] The PEG-functionalised BODIPY was utilized for molecular imaging of MC38 tumours in vivo with a high tumour to normal tissue signal ratio. In addition, NIR irradiation of PEG-functionalised BODIPY induced the formation of $^1O_2$ to kill MC38 cancer cells, and the MC38 tumours were fully removed after 30 days of photodynamic therapy.

However, certain limitations still exist for organic-based nanomaterials that hinder their application in deep tissue light-mediated therapy – such as the broad emission peaks, short luminescence lifetime, susceptibility to photobleaching and the lack of control and tunability over excitation and emission wavelength.

3.2.2 Lanthanide-based nanomaterials.
Lanthanide-based nanomaterials are more favourable for NIR-excited downconversion luminescence due to their narrow and unique emission peaks, along with their high versatility and tunability in altering optical properties.

Although $NaLnF_4$ is well-known for its upconversion properties, it can also exhibit downconversion luminescence with similar lanthanide dopants. Not only could Er^{3+} and Ho^{3+} be activated by NIR-II luminescence at 1550 nm and 1150 nm respectively (mentioned in the upconversion section), they could also emit NIR-II downconversion luminescence at the same wavelengths.[92] By doping different activators like Ho^{3+} (20%), Pr^{3+} (3%), Tm^{3+} (4%) and Er^{3+} (10%) into $NaYbF_4$, the nanosystem produced emissions in the NIR-II region–1155 nm (Ho^{3+}), 1310 nm (Pr^{3+}), 1475 nm (Tm^{3+}), and 1525 nm (Er^{3+}) following 980 nm excitation.[93] The emission peaks were assigned to the transitions $^5I_6$–$^5I_8$, $^1G_4$–$^3H_5$, $^3H_4$–$^3F_4$, and $^4I_{13/2}$–$^4I_{15/2}$ for Ho^{3+}, Pr^{3+}, Tm^{3+}, and Er^{3+}, respectively.

It has been reported that NIR light at around 808 nm exhibits less attenuation in biological tissues compared to the traditional 980 nm excitation wavelength of Yb^{3+} ions.[94] Therefore, Li et al. co-doped Nd^{3+} with Yb^{3+} to form CaF_2:Yb^{3+},Nd^{3+}, where Nd^{3+} was excited by 808 nm photons to the $^4F_{5/2}$ energy level.[95] Nd^{3+} then transferred the energy to the $^2F_{5/2}$ level of Yb^{3+}, leading to the emission of 980 nm photons through $^2F_{5/2}$–$^2F_{7/2}$ transition. Apart from relaying energy to Yb^{3+}, Nd^{3+} itself could emit downconversion luminescence in the NIR-I/II regions. Following 808 nm excitation, Nd^{3+} emitted at 903 nm, 1062 nm, and 1336 nm corresponding to the $^4F_{3/2}$–$^4I_{9/2}$, $^4F_{3/2}$–$^4I_{11/2}$, and $^4F_{3/2}$–$^4I_{13/2}$ transitions.[96] Similarly, Tm^{3+} in $LiTmF_4$ could be excited by either 800 nm or 1208 nm radiation, leading to the emission of NIR-IIc photons (1600–2100 nm) due to the $^3F_4$–$^3H_6$ transition of Tm^{3+}, allowing even deeper tissue penetration and a higher SBR in in vivo imaging.[8] Apart from Nd^{3+} and Tm^{3+}, Ni^{2+} could also be excited by 808 nm. Under 808 nm excitation, $ZnGa_2O_4$:Ni^{2+},Er^{3+} experienced

This journal is © The Royal Society of Chemistry 2024

Chem. Soc. Rev., 2024, 53, 2898–2931 | 2907

the population of the $^3T_2(^3F)$ level in Ni^{2+}.[97] A portion of the energy relaxes radiatively from $^3T_2(^3F)$ to $^3A_2(^3F)$, emitting 1280 nm luminescence, while another portion of the energy is transferred to the $^4I_{13/2}$ level of Er^{3+}, which then relaxes and emits light at 1550 nm due to the $^4I_{13/2}$–$^4I_{15/2}$ radiative transition.

3.2.3 Metal-based nanomaterials. Certain metals could be excited by NIR to emit downconversion luminescence. For example, gold nanoclusters could be excited by NIR photons at 808 nm or 700 nm to emit light at 1050 nm, due to the radiative decay of the core states of Au.[98,99] Apart from gold nanoclusters, platinum-based metal–organic frameworks (Pt(II)–porphyrin) could also emit NIR luminescence at 1000 nm under 800 nm excitation.[100] Metal-based quantum dots Ag_2S can be activated by an 808 nm laser, resulting in NIR-II emission at 1200 nm.[101] In addition, narrow band-gap semiconductors like I–III–VI QDs, which consist of two metals and a chalcogen, also exhibit high quantum yield in the NIR-II region.[102] For example, $AgInTe_2$ could produce NIR-II emission at 1090 nm following 808 nm excitation, which has a NIR-II quantum yield of 25.2%.[103] However, similar to organic nanomaterials, metal-based nanomaterials produce broad emission peaks and lacks tunability in their design.

3.3 Persistent luminescent nanoparticles

Persistent luminescence nanoparticles (PLNPs) are luminescent nanoparticles that retain the excitation energy within the material through trapping mechanisms, allowing them to slowly emit photons over extended durations even after the excitation source has been removed.[104] Following excitation, electrons are tunnelled to traps and are slowly released to emit luminescence (Fig. 8d). This unique phenomenon does not require a continuous excitation source for light emission, resulting in enhanced signal-to-noise imaging and deep tissue therapy without the need for continuous excitation sources, eliminating side effects like light scattering and tissue damage.

However, most PLNPs could only be activated by high-energy excitation sources like UV/X-rays to pump the excitons into the deep traps (Fig. 11a).[14,105,106] Although certain PLNPs could be re-activated by NIR light after UV excitation, the intensity and afterglow time were significantly reduced.[105,107] To engineer PLNPs that can be directly activated by NIR light, Han's group developed $CaSnO_3$:Bi^{2+}, which exhibited persistent

luminescence at 810 nm following 700 nm NIR excitation.[108] This nanophosphor operates through an "upconversion-like" carriers' transition process, as the NIR light first excites the deep trap due to its low energy, and slowly transitions to the shallow traps that have higher energy (Fig. 11b). The emission band at 810 nm was assigned to the $^2P_{3/2}(1)$–$^2P_{1/2}$ transition of Bi^{2+} (Fig. 11b). Compared with the traditional PLNP $ZnGa_2O_4$:Cr^{3+} excited with NIR light, $CaSnO_3$:Bi^{2+} exhibited 10-fold stronger persistent luminescence (Fig. 11c).

Efforts have also been made to synthesize upconverting persistent luminescent nanomaterials. One method is to physically combine upconversion nanomaterials with persistent luminescence nanomaterials, such that the emission spectra of the UCNP overlaps with the excitation spectra of PLNP to generate persistent luminescence.[109,110] In 2017, Li's group produced a nanohybrid consisting of upconversion nanoparticles ($NaYbF_4$:Tm@$NaYF_4$) and persistent nanoparticles ($Zn_{1.1}Ga_{1.8}Ge_{0.1}O_4$:0.5% Cr).[109] Upon 980 nm laser irradiation, the $NaYbF_4$:Tm@$NaYF_4$ UCNP emitted visible light at 345, 360, 452 and 475 nm, activating the $Zn_{1.1}Ga_{1.8}Ge_{0.1}O_4$:0.5% Cr PLNP to give persistent luminescence at 700 nm. Although this nanohybrid allowed deep NIR tissue bioimaging with long afterglow time, the energy transfer efficiency of the system is questionable. Shortly after, Liu *et al.* directly doped lanthanide ions into a PLNP host crystal, producing $Zn_3Ga_2GeO_8$:Yb^{3+},Er^{3+},Cr^{3+} that exhibited upconverted persistent luminescence.[111] Under 980 nm excitation, Yb^{3+} underwent excitation to the $^2F_{5/2}$ level and transferred the energy to the adjacent Er^{3+}, resulting in the population of its excitation state levels at $^2H_{11/2}$, $^4S_{3/2}$ and $^4F_{9/2}$. Er^{3+} then relayed the energy to the traps located in the crystal lattice. After the cessation of excitation light, the energy was transferred to Cr^{3+}, emitting light at 700 nm *via* ^2E–$^4A_2$ transition. This nanocrystal exhibited long afterglow time, with detectable luminescence 10 hours after intravenous injection in mice.

The afterglow time of inorganic persistent luminescent nanoparticles mainly depends on the trap density of the nanomaterial. On the other hand, organic-based nanomaterials usually rely on sustained biochemical reactions for prolonged afterglow emissions. For example, many organic-based PLNPs produce dioxetane as an intermediate, which degrades continuously to emit visible photons.[53] Hence, many organic afterglow luminescent nanosystems incorporate phenylenevinylene (PPV), which produces singlet oxygen under NIR excitation. This oxidizes the double bonds in the structure of PPV, producing unstable dioxetane intermediates that contribute to afterglow luminescence.[112] Efforts have been made to achieve *in vivo* delivery of PPV through encapsulation with polymers for deep tissue tumour imaging.[113,114] Pu *et al.* synthesized NIR-emitting $F1^{2+}$-ANP, which consists of PPV, $EMF1^{2+}$, and the photosensitiser NIR775 encapsulated in PEG (Fig. 12a).[115] Initially, $F1^{2+}$-ANP exhibited suppressed afterglow due to the quenching effect of $F1^{2+}$ species. However, upon interaction with the enriched H_2S in the tumour area, $F1^{2+}$-ANP is reduced to F2-ANP, resulting in the recovery of $^1O_2$ production and fluorescence at 580 nm from the produced dioxetane. This resulted in the excitation of NIR775 and afterglow luminescence at 780 nm (Fig. 12b). $F1^{2+}$-ANP added with
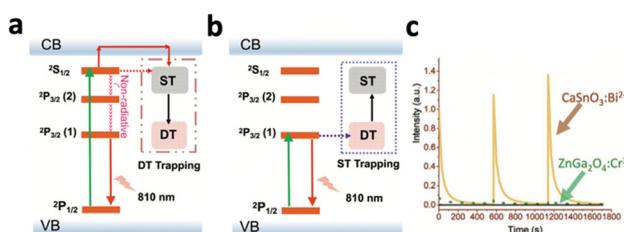
Fig. 11 Schematic illustration of the energy transfer mechanism during (a) high-energy (UV) photon-excited afterglow and (b) low-energy (NIR) photon-excited afterglow. (c) Afterglow decay curves of $CaSnO_3$:Bi^{2+} and $ZnGa_2O_4$:Cr^{3+}. Reproduced with permission from ref. 108. Copyright 2021, Wiley-VCH Verlag GmbH & Co. KGaA, Weinheim.

2908 | *Chem. Soc. Rev.*, 2024, **53**, 2898–2931

This journal is © The Royal Society of Chemistry 2024
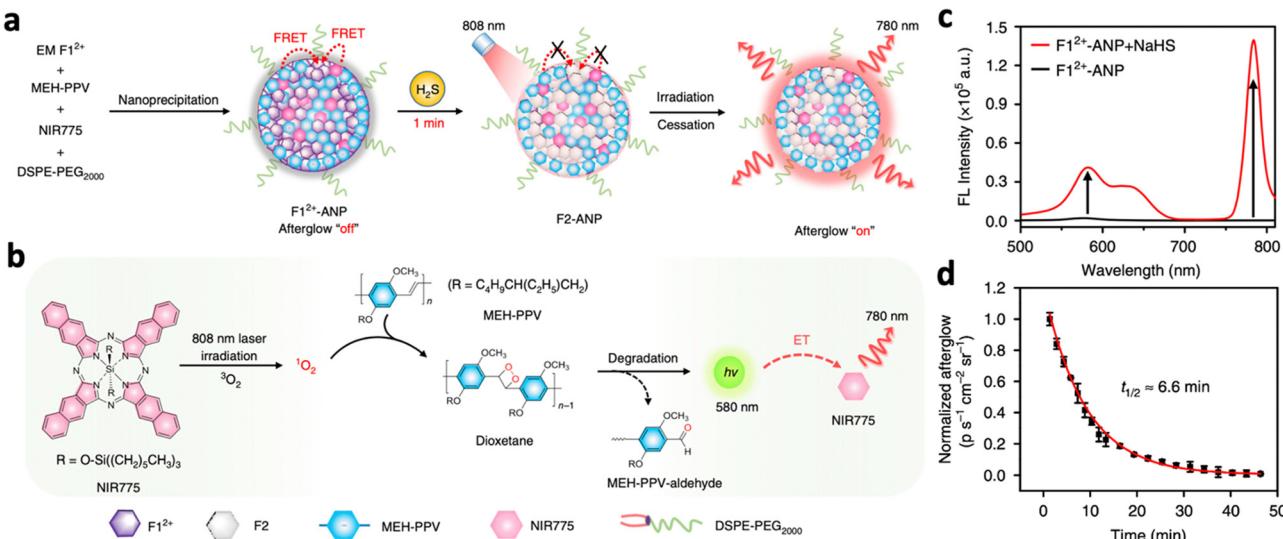
Fig. 12 (a) Schematic illustration of the proposed mechanism of H_2S-activated NIR afterglow luminescence at 780 nm following irradiation with an 808 nm laser. (b) Schematic illustration of the photoreaction processes to produce NIR afterglow luminescence within activated F1^{2+}-ANP (*i.e.*, F2-ANP). (c) Fluorescence spectra of F1^{2+}-ANP in the presence or absence of NaHS (excitation: 808 nm). (d) Afterglow decay of F1^{2+}-ANP in the presence of H_2S monitored at 780 nm. Reproduced with permission from ref. 115. Copyright 2020, Nature Publishing Group.

NaHS exhibited fluorescence at 580 nm and 780 nm while F1^{2+}-ANP alone did not exhibit any fluorescence (Fig. 12c). The nanoprobe also showed high afterglow intensity in the presence of H_2S with a long half-life of 6.6 minutes (Fig. 12d), while showing an SBR of 71.9 *in vivo* 12 hours post-injection.

3.4 Enhancing NIR-excited luminescence

3.4.1 Engineering passive shell coatings. It is known that luminescent nanoparticles are vulnerable to surface quenching due to their large surface area, which reduce the luminescence intensity of the nanoparticles. One traditional method to reduce surface quenching is to engineer homogenous passive shell coatings on the surface of the nanoparticles. The passive coating, lacking both the sensitizer and activator, serves as an inert layer, preventing quenching on the surface. Homogenous passive shell coatings share the same crystal structure with the core, which allows a more favourable growth and has been extensively demonstrated in upconversion nanoparticles. In 2007, Yi *et al.* demonstrated a significant improvement of 7.4 times and 29.6 times in the visible UC emissions of hexagonal-phase NaYF$_4$:Yb^{3+}/Er^{3+} and NaYF$_4$:Yb^{3+}/Tm^{3+}, respectively, by incorporating a thin layer of NaYF$_4$ ($\sim$2 nm) as the outer shell.[116] More recently, it has been reported that 15 nm NaGdF$_4$:Er^{3+} ions exhibited 167.7-fold upconversion luminescence enhancement following inert shell coating.[78] The same principle applies to the downconversion nanoparticle Ba$_2$LuF$_7$:Er^{3+}/Yb^{3+}/Nd^{3+}, which exhibited 3.5-fold luminescence enhancement following coating of inert Ba$_2$LuF$_7$. However, luminescence intensity might be compromised if the shell coating becomes too thick due to the significant reduction in energy migration; hence the optimal shell thickness would be 1 to 3.8 nm on NaYF$_4$.[117]

Apart from reducing surface quenching and improving luminescence intensity, heterogenous passive shell coatings could provide additional benefits, such as introducing imaging modalities or improved biocompatibility. For example, coating Gd^{3+}-containing shells, *i.e.*, NaGdF$_4$, could enable T_1-weighted MRI for image guided therapy.[118,119] In addition, coating the magnetic Fe$_x$O$_y$ shell on NaYF$_4$:Yb^{3+},Tm^{3+} enabled T_2-enhanced magnetic resonance imaging (MRI) of the lymphatic node.[120] In addition, the emission intensity at 475 nm was increased by 2.5-fold simultaneously due to the reduction in surface quenching. Fe$_3$O$_4$ was also coated on UCNPs to enable magnet-guided photodynamic therapy towards the tumour site.[6] Apart from coating iron oxides, passive silica coating was also studied extensively since it provides a hydrophilic surface on the UCNPs/DCNPs, which is more suitable for biological applications.[121] In addition, silica coating exhibits low cytotoxicity and provides a chemically active surface that can be easily modified to introduce diverse functional groups, catering to the conjugation of biological molecules or functional nanoparticles. In 2008, Zhao *et al.* reported SiO$_2$-coated Y$_2$O$_3$:Eu^{3+} nanoparticles, which exhibited 4.13 times luminescence enhancement compared to the uncoated nanoparticles.[122] More recently, SiO$_2$ coating on ZnGa$_2$O$_4$:Yb^{3+}, Tm^{3+} successfully enhanced upconversion luminescence intensity by 12 times at 700 nm and 830 nm following 980 nm excitation.[88]

3.4.2 Engineering active shell coatings. Different from passive shell coatings, active shell coatings usually contain sensitiser ions to maximise light absorption. For example, NaGdF$_4$:Yb^{3+},Tm^{3+} coated with NaGdF$_4$:Yb^{3+} exhibited a 3-fold increase in green upconversion luminescence due to the reduction in surface quenching and the increased surface area of Yb^{3+} to absorb NIR photons.[123] Since 808 nm photons possess deeper tissue penetration depth than 980 nm photons, various studies incorporated Nd^{3+} ions or both Nd^{3+} and Yb^{3+} ions in the active shell, which allows the nanosystem to be excited directly by 808 nm light.[124–126]

Having more than 1 sensitizer located in different layers of active shell coatings allows the nanosystem to be excited by

multiple wavelengths, *i.e.*, orthogonal excitation. Our group previously reported NaErF$_4$:Yb/Tm@NaYF$_4$:Yb@NaNdF$_4$:Yb, which could be excited by 808 nm and 980 nm due to the presence of both Yb^{3+} and Nd^{3+}.[127] Under 980 nm excitation, the Yb^{3+} sensitizers present in the core (NaErF$_4$:Yb/Tm) and two subshells (NaYF$_4$:Yb and NaNdF$_4$:Yb) absorbed the excitation light and transferred it to the Er^{3+} activators in the core (Fig. 13a). The elevated concentration of Er^{3+} in the excited state increased the likelihood of cross-relaxation between the $^4I_{11/2}$ state and $^4F_{7/2}$ state, promoting the population of the $^4F_{9/2}$ state and enhanced the 650 nm red upconversion emission (Fig. 13b). When excited with 808 nm light, the Nd^{3+} ions served as sensitizers and transferred the excitation energy to Yb^{3+} ions and subsequently to the Er^{3+} activators in the core (Fig. 13c). However, since the Nd^{3+} ions are only localized in the outer shell, the absorption of 808 nm light is significantly lower compared to 980 nm light. Moreover, the longer energy migration distance between Nd^{3+} and Er^{3+} ions limited energy transfer to Er^{3+}. Consequently, the cross-relaxation effect was less prominent, resulting in green luminescence dominated by the $^2H_{11/2}$, $^4S_{3/2}$–$^4I_{15/2}$ transition of Er^{3+} (Fig. 13d).

3.4.3 Metal ion doping. Metal ion doping, such as Li$^+$, Ca^{2+}, Fe^{3+}, Zn^{2+}, Mn^{2+} and Na$^+$, into the lattice could improve upconverting and downconverting luminescence through different mechanisms.[103,128–134] On the other hand, PLNP intensity and afterglow time are enhanced by creating defects in the crystal lattice.[135]

Substituting NaYF$_4$:Yb^{3+}/Tm^{3+} with Ca^{2+} caused a 121-fold improvement in upconversion luminescence intensity.[129] This is because the substitution of Ca^{2+} ions with Y^{3+} in the lattice inhibits the migration and rearrangement of dislocations, thereby suppressing the formation of small-angle grain boundaries. This enhances the optical homogeneity of the crystal and improves upconversion luminescence. Doping Y^{3+} into CaF$_2$:Nd^{3+} was also shown to improve downconversion luminescence by

2.38-fold, since it could bind with Nd^{3+} and prevent the formation of aggregated inactive Nd^{3+}–Nd^{3+} clusters.[136] Doping Li$^+$ or Na$^+$ caused crystal shrinkage which also enhanced luminescence enhancement.[128,134] For example, Li$^+$ easily substituted Gd^{3+} ions in GdF$_3$:Yb^{3+},Tm^{3+}, creating defects $\left(\text{Li}''_{\text{Gd}}\right)$ that can be electrically neutralized by F$^-$ vacancies $\left(\text{V}^{\bullet\bullet}_{\text{F}}\right)$. This substitution and neutralization induced the contraction of the crystal cell of GdF$_3$, reducing symmetry around Tm^{3+} and increasing the probability of radiative transitions. As a result, under 980 nm excitation, the emission intensity at 800 nm and 474 nm increased 2.2 and 5.2 times, respectively, under 3% of Li$^+$ doping. Ferroelectric polarization of LiNbO$_3$:Yb^{3+},Tm^{3+} also enhanced upconversion and downconversion luminescence by 2.6 and 3.2 times through deliberately causing crystal shrinkage.[137] Upon application of an increasing electric field to the LiNbO$_3$:Yb^{3+},Tm^{3+}, the lattice was found to shrink by 0.03 Å.

Doping certain lanthanide ions could also improve luminescence intensity *via* energy transfer processes. Doping NaYF$_4$:Yb^{3+},Tb^{3+} with Mn^{2+} ions could increase the upconversion emission of Tb^{3+} ions by over 30 times due to the more efficient energy transfer between the sensitiser and activator.[75] Energy is transferred from excited Yb^{3+} ions to Mn^{2+} ions and then to the $^5D_4$ state of Tb^{3+} ions, which resulted in stronger luminescence following relaxation. In another study, the downconversion luminescence of NaYbF$_4$:Er^{3+},Nd^{3+} was enhanced through the suppression of upconversion luminescence by Ce^{3+} doping.[138] Initially, Nd^{3+} ions absorbed the excitation energy at 808 nm and transmitted it to Yb^{3+} ions to excite Er^{3+}, resulting in downconversion luminescence at 1530 nm by $^4I_{13/2}$–$^4I_{15/2}$ (Fig. 14a). Concurrently, a competing process occurs where the $^4I_{11/2}$ level of Er^{3+} is excited to its higher $^2H_{11/2}$ and $^4S_{3/2}$ levels for upconversion emission. The similar energy gap between $^2F_{5/2}$–$^2F_{7/2}$ of Ce^{3+} and $^4I_{11/2}$–$^4I_{13/2}$ of Er^{3+} allowed Ce^{3+} to absorb energy from Er^{3+}, causing them to relax from $^4I_{11/2}$ to $^4I_{13/2}$ (Fig. 14c and d). The emission peak at 1530 nm for the nanoparticles doped with 5% Ce^{3+} was 10.4 times higher than that of nanoparticles without Ce^{3+} (Fig. 14b).

3.4.4 Plasmonic enhancement effect. Metal is known for its plasmonic effect, and studies have demonstrated the sensitization of gold or silver with upconversion nanoparticles enhanced the luminescence intensity.[139,140] The convergence of localized surface plasmon resonance (SPR) bands of metals and the excitation bands of upconversion nanoparticles can lead to remarkably efficient luminescence.[141] For example, coating gold nanorods on NaYF$_4$:Yb^{3+},Er^{3+}@NaYF$_4$@NaYF$_4$:Yb^{3+},Nd^{3+},Tm^{3+} caused an enhancement in upconversion luminescence of 2.4×10^4-fold, 2.2×10^4-fold, and 1.6×10^4-fold following 808 nm, 980 nm, and 1540 nm excitation, respectively.[142] Gold nanorods could also improve the downconversion luminescence of Nd$_2$O$_3$ by the strong local electromagnetic field around AuNRs.[143] In addition, the conjugation of semiconducting W$_{18}$O$_{49}$ nanowires with NaYF$_4$:Yb^{3+},Er^{3+} exhibited two orders of green upconversion enhancement.[144] This is because W$_{18}$O$_{49}$ converted incident NIR light into local SPR oscillation energy, which was subsequently transferred to NaYF$_4$:Yb^{3+},Er^{3+} due to the overlap between the 2 energy bands. Excited states of Er^{3+} were populated and upconversion luminescence intensity was enhanced.
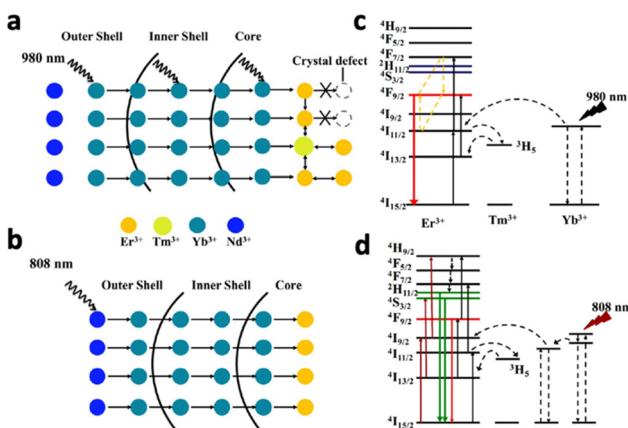
Fig. 13 Schematic illustration of energy migration pathways of NaErF$_4$:Yb/Tm@NaYF$_4$:Yb@NaNdF$_4$:Yb under (a) 980 and (b) 808 nm excitations. Proposed upconversion mechanism for (c) red emission generated under 980 nm laser excitation and (d) green emission under 808 nm laser excitation. Reproduced with permission from ref. 127. Copyright 2019, American Chemical Society.

2910 | *Chem. Soc. Rev.*, 2024, **53**, 2898–2931

This journal is © The Royal Society of Chemistry 2024
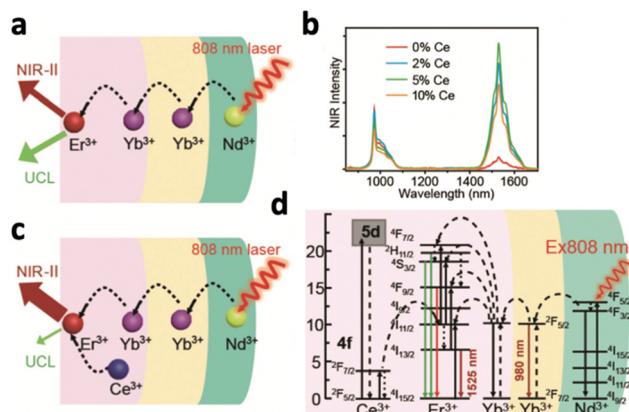
Fig. 14 (a) Schematic illustration of the energy transfer path from Nd^{3+} to inner Er^{3+} for luminescence without (a) and with (c) Ce^{3+}-ion doping. (b) The downconverting NIR fluorescence spectra of $NaYbF_4$:2% Er,y% Ce@NaYF_4$:10% Yb@NaYF_4$:50% Nd (y = 0, 2, 5, and 10). (d) Detailed illustration of the energy transfer from Nd^{3+} to Er^{3+}, emitting NIR-II luminescence at 1525 nm under 808 nm excitation. Reproduced with permission from ref. 138. Copyright 2020, Royal Society of Chemistry.

3.4.5 Dye sensitization. Many dyes and quantum dots have their absorption bands located in the NIR region, and they possess higher quantum yields and surface area compared to the rare earth ions in UCNPs or DCNPs.[145,146] The sensitization by these dyes enhanced energy absorption of the UCNPs/DCNPs, leading to enhanced luminescence. For example, IR-808-sensitized $NaGdF_4$:Yb,Ho,Ce@NaYF_4$:Nd,Yb was shown to exhibit over 100-fold enhancement in upconversion luminescence.[147] Ag_2Se quantum dot-sensitized Yb^{3+}/Er^{3+}-doped UCNPs also showed 19-fold luminescence enhancement.[148] An organic dye Alk-pi also enhanced upconversion luminescence by 600-fold and downconversion luminescence by 40-fold after sensitizing with Er^{3+}/Ce^{3+}@NaYF_4$:Nd^{3+}$.[149]

3.5 NIR-activated light-mediated therapy

NIR light possesses sufficient tissue penetration depth to carry out light-mediated therapy in deep tissue. However, certain NIR wavelengths possess deeper tissue penetration than the other wavelengths, such as NIR light located at around 800 nm or NIR-II light. Therefore, an increasing number of studies have focused on engineering 808 nm or NIR-II-excitable upconversion or downconversion nanomaterials for therapy and imaging respectively. In addition, NIR-IIb and NIR-IIc photons, or magnetic resonance imaging (MRI) are mostly used for imaging-guidance of deep tissue therapy due to their ability to produce high resolution images in deep tissues. Orthogonal excitations were also applied in various therapies since different modalities of the system, *i.e.*, therapy and imaging, could be activated with different excitation wavelength. Finally, better targeting strategies were developed such that the nanosystem is only "activated" in the tumour, minimizing damage to normal cells.

In this section, we will cover the major directions of NIR-activated light-based therapy and their challenges.

3.5.1 Photodynamic therapy. Upconversion nanoparticles are a promising candidate for photodynamic therapy, due to their ability to emit visible light following NIR excitation, which could activate various photosensitizers to produce singlet oxygen.

The initial application of UCNPs for photodynamic therapy was limited by the loading rate of photosensitizers onto the UCNP.[150] In addition, the desorption and leakage of PSs from the nanoplatform is also a big concern, since most rely on the electrostatic or hydrophobic interaction between the UCNP and photosensitizers.[151] This issue was solved by Zhang's group in 2012 as they covalently linked photosensitizers with the UCNP $NaYF_4$:Yb^{3+},Er^{3+}$, with 100 photosensitizing molecules covalently bonded to every 20 nm UCNP.[152]

To achieve deep-tissue therapy, it is crucial to engineer nanosystems that could be excited by highly penetrative NIR-II photons. Zeng *et al.* recently reported $NaLuF_4$:40% Mn20% Er@NaLuF_4$@SiO_2$.[7] Upon 1532 irradiation, Er^{3+} was excited to $^2H_{11/2}$, emitting red light following $^4F_{9/2}$ to $^4I_{15/2}$ transition, which activated the photosensitizer ZnPc to produce singlet oxygen. The red upconversion luminescence was also utilised for imaging guidance *in vivo* following both oral administration and subcutaneous injection. To enhance imaging depth and resolution, NIR-II photons at 1500 nm were produced from $NaYF_4$:Yb^{3+},Er^{3+}$ through downconversion luminescence following 980 nm activation.[153] The imaging modality successfully produced angiography of the hindlimb blood vessels and visualized the liver of a mice following a 2 mg injection with a low NIR power density of 0.5 W cm^{-2}. To enhance image resolution, MRI was used to image Gd^{3+}-containing UCNPs due to the T_1-weighted MRI properties of Gd^{3+}.[154] For example, Wu *et al.* produced $NaGdF_4$:Yb/Tm@SiO_2@TiO_2$ nanocomposites, which displayed a high r_1 relaxivity value of 4.53 mM^{-1} s^{-1}.[74] Despite having higher resolution, the high cost and complexity and MRI has to be taken under consideration.

Orthogonal excitation allows the UCNPs to be excited by 2 different wavelengths, producing 2 different emissions wavelengths – one for PDT and one for imaging/diagnosis.[127,155] For example, $GdOF$:Yb^{3+},Er^{3+},Eu^{3+}$ coupled with the photosensitizer DHA could carry out PDT and produce NIR-II imaging with orthogonal excitation.[156] Under 980 nm NIR irradiation, the Er^{3+} ions were excited and produced red emissions at 550 nm and 650 nm, which excited DHA to produce singlet oxygen, inducing tumour ablation *in vivo* after 14 days of treatment. Following 808 nm laser irradiation, Er^{3+} produced downconverting NIR-II emissions at 1530 nm, which was observed clearly at the tumour site following intravenous injection of the UCNP in mice.

To enhance tumour cells uptake of the nanoparticles, targeting ligands like folate have been conjugated on UCNPs.[157,158] Instead of using targeting ligands, magnetic field was shown to increase the cell uptake of transferrin-coated $NaYF_4$:Gd^{3+},Yb^{3+},Er^{3+}$ loaded with the photosensitizer PpIX on MDA-MB-231 and HeLa cells *in vitro*.[159] *In vivo* injection of UCNPs coated with Fe_3O_4 while placing external magnets near the tumour area also enhanced the accumulation of UCNPs in tumour cells and increased PDT efficacy.[6]

Persistent luminescence nanoparticles (PLNPs) do not require constant irradiation for continuous emission, which

This journal is © The Royal Society of Chemistry 2024

Chem. Soc. Rev., 2024, **53**, 2898–2931 | **2911**
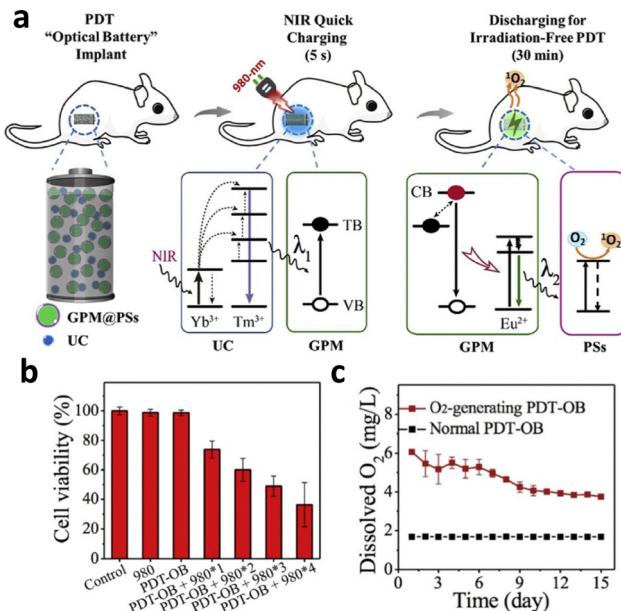
Fig. 15 (a) Schematic illustration of the NIR-excited PDT with persistent luminescence (GPM: green persistent luminescence materials; PSs: photosensitizers; UC: upconversion materials; TB: trapping band; and VB: valence band). (b) Viability of HT_29 cells treated with different numbers of 980 nm NIR recharging cycles. (c) *In vitro* comparison of O_2 generation ability between CaO_2-containing implants and CaO_2-free implants. Reproduced with permission from ref. 110. Copyright 2018, Elsevier.

reduces irradiation time and minimizes the side effects of NIR irradiation on tissue. The physical combination of the UCNP $NaYF_4:Yb^{3+},Tm^{3+}$ and PLNP $SrAl_2O_4:2\%\ Eu^{2+},4\%\ Dy^{3+}$ resulted in the emission of persistent luminescence at 520 nm following 980 nm excitation.[110] After 5 minutes of 980 nm charging, the nanophosphors emitted light for 30 minutes, resulting in the excitation of photosensitizers for PDT (Fig. 15a). A high degree of singlet oxygen generation resulted in 60% reduction in cell viability of HT_29 cells after 4 cycles of irradiation (Fig. 15b). To combat the hypoxia environment in the tumour, the nanosystem encapsulated CaO_2, which reacted with water to generate oxygen. Higher oxygen content and oxygenated hemoglobin of the tumours was reported *in vitro*, which resulted in increased generation of singlet oxygen and reduction in tumour volume (Fig. 15c).

3.5.2 Photothermal therapy. UCNPs/DCNPs were applied to induce PTT, provide imaging modalities or both through orthogonal excitation. Photothermal agents that also carry imaging modalities are favourable since it simplifies the design of the nanosystem.

Gd^{3+}-Doped upconverting/downconverting nanoparticles exhibit T_2-enhanced MRI modalities that could be used as an image-guidance for PTT.[86,160] Fe_3O_4, having high T_2 relaxation time, exhibits MRI modalities while being a photothermal agent itself. A hollow carbon sphere containing Fe_3O_4 and $NaGdF_4:Yb^{3+},Er^{3+}@NaGdF_4$ UCNPs exhibited a r_2 value of 845.13 $mM^{-1}\ s^{-1}$, indicating their effectiveness as a T_2 contrast agent.[56] Under external magnetic field, the nanoparticles exhibited enhanced accumulation at the tumour site. 980 nm laser

irradiation on the nanosystem resulted in visible upconversion emission that excited Fe_3O_4. Tumour temperature increased and a complete elimination of tumour was observed following treatment. To minimise energy loss during transfer between UCNPs and the photothermal agent, Hao *et al.* developed carbon dots that produce NIR-II emission in the range of 900–1200 nm under 808 nm excitation while acting as a photothermal agent.[65] The CDs showed a high quantum yield (QY) of approximately 0.4% and a photothermal conversion efficiency of 30.6%, which resulted in the near-disappearance of tumour after 6 days of 10-minute 808 nm irradiation daily.

Orthogonal excitation/emission was also applied in PTT to trigger therapy and imaging separately. Chen *et al.* produced prussian blue (PB)-coated $NaErF_4@NaYF_4@NaNdF_4$ that could emit different downconversion luminescence under 808 and 980 nm excitation (Fig. 16a).[65] Under 808 nm excitation, Nd^{3+} was excited to produce 1064 nm emission, which activated PB to generate heat (Fig. 16c). The PEGylated nanosystem at 600 μg mL^{-1} raised the tumour temperature above 42 °C for 10 minutes, significantly more than the water and the nanosystem without PB (Fig. 16d). *In vivo* studies confirmed the prominent tumour cell ablation and significant reduction in tumour volume compared to other the control groups (Fig. 16e). On the other hand, 980 nm excitation caused Er^{3+} to produce emission at 1525 nm, which provided a clear, high-resolution and high-contrast image of miniature blood vessels, brain tissue, and internal organs in *in vivo* imaging (Fig. 16b and f). Even with a 2-fold higher laser power and 80-fold longer integration time, 1064 nm luminescence exhibited lower resolution and could only capture an unclear image (Fig. 16g). This further highlights the importance of using NIR-IIb or NIR-IIc luminescence for imaging-guided therapy.

3.5.3 Drug delivery. NIR light has been applied extensively to activate upconversion or downconversion nanoparticles to trigger drug delivery or provide imaging modalities.

Trans platinum complex *trans,trans,trans*-$[Pt(N_3)_2$-$(NH_3)(py)(O_2CCH_2CH_2COOH)_2]$ (DPP) could be activated by UV/blue light to yield toxic platinum complexes, which could achieve cancer chemotherapy.[161,162] Therefore, DPP was conjugated onto the surface of $NaYF_4:Yb^{3+},Tm^{3+}@NaGdF:Yb^{3+}$ UCNPs, where a 980 nm laser activated the UCNPs to produce UV emissions, triggering the generation of toxic platinum complexes and caused significant tumour inhibition *in vivo*.[119] Apart from directly generating toxic substances, UCNPs could trigger drug release from nanocomposites with the use of photothermal effect.[163] For example, Yang *et al.* assembled $Gd_2O_3:Yb^{3+},Er^{3+}$ in mesoporous silica loaded with gold nanocrystals and the target drug doxorubicin (Dox).[164] Upon 980 nm excitation, the UCNPs emitted green light, which overlapped with the surface plasmon resonance (SPR) band of gold nanoparticles. This caused the gold nanocrystals to generate heat and release the loaded Dox, while the elevated tissue temperature enhanced the cellular uptake of Dox.

UCNPs were also applied to provide imaging guidance for drug delivery, but most of them do not provide imaging specifically for the site of drug release.[67,163] To enhance the

2912 | *Chem. Soc. Rev.*, 2024, **53**, 2898–2931

This journal is © The Royal Society of Chemistry 2024
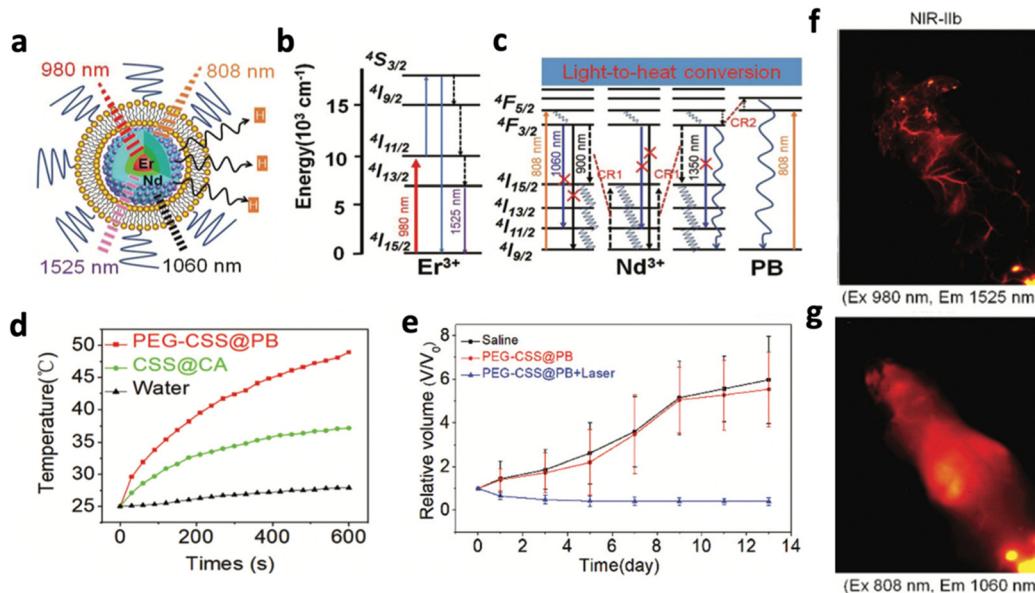
Fig. 16 Schematic illustrations of (a) the design of NaErF$_4$@NaYF$_4$@NaNdF$_4$ exhibiting NIR-II luminescence under orthogonal excitation, (b) energy transition diagrams of the 1525 nm luminescence of Er^{3+} under 980 nm excitation and (c) energy transition diagrams of the 1060 nm luminescence of Nd^{3+} under 808 nm excitation, with cross-relaxation pathways between Nd^{3+} ions and Nd^{3+} ions with PB. (d) Comparison of temperature increases of the PEG-CSS@PB nanocomposite, CSS@CA nanocomposite and water, excited by a 808 nm laser (1 W cm^{-2}). (e) Comparison of tumour volume following different groups of treatment. *In vivo* NIR II luminescence imaging of the mouse with a tail vein injection of PEG-CSS@PB, acquired with (f) 1525 nm and (g) 1064 nm luminescence. Reproduced with permission from ref. 65. Copyright 2019, Royal Society of Chemistry.

specificity of imaging, a nanosystem consisting of UCNPs coated with dye-doped and drug-loaded macroporous silica shells protected by hyaluronic acid (HA) was developed.[165] While intact, the Ho^{3+}-containing UCNPs produced 660 nm upconversion under 980 nm excitation, which excited the doped Cy5.5 dye to emit at 710 nm. Following specific degradation by hyaluronidase in tumour cells, the nanosystem disintegrated and released the drug load while restoring luminescence at 660 nm. Intratumoural injection of this nanosystem displayed no signal at 660 nm for the first 48 hours but started showing increasing intensity after 48 hours, which indicated a specific and progressive drug release. To enhance the resolution and imaging depth, a NIR-II emitting Nd^{3+}-MOF loaded with chloroquine (CQ) and coated with HA was developed.[166] Following 808 nm excitation, Nd-MOF crystals exhibited emissions at 1064 and 1337 nm in the NIR-II region, which peaked 12 hours after intravenous injection *in vivo*.

3.5.4 Combinational therapy. Combining more than 1 therapeutic modality into a single nanosystem could lead to better therapeutic effect. In this section, we will discuss 3 major combinational light-mediated therapies in cancer: photothermal–chemotherapy, photodynamic–chemotherapy and photothermal–photodynamic therapy.

Photothermal therapy and chemotherapy could be combined by making use of drug delivery systems that release drugs upon an increase in temperature. For example, NaGdF$_4$:Yb/Er@NaGdF$_4$ UCNPs were functionalised with mesoporous silica shells, and loaded with doxorubicin (DOX) and gold nanoparticles.[167] Upon 980 nm laser irradiation, the green emission from UCNPs excited gold nanoparticles due to SPR band overlap, causing a rise in

temperature to 70.7 °C after 7 min of the irradiation while simultaneously releasing the drug. The presence of gold nanoparticles caused an increase in DOX release efficiency from 38.6% to 78.9%. To provide an imaging modality for this combinational therapy, Nd^{3+}-based downconversion nanoparticles were conjugated with CuS and Dox. 808 nm irradiation not only excited CuS to generate heat but also excited Nd^{3+} to emit NIR-II fluorescence at 1064 nm. Following 8 minutes of irradiation, the nanosystem exhibited a 5.1 °C temperature rise, releasing Dox and reducing the cell viability of 4T$_1$ cells from 90% to 40% *in vitro*. The axillary lymph nodes in breast tumour exhibited clear fluorescence 1 hour post-injection *in vivo* and remained evident for 4 hours with high contrast.

By loading drugs together with UCNPs and photosensitizers, PDT efficacy could be enhanced without the need to increase oxygen level in tumour tissue.[168,169] Similar to photothermal–chemotherapy, it is important to incorporate drug release systems that are also triggered by NIR irradiation, to minimize side effects on healthy cells. Gong *et al.* coloaded NaYF$_4$:Yb^{3+}, Tm^{3+},Er^{3+} UCNPs with the photosensitiser Rose Bengal (RB) and hydrophobic drug AB3 inside the polymer PNBMA.[170] The red upconversion at 650 nm induced by Er^{3+} activated RB to generate singlet oxygen, while the UV upconversion by Tm^{3+} triggered the PNBMA to undergo a hydrophobic-to-hydrophilic transition, releasing the hydrophobic drug AB3. The targeted combinational therapy displayed remarkable antitumour effects, outperforming the individual treatments of chemotherapy or PDT.

By combining photothermal therapy and photodynamic therapy, the heat generated in PTT improved blood flow to

This journal is © The Royal Society of Chemistry 2024

Chem. Soc. Rev., 2024, **53**, 2898–2931 | **2913**

the tumour area, enhancing the intratumoural oxygen level and promoting PDT.[171] Therefore, photothermal agents with higher surface area to bind with UCNPs and photosensitizers have been explored. For example, MoS_2 nanosheets could be excited directly by an 808 nm laser (1 W cm^{-2}) to produce heat that could reach 55.3 °C after 60 min of irradiation.[172] Nanographene oxide (NGO) was also shown to increase temperature to 65 °C within 2 minutes of 808 nm irradiation.[125] MoS_2 and NGO both exhibit a large surface area and ability to covalently graft with UCNPs as well as photosensitisers like Ce6 or ZnPc.[172,173] To simplify the synthesis process, photothermal agents that could generate ROS under NIR irradiation have been studied. For example, FePc can emit ROS and exhibits a photothermal conversion efficiency of 42.5% under 730 nm irradiation.[174] In addition, the photothermal agent $Cu_{2-x}S$ nanodots caused a 52 °C temperature increase under 1064 nm irradiation, while generating hydroxyl radicals through a Fenton-like reaction with H_2O_2.[175]

3.6 Strengths and weaknesses of the NIR-mediated therapy

NIR-activated therapy has several strengths that contribute to its growing popularity in biomedical applications. One of the main advantages is the higher tissue penetration capability of NIR light compared to conventional UV/visible sources. Certain NIR wavelengths fall within the "optical window" of biological tissues, allowing them to penetrate deeper than UV/visible light into biological tissues for light-mediated therapy. Another advantage of NIR-activated therapy is that NIR provides the versatility to tune the wavelength for specific purposes. For example, 808 nm excitation wavelength could be used instead of 980 nm for deeper tissue penetration; NIR-IIb or NIR-IIc emission wavelength could be used for high-resolution deep-tissue imaging. In addition, orthogonal excitation in several nanosystems allowed them to produce different emission wavelengths that perform different functions, such as therapy or imaging. The orthogonal emissions at 2 different wavelengths could also be monitored simultaneously to track 2 processes together. Additionally, NIR-activated therapy benefits from the widespread availability of equipment. NIR light sources and detectors are readily found in many research laboratories and clinical settings. This accessibility makes it easier for researchers and clinicians to implement NIR-activated therapy in their studies and medical practices. In contrast to chemiluminescence-activated therapy, NIR-activated therapy offers the advantage of external control over the activation and deactivation of luminescence. This capability allows for the precise modulation of the luminescent signal. Furthermore, NIR-activated luminescence typically exhibits stronger intensity than chemiluminescence-based approaches, enabling more effective therapeutic outcomes.

However, NIR-activated therapy has certain limitations and disadvantages that need to be considered. NIR light can generate heat when absorbed by tissues, which may lead to thermal damage in surrounding healthy tissues. Careful control over the NIR light dosage and monitoring of tissue temperature are essential to mitigate the risk of overheating and ensure the safety of the therapy. Another limitation is the depth of tissue penetration. While NIR light offers higher tissue penetration than UV and visible light, its penetration depth is still limited compared to other excitation sources like X-rays and ultrasound. This constraint restricts the treatment of deep-seated tissues and tumours.

4. X-ray-excited luminescence

X-rays, having higher tissue penetration than most of the other excitation modalities, could activate many nanosystems to carry out light-mediated therapeutics in deep tissue. The generation of X-ray-excited luminescence is usually dependent on the direct ejection of electrons. High energy X-ray photons eject electrons in atomic orbitals that results in the creation of holes, where subsequent filling of these holes by electrons from higher orbitals results in X-ray fluorescence.[176] However, the efficiency of this process is heavily dependent on the electronic structure of the atom, since competing processes may occur, such as Compton scattering, Rayleigh scattering or emission of Auger electrons.[177]

4.1 X-ray-excitable luminescent nanomaterials

X-ray-responsive nanomaterials typically comprise elements with high atomic numbers, characterized by significant X-ray attenuation coefficients. These nanomaterials can efficiently absorb X-rays and generate luminescence. Hence, most X-ray excitable luminescent nanomaterials consist of lanthanides and heavy metals due to their high atomic number. In addition, certain semiconductors and organic nanomaterials exhibit X-ray excitable luminescence due to the direct band-to-band excitation by X-rays. However, they are less studied due to their lower X-ray absorption coefficients.

Different from NIR-excited luminescence, most X-ray-excited luminescent nanomaterials do not require a sensitiser, since X-rays have enough energy to cause a direct band-to-band excitation (Fig. 17a and b). In contrast, certain sensitisers, such as Yb^{3+}, may even quench X-ray luminescence through cross-relaxation and charge trapping processes.[178] Band-to-band excitation by X-rays allows many nanomaterials to emit in the visible range or even in the deep UV range with strong intensity, with or without the presence of an activator. This would be beneficial for activating light-sensitive molecules like photosensitisers, or cause direct UV damage to the target cells.

4.1.1 Lanthanide-based nanomaterials. Lanthanide-based nanomaterials were well-studied in NIR-excitable luminescence due to their f–f transitions and ladder-like energy levels. Interestingly, lanthanide-based nanomaterials, having high atomic numbers and X-ray attenuation coefficients, serve as good candidates for absorbing X-rays and exhibiting X-ray-excited luminescence. Crystal lattices with high material density that favour the incorporation of lanthanide ions are usually chosen, such as $NaLnF_4$, Ln_2O_3, LnF_3, LnOCl, etc.[179–182] In particular, lanthanide ions that exhibit prominent X-ray absorption include Gd^{3+}, La^{3+}, Ce^{3+}, Lu^{3+}, Nd^{3+}, Y^{3+} and Hf^{3+}. These lanthanide ions typically eject the electron located in the 4f orbital, which results in a hole in the 4f orbital. An electron

2914 | *Chem. Soc. Rev.*, 2024, **53**, 2898–2931

This journal is © The Royal Society of Chemistry 2024
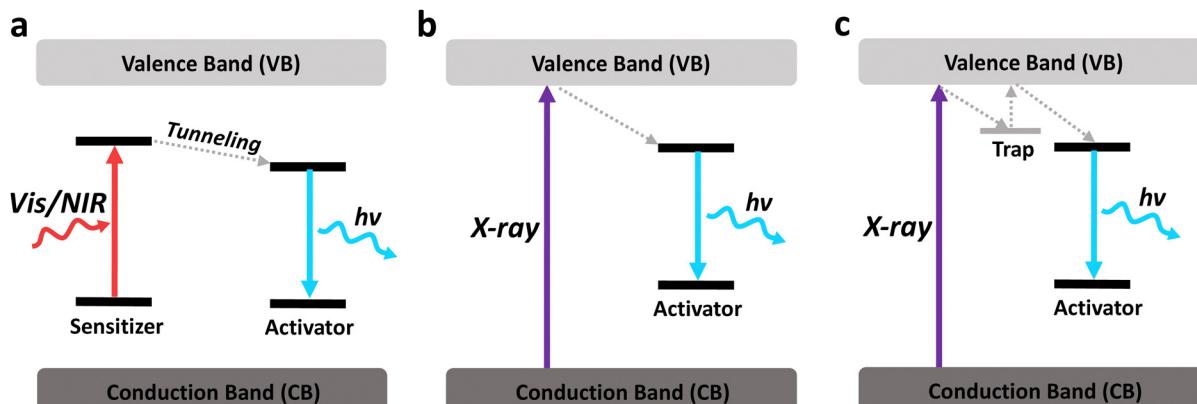
Fig. 17 Schematic illustrations of the typical mechanisms of (a) downconversion luminescence upon excitation with visible or NIR light, (b) X-ray-excited luminescence and (c) X-ray-excited persistent luminescence.

from the 5d orbital is usually used to fill the hole in the 4f orbital, releasing energy and relaying it to the activator ions.[183]

Activator ions that have energy levels located near the 5d orbital are often chosen to accept energy from the excited host crystal to emit light of different wavelengths. Eu^{3+}, for example, gives red luminescence at 592 nm ($^5D_0$–$^7F_1$), 618 nm ($^5D_0$–$^7F_2$) and 698 nm ($^5D_0$–$^7F_4$).[184] Sm^{3+} gives red luminescence at 554 nm ($^4G_{5/2}$–$^6H_{9/2}$), 596 nm ($^4G_{5/2}$–$^6H_{7/2}$), 646 nm ($^4G_{5/2}$–$^6H_{5/2}$) and 708 nm ($^4G_{5/2}$–$^6H_{3/2}$).[185] Tb^{3+} gives green emission at 490 nm ($^5D_4$–$^7F_6$), 545 nm ($^5D_4$–$^7F_5$), 585 nm ($^5D_4$–$^7F_4$) and 621 nm ($^5D_3$–$^7F_6$).[186] Gd^{3+} is often co-doped with Tb^{3+} to facilitate the energy transfer from 5d electrons to Tb^{3+} ions, since ^6I_J and ^6P_J energy levels of Gd^{3+} are located close to the $^5D_4$ level of Tb^{3+}.[183]

Due to the high energy of X-rays, they can excite many lanthanide ions inducing emission of light in the UV range. For example, Pr^{3+} is capable of emitting light in the UVC spectrum at 235, 245, 263, and 274 nm, attributed to the characteristic inter-configurational $4f^15d^1$–$4f^2$ transition in Pr^{3+}.[187] Ce^{3+} ions can also emit UV at 360 nm due the transition from the lowest level of the 5d configuration to the $^2F_{5/2}$ and $^2F_{7/2}$ levels.[188] Tm^{3+} ions are also known for their UV emissions at 353 and 368 nm due to the $^3P_0$–$^3F_4$ and $^1D_2$–$^3H_6$ transitions, accompanied by NIR emission at 807 nm due to the $^3H_4$–$^3H_6$ transition of Tm^{3+} ions.[189,190] Not only can UV emissions activate most of the photosensitive molecules for deep tissue therapy, but they can also directly cause DNA damage in the targeted tissue while minimizing the damage to surrounding tissues due to their low biological penetration.[187]

4.1.2 Metal-based nanomaterials. Other than lanthanides, certain heavy metal-based nanomaterials can absorb X-rays efficiently. These nanomaterials usually contain heavy metals that possess a high atomic number, including compounds like $BaAl_2O_4:Eu^{3+}$, $CaF_2:Ce^{3+},Tb^{3+}$, $CsMnCl_3:Pb^{3+}$, and $SrAl_2O_4:Eu^{2+}$.[191–194] The host crystal lattice with a high atomic number absorbs X-rays and transfers the energy to the doped lanthanide activators, resulting in visible or even NIR emission, as shown in $LiGa_5O_8:Cr^{3+}$.[195] In addition to utilizing lanthanide ions as activators, Zr^{4+} in Zr-based metal–organic framework can also transfer the energy to the organic ligand (H_4ETTC), resulting in

luminescence emission at 550 nm due to the ejection of inner-shell electrons in Zr^{4+}.[196]

However, different from most lanthanide-based nanomaterials, metal-based compounds can emit X-ray-excited luminescence even without the addition of activator ions. Although offering more simplicity in design, metal-based nanomaterials usually produce broader emissions with less tunability in emission wavelength. For example, GSH-Au NPs were first shown to exhibit X-ray-excited luminescence at 645 nm and 800 nm in 2013 by Chen *et al.*, as X-ray photons above the L3 absorption edge of Au (~12 keV) have sufficient energy to knock out the inner-shell electrons.[197] In order to alter emission wavelengths of Au NPs, changes in thir surface modifications have to be made. For example, bovine serum albumin (BSA)-directed Au nanoclusters produced an emission at 667 nm while lysozyme-coated Au nanoclusters produced an emission at 421 nm.[198] This is due to the varying degrees of inelastic scattering between the electrons in the organic coating and the ejected photoelectrons, resulting in different levels of hole–electron generation. In addition, the conjugation of activator-based organic compound europium bromoacetate (EuBA) onto Au nanorods resulted in an emission shift to around 630 nm.[199] Similarly, copper–cysteamine nanoparticles also exhibited 645 nm emission following X-ray excitation.[200] Other than gold and copper, molybdenum (Mo_6) complexes also have a high atomic number and have demonstrated emissions at 690 nm with ethylene oxide surface modification following X-ray irradiation.[201]

Other than metal nanoparticles, metal oxides were also found to exhibit X-ray excited luminescence due to their large band gap and the presence of bulk and surface defect sites.[202] For example, Al_2O_3 nanotubes, TiO_2 NPs and ZnO NPs exhibited X-ray excited luminescence due to their oxygen vacancies.[203–205] ZnO gives an emission at 382 nm and 510 nm following X-ray excitation, where the former is due to band-gap emission (3.24 eV) and the latter is due to oxygen vacancies.[205] Similarly, X-ray excitation of ZnS NPs resulted in UV emission at 330 nm.[206] Combining several heavy metals together in a nanocomposite could also result in efficient X-ray absorption. Shan *et al.*

This journal is © The Royal Society of Chemistry 2024

Chem. Soc. Rev., 2024, **53**, 2898–2931 | **2915**

reported $CsZrCl_6$, which gave an emission peak at 464 nm, mainly due to the recombination of triplet states.[207] The accumulation of triplet states within the nanocomposite could also boost its ability to generate ROS, which could be applied in many ROS-based therapies.

4.1.3 Persistent luminescent nanomaterials. X-ray-activated persistent luminescent nanoparticles (PLNPs) are promising for deep tissue light-mediated therapeutics. This is because X-rays can activate the PLNPs in deep tissue, generating strong and long-lasting afterglow luminescence.[208] In general, the 2 most studied systems are $ZnGa_2O_4$-based nanosystems and $NaLnF_4$-based nanosystems.

Zinc-based nanosystems are favourable for X-ray excited afterglow luminescence due to their high X-ray absorption coefficient. For example, ZnS:Cu,Co-A was reported to emit 578 nm under X-ray irradiation, but afterglow luminescence time was just 10 minutes long.[209] To improve the X-ray excited afterglow of the nanosystem, other Zn-based nanosystems were developed, namely, zinc gallate ($ZnGa_2O_4$), zinc silicate ($ZnSi_2O_4$), or variations of zinc gallogermanate.[210] X-ray-activated $ZnGa_2O_4$:Cr^{3+} was first discovered in 2017 by Hao's group.[211] They reported $ZnGa_2O_4$:Cr^{3+}, which exhibited 6 hours of persistent luminescence at 700 nm after the cessation of the soft X-ray excitation source with low excitation power (45 kVp, 0.5 mA), due to the characteristic electron transition of Cr^{3+} from ^2E to $^4A_2$ (Fig. 18a and b). Although this nanosystem was originally discovered for UV-excitation, X-ray excitation increased the penetration depth from 3 mm to 20 mm (Fig. 18c). More importantly, the PLNPs could be recharged with the same X-ray dosage without a decrease in luminescence intensity. Later on, work has beencarried out to further

Fig. 18 (a) Excitation spectrum (black) and emission spectrum (red) of $ZnGa_2O_4$:Cr^{3+}. (b) 4 Cycles of persistent luminescence decay curves by $ZnGa_2O_4$:Cr^{3+} following cessation of X-ray irradiation (5 min, 45 kVp). (c) Luminescence intensity of $ZnGa_2O_4$:Cr^{3+} excited by X-ray (blue) and 365 nm UV (red) through pork tissues with different thicknesses (0, 1, 3, 5, 10, and 20 mm). Reproduced with permission from ref. 211. Copyright 2017, American Chemical Society.

optimise this nanosystem. For example, tungsten W(VI) was doped to improve X-ray absorption, which resulted in a 1.3-fold increase in luminescence intensity due to the additional electrons ejected.[106] The afterglow lifetime was also increased due to the readjustment of trap depth and density by W(VI). Mn^{2+} was also doped into $ZnGa_2O_4$ to shift the emission to from 700 nm to 530 nm, due to the transition of Mn^{2+} from $^4T_1$ to $^6A_1$.[212]

Zinc gallogermanate, having different variations, is synthesized by doping germanium(IV) into zinc gallate. Zn_3Ga_2-Ge_2O_{10}:0.5% Cr^{3+},0.1% Mn^{2+} was produced to generate red luminescence at 698 nm and green luminescence at 532 nm due to the transitions of Cr^{3+} and Mn^{2+}.[213] This nanosystem is particularly useful due to its ability to generate visible and NIR afterglow emissions, which could be used to activate photosensitisers and carry out deep tissue imaging guidance simultaneously. To enhance the resolution of imaging guidance, Liu et al. developed $Zn_2Ga_3Ge_{0.75}O_8$:Cr^{3+},Nd^{3+} that exhibited NIR-I and NIR-II afterglow following X-ray irradiation.[214] Not only did the nanoparticle exhibit emissions at 696 nm due to Cr^{3+}, the presence of Nd^{3+} resulted in emissions at 895, 1067 and 1340 nm, originating from the $^4F_{3/2}$–$^4I_{9/2}$, $^4F_{3/2}$–$^4I_{11/2}$, and $^4F_{3/2}$–$^4I_{13/2}$ transitions of Nd^{3+}. Following cessation of X-ray irradiation, the 700 nm afterglow peak of Cr^{3+} (^2E–$^4A_2$) partly overlaps with the absorption peaks of Nd^{3+} at 745 nm ($^4I_{9/2}$–$^4F_{7/2}$ + $^4S_{3/2}$) and 805 nm ($^4I_{9/2}$–$^4F_{5/2}$ + $^2H_{9/2}$). The energy transfer from Cr^{3+} to Nd^{3+} enabled afterglow luminescence at 696 nm and 1067 nm for 800 and 10 min, respectively. Besides Nd^{3+}, Yb^{3+} also serves as a good candidate for NIR-II emission in the 950–1150 nm range, attributed to its phonon-assisted transition of from the $^2F_{5/2}$ state to the $^2F_{7/2}$ state.[215]

On the other hand, $NaLnF_4$-based PLNPs like $NaYF_4$:Ln^{3+} or $NaGdF_4$:Ln^{3+} have also shown high X-ray absorption and afterglow luminescence, due to the presence of high-Z elements.[216,217] In addition, the presence of Na^+ and F^- in the crystal lattice induces the formation of vacancies and Frenkel defects, which facilitates the development of trapping sites for the trapping of excited electron–hole pairs.[218] The electron–hole pairs are subsequently captured by different activators for afterglow emission. For example, a multilayered $NaYF_4$ doped with different activator ions (Er^{3+}, Nd^{3+} and Ho^{3+}) exhibited emissions peaking at 1064 nm, 1180 nm and 1525 nm.[219] These peaks correspond to the $^4F_{3/2}$–$^4I_{11/2}$ transition of Nd^{3+}, $^5I_6$–$^5I_8$ transition of Ho^{3+} and $^4I_{13/2}$–$^4I_{15/2}$ transition of Er^{3+}, respectively. The afterglow by Er^{3+} at 1064 nm remained for over 72 hours following the cessation of X-ray irradiation.

Liu et al. discovered that $NaLuF_4$ has better X-ray absorption compared to $NaYF_4$ or $NaGdF_4$.[208] $NaLuF_4$ has an atomic number $Z_{max} = 71$ and X-ray absorption coefficient of $K_\alpha = 63.31$ keV, surpassing that of $NaYF_4$ ($Z_{max} = 39$, $K_\alpha = 17.05$ keV) or $NaGdF_4$ ($Z_{max} = 64$, $K_\alpha = 50.24$ keV). $NaLuF_4$:Tb^{3+} displayed strong afterglow emission peaks at 584 nm ($^5D_4$–$^7F_4$), 546 nm ($^5D_4$–$^7F_5$) and 489 nm ($^5D_4$–$^7F_6$) according to the optical transitions of Tb^{3+}.[208] Notably, the post-excitation afterglow intensity of $NaLuF_4$:15% Tb^{3+} nanocrystals is 3 times stronger than that of $NaYF_4$:15% Tb^{3+} nanocrystals. The afterglow duration of

2916 | *Chem. Soc. Rev.*, 2024, **53**, 2898–2931

This journal is © The Royal Society of Chemistry 2024

NaLuF$_4$:15% Tb^{3+} was reported to be 30 days, which is much longer than the 15 day afterglow duration of ZnGa$_2$O$_4$:Cr^{3+}, and many other commonly studied X-ray-activated PLNPs like SrAl$_2$O$_4$:Eu^{2+},Dy^{3+} and ZnS:Cu^{2+}/CO$_2$$^+$. Other than Tb^{3+} ions, other activators like Sm^{3+}, Pr^{3+} and Dy^{3+} could also accept energy from NaLuF$_4$ to emit persistent luminescence.[218] This is because the ^{3}P$_1$ level of Pr^{3+}, ^{4}F$_{9/2}$ level of Dy^{3+} and ^{4}G$_{5/2}$ level of Sm^{3+} are all located in close proximity to the traps in NaLuF$_4$.

4.1.4 Semiconductor-based nanomaterials. Semiconductors are also a viable class of nanomaterials for X-ray-excited luminescence, as X-rays usually possess enough energy to excite electron across the band gap. Nanosized silicon is an extensively studied semiconductor, exhibiting X-ray excitable luminescence. Nanosized porous silicon was first reported to be able to exhibit a broad luminescence in 2004, ranging from 500–800 nm, peaking at 720 nm.[220] Later on, it was discovered that Si nanocrystals exhibit emission maxima at approximately 430 nm and 620 nm, which were attributed to oxidized and non-oxidized silicon moieties, respectively.[221] However, since silicon itself does not possess high enough X-ray absorption due to its low atomic number, zinc and manganese were doped into mesoporous silica to further enhance its X-ray-excited luminescence.[222] The nanosystem displayed luminescence peaking at 570 nm following 50 kV X-ray excitation. Apart from silicon, boron nitride nanotubes and CdTe quantum dots could be excited by X-rays to emit luminescence at 379–450 nm and 700 nm, respectively.[223,224]

4.1.5 Organic nanomaterials. Traditional organic nanomaterials that exhibit X-ray excited luminescence are usually composed of aromatic hydrocarbon compounds featuring interconnected benzene rings. The mechanism for their X-ray excited luminescence is attributed to unbound valence electron transitions following X-ray irradiation, occupying π molecular orbitals.[225] Another mechanism would be the energy transfer from excited triplet states. For example, iridium complex-doped polymer dots exhibited X-ray-excited luminescence at 510 nm due to the efficient energy transfer from the triplet excited state of the polymers to the iridium complex.[226] More recently, Sun *et al.* reported X-ray-excited luminescence from di[4-(4-diphenyl-aminophenyl)phenyl]sulfone (DAPSF).[227] In the design of DAPSF molecules, the sulfone moiety was strategically chosen to serve as the electron-acceptor, while the di-phenylamino groups were designated as the electron-donor entity. Notably, the localization of the lowest unoccupied molecular orbital (LUMO) of DAPSF occurs at the sulfone site. Under X-ray irradiation, the sulphur group accepts the photons and relays it to the LUMO in the sufonyl group. The electronic transitions in the sufonyl group resulted in emissions of a sharp peak at 418 nm and two broader peaks at 490 nm and 510 nm.

4.2 Enhancing X-ray-excited luminescence

4.2.1 Enhancement of X-ray absorption. As mentioned before, elements that have a high atomic number and X-ray attenuation coefficients absorb X-rays more efficiently. By incorporating more of these elements, such as sulphur, Gd^{3+} or tungsten into the host crystal lattice, X-ray absorption and

X-ray induced luminescence could be enhanced.[228] For example, doping 12.3 mol% Gd^{3+} into CeF$_3$:Tb^{3+} caused a 2.5-fold enhancement in luminescence intensity peaking at 542 nm.[183] In addition, doping 1% of Pb^{2+} into CsMnCl$_3$ also caused a roughly 7-fold increase in X-ray-excited luminescence.[193] This is due to both the high absorption of Pb^{2+} and the effective energy transfer from Pb^{2+} to Mn^{2+} ions, achieving a quantum yield up to 21%. Tungsten(W)-doped ZnGa$_2$O$_4$:Cr not only exhibited a 1.3-fold increase in luminescence intensity at 696 nm, but also displayed a significant improvement in afterglow time.[106]

Other than doping elements directly into the host crystals, placing the element in close proximity to the crystal could also enhance luminescence intensity. For example, it was found that the molybdenum cluster compound (*n*-Bu$_4$N)$_2$[Mo$_6$I$_8$(OOC-1-adamantane)$_6$] embedded in a polystyrene (PS) matrix caused an increase in radioluminescence intensity.[229] This is because the polystyrene matrix can be excited by X-rays, transferring the energy efficiently to the cluster. In addition, Gali *et al.* grew ZnGa$_2$O$_4$:Cr^{3+} (ZGO) on top of SiC nanoparticles, which acted as an additional X-ray absorber to transfer the energy to the ZnGa$_2$O$_4$:Cr^{3+} for a 14-fold radioluminescence enhancement.[230]

4.2.2 Reduction of surface quenching. As mentioned before, nanoparticles are susceptible to surface quenching, which ultimately leads to a reduction in luminescence intensity. Traditional methods for reducing surface defects and increasing crystal domain size involve annealing the luminescent nanomaterial at high temperature, usually over 1000 °C.[231] Sintering agents were added in several studies to increase the crystal grain size at a lower temperature at around 600 °C. However, the presence of a sintering agent could lead to particle fusion and poor homogeneity in the nanoparticles. Therefore, Anker *et al.* proposed a method to encapsulate the sintering agent, NaF, inside the X-ray-excited luminescent nanomaterial, Gd$_2$O$_2$S:Eu^{3+}.[232] The presence of a protective shell (Gd$_2$O$_2$S:Eu^{3+}) around the sintering agents allowed the enhancement of the crystal domain size without aggregation problems. Following annealing at 600 °C, the core–shell structured nanomaterial exhibited a 30-fold increase in luminescence intensity when NaF was present at a concentration of 7.6 mol%. Despite being 150-fold smaller in diameter, the NaF@Gd$_2$O$_2$S:Eu^{3+} exhibited an intensity up to 40% of commercial microphosphors.

Despite the outstanding luminescence enhancement, the usage of high temperature treatments poses hazards and increases production costs. One method for reducing surface quenching in X-ray-excited luminescence from nanomaterials is to simply increase the particle size. For example, Nd^{3+} was doped into Zn$_2$Ga$_3$Ge$_{0.75}$O$_8$:Cr^{3+}, which resulted in an increase in the nanoparticle size from 45.4 nm to 86.2 nm and a subsequent 2-fold enhancement in luminescence intensity located at 696 nm.[214] Instead of increasing the particle size, gold nanoclusters (2.5 nm) was assembled and aggregated into aggregation-induced emission (AIE) clustoluminogens with the help of poly(allyl-amine hydrochloride) (PAH).[233] The clustoluminogens exhibited a size of 65.6 nm and a 5.2-fold enhancement in luminescence intensity at 570 nm.

This journal is © The Royal Society of Chemistry 2024

Chem. Soc. Rev., 2024, **53**, 2898–2931 | **2917**

Since increasing particle size might limit therapeutic applications due to the difficulties in penetrating biological barriers, designing core–shell structured nanophosphors with a passive shell coating would be a better strategy. It was realised that the $NaYF_4$ coating on $NaLuF_4:Tb^{3+}$ caused a 1.5-fold enhancement in luminescence intensity and a 6.5-fold increase in afterglow luminescence intensity.[208] In addition, $NaYF_4:Er^{3+}@NaYF_4$ with a 35 nm core and 7 nm shell led to a remarkable amplification of approximately 25-fold in luminescence intensity, compared with $NaYF_4:Er^{3+}$ alone (22 nm).[219] Developing core–shell structured nanophosphors could also enable the simultaneous doping of different activator ions other than Er^{3+} in different layers, separated by inert layers of $NaYF_4$. This prevents the cross-relaxation and concentration quenching when 2 or more activators are doped in the same crystal lattice.

4.2.3 Optimisation of the crystal phase and crystallinity. As mentioned previously in the NIR section, hexagonal $NaLnF_4$ exhibits better luminescence performance compared to the cubic counterpart. Similarly, it was also found that hexagonal $NaGdF_4:Eu^{3+}$ produced a 25% stronger X-ray-excited luminescence compared to the cubic $NaGdF_4:Eu^{3+}$.[184] Hexagonal $NaGdF_4$ favours the broadening of the valence band due to the distinct fluorine sites within the unit cell, which hinders the direct relaxation of self-trapped excitons. This allows the holes from the excitons to be trapped by Eu^{3+} ions, facilitating radiative f–f transition. In contrast, cubic $NaGdF_4$ presents challenges in radiative emission due to its eight-coordinated holes, which serve as electron traps. Consequently, the reduced migration of excitons to Eu^{3+} ions contributes to non-radiative relaxation and reduced luminescence intensity.

Apart from engineering hexagonal nanophosphors, enhancing the crystallinity of the host crystal can also improve the luminescence intensity. For example, Li^+ ions were doped into $Y_2O_3:Yb^{3+},Er^{3+}$ to enhance the crystallinity of the crystal lattice, which showed enhanced X-ray-activated luminescence.[178] Depositing nano-sized TiO_2 with $CH_3NH_3PbI_3$ also showed an 2-fold enhancement in luminescence intensity at 790 nm along with an increase in luminescence lifetime.[234] The ordered nanoporous architecture of TiO_2 nanotube arrays confines the three-dimensional $[PbI_6]^{4-}$ octahedral lattice, effectively curtailing ion migration and minimizing octahedral aggregation. This confinement mechanism significantly enhances the stability and crystallinity of the $CH_3NH_3PbI_3$ organometal halide perovskite, thus advancing its luminescence performance.

Recently, Han *et al.* reported that Li^+ and Yb^{3+} co-doping in $Zn_2SIO_4:Mn^{2+},Yb^{3+}$ could enhance luminescence by shifting the crystal to the favourable phase.[210] A coexistence of α phase (410) and β phases (023) is present in Zn_2SiO_4, where the nanocrystals exhibit the most optimal afterglow time and luminescence intensity with an α/β ratio of 2.76 (Fig. 19c). However, $Zn_2SiO_4:Mn^{2+}$ exhibited an α/β ratio of 0.42 (Fig. 19b). Introducing Yb^{3+} and Li^+ ions into the crystal caused a preferential substitution of higher-valence Zn^{2+} ions within the ZnO_6 octahedra of the β-phase structure, due to the higher valence of Yb^{3+} and Li^+. This substitution tendency takes place before Yb^{3+} ions replace the lower-valence Zn^{2+} ions within the
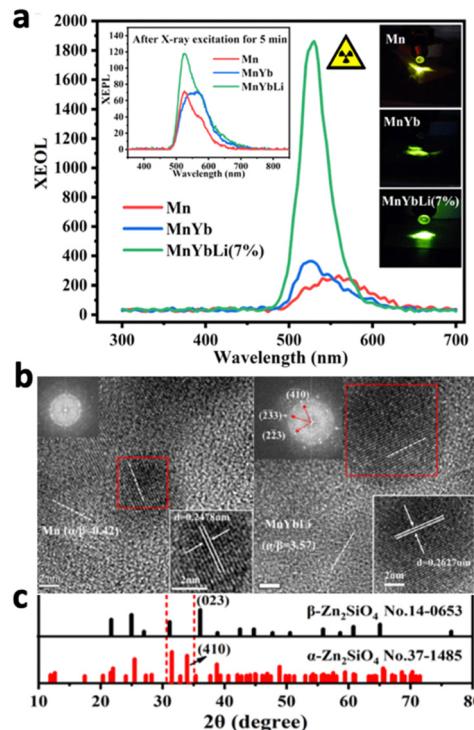
Fig. 19 (a) X-ray excited luminescence spectrum and afterglow spectrum (inlet) of Mn, MnYb, and MnYbLi (7%) samples after X-ray excitation for 5 min. (b) High resolution TEM images of $ZnSi_2O_4$:Mn (α/β = 0.42, left) and $ZnSi_2O_4$:Mn,Yb,Li (α/β = 3.57, right) samples. (c) XRD patterns of α-Zn_2SiO_4 and β-Zn_2SiO_4. Reproduced with permission from ref. 210. Copyright 2023, American Chemical Society.

ZnO_4 tetrahedra of the α-phase structure and accelerates the creation of the β crystal phase. As a result, $Zn_2SiO_4:Mn^{2+}$, Yb^{3+},Li^+ exhibited an α/β ratio of 3.57, accompanied by a 9-fold enhancement in X-ray excited luminescence intensity compared to $Zn_2SiO_4:Mn^{2+}$ (Fig. 19a and b). The band gap of $Zn_2SIO_4:Mn^{2+},Yb^{3+},Li^+$ was measured to be 4.51 eV, higher than the 4.02 eV band gap of $Zn_2SiO_4:Mn^{2+}$. This led to the formation of deeper traps and increased trap density, contributing to a stronger and longer afterglow luminescence.

4.3 X-ray-activated light-mediated therapy

To apply X-ray-excited luminescent nanomaterials to deep tissue therapy, merely inducing luminescence in nanomaterials is not enough. Since X-rays are highly ionising, it is important to reduce the dose of X-ray excitation while maintaining effectiveness for therapy. Therefore, several nanomaterials were proposed which only required a low X-ray dosage (as low as 0.09 Gy) for effective therapy. More importantly, the emergence of long afterglow luminescent nanomaterials could further reduce the exposure time to X-rays.

Many light-based therapy rely on the generation of ROS to kill the target cells. Therefore, methods have been developed to increase the oxygen content in tumour to enhance ROS generation, or even deplete molecules from the ROS defence system of the target cells, such as glutathione (GSH). In addition,

combined therapies have also been shown to boost overall therapeutic efficacy. Furthermore, X-ray-excited luminescence usually falls into the UV/visible spectrum, activating many of the light-sensitive molecules for photodynamic therapy or drug release. In this section, we will discuss the applications of X-ray-excited luminescence in photodynamic therapy, radiodynamic therapy, gas therapy and chemotherapy.

4.3.1 Photodynamic therapy. By combining X-ray-excitable luminescent nanomaterials with photosensitizers, photodynamic therapy can be achieved. Many X-ray-excitable luminescent nanomaterial emit visible light following activation, which activates photosensitizers like verteporfin (UV activation), Ag_3PO_4 (UV activation), PpIX (UV activation), merocyanine 540 (green light activation), Rose Bengal (green light activation), 2,3-naphthalocyanine (red light activation) and methylene blue (red light activation).[194,204,222,235–238] Inorganic photosensitizers are usually combined with X-ray-excited luminescent nanomaterials through electrostatic attractions, shell coating, co-loading in mesoporous silica, or conjugated to nanomaterial with the help of organic linkers or polymer.[179,204,222,235] Other than traditional photosensitisers, fluorescent proteins like eGFP, KillerOrange (KO), and KillerRed (KR) could also be activated by green light to produce ROS.[181] GFP, KO and KR formed a complex with $LaF_3:Tb^{3+}$ with His-tag as a linker, where X-ray irradiation caused $LaF_3:Tb^{3+}$ to emit green luminescence. The green luminescence then activated the 3 proteins to produce ROS. It was demonstrated that the $KR-LaF_3:Tb^{3+}$ complex showed radiation dose-dependent toxicity against *E. coli*.

The efficacy of the X-ray-activated photodynamic therapy depends heavily on the efficiency of the photosensitizer to generate ROS. Following excitation by the luminescent nano-materials, electron–hole pairs are generated in the photosensitizer. These holes exhibit a propensity to react with water molecules, resulting in the formation of hydroxyl radicals ($^{\bullet}OH$). However, a portion of the electron–hole pairs would recombine, resulting in the limited production of $^{\bullet}OH$ and reduced effectiveness of the therapy. Therefore, Bu *et al.* conjugated the cisplatin prodrug Pt(IV) with $LiLuF_4:Ce^{3+}$ and the photosensitizer Ag_3PO_4, where Pt(IV) acted as an electron acceptor.[237] This facilitated the separation of holes from electrons, thereby fostering an increased yield of $^{\bullet}OH$. Upon X-ray irradiation, $LiLuF_4:Ce^{3+}$ produced emissions at 305 and 325 nm due to the 5d to 4f transition of Ce^{3+}, which overlapped with the 295 nm excitation peak of Ag_3PO_4, causing the enhanced production of hydroxyl radicals. Furthermore, cisplatin is produced as Pt(IV) accepts electrons, directly attacking the DNA of the target cells.[239] The additional therapeutic effect from this nanosystem resulted in almost 100% HeLa cells eradication at 6 Gy while the control group without Pt(IV) only caused 90% cell eradication. More importantly, the cell killing effect of this nanosystem was retained under hypoxia conditions, where the other control groups without Pt(IV) exhibited a significant reduction in cell eradication.

Not only did this study improve the efficiency in ROS generation from photosensitizers, but it also suggested that combining chemotherapeutic drugs with PDT could enhance therapeutic efficacy in a hypoxic tumour microenvironment. Therefore, attempts have been made to co-deliver chemotherapeutic drugs, such as 5-FU, together with the scintillating nanoparticle to boost the therapeutic efficacy.[240] Li *et al.* co-loaded $CaF_2:Ce^{3+},Tb^{3+}$, Rose Bengal and sunitinib inside polyamidoamine (PAMAM) dendrimers, where sunitinib (SU) inhibits multiple receptor tyrosine kinases (RTK), suppressing angiogenesis in tumour.[192] *In vitro* studies on $4T_1$ cells confirmed an additional 20% tumour cell eradication in the presence of sunitinib, where the combined nanosystem achieved over 80% of cell eradication. Even at a lower radiation dose of 0.5 Gy, this approach yielded substantial tumour regression after 4 days of treatment.

In order to reduce side effects on other healthy tissues, efforts have been made to reduce the X-ray dosage and develop X-ray activated PLNPs that shorten X-ray irradiation time. Yang *et al.* produced tungsten(W)-doped $ZnGa_2O_4:Cr$ (ZGO:Cr/W) coupled with the photosensitizer ZnPcS4, enabling photodynamic therapy with a low dose of X-rays (0.18 Gy).[106] The presence of Cr^{3+} caused the generation of NIR luminescence peaking at 696 nm, which activated ZnPcS4 for the production of singlet oxygen. Following 2 minutes of X-ray irradiation, ZGO:Cr/W–ZnPcS4 exhibited increased singlet oxygen production, which persisted for 40 minutes more after the switching off of X-ray excitation due to the afterglow effect. *In vitro* PDT effects on cells demonstrated only 25% cell viability after 3 2-minute 0.09 Gy X-ray irradiation cycles.

Despite the effectiveness of the treatment, there is no imaging modality to guide the PDT process, since most of the NIR luminescence is quenched by the photosensitizer. This caused the development of $Zn_3Ga_2Ge_2O_{10}:Cr^{3+},Mn^{2+}$ (ZGGCM), which could emit NIR (698 nm) and green (532 nm) afterglow from Cr^{3+} and Mn^{2+} ions, respectively.[213] The green luminescence is used to activate Rose Bengal, while the NIR luminescence is used as an imaging modality to monitor the therapy. Intravenous administration of a pre-X-ray-excited ZGGCM solution to normal mice resulted in strong afterglow signals in the liver and lungs that lasted for at least 9 minutes. Apart from imaging with NIR luminescence, Gd^{3+}-containing nanomaterials could also be imaged through computed tomography (CT) or magnetic resonance imaging (MRI) due to the strong X-ray absorption and long relaxation time of Gd^{3+}.[183]

It has been recently reported that $NaLuF_4:Tb^{3+}$ conjugated with Rose Bengal (RB) and the ligand targeting amyloid-β (ScNPs@RB/Ab) could carry out PDT against Alzheimer's disease.[14] Following intravenous injection of the nanosystem *in vivo*, the targeting amyloid-β caused a 6.6-fold enhancement in blood–brain barrier penetration efficiency compared to ScNPs@RB. 0.12 Gy X-rays successfully penetrated the scalp and excited ScNPs@RB/Ab in the brain, outperforming other excitation sources like NIR and green light (Fig. 20a and b). $NaLuF_4:Tb^{3+}$ emitted green luminescence, which excited RB to produce singlet oxygen ($^1O_2$) for oxygenation and suppression amyloid-β self-assembly (Fig. 20c). As a result, neurotoxic aggregated amyloid-β plaques could not be formed. After 18 days of treatment, spatial memory and learning of the mice

This journal is © The Royal Society of Chemistry 2024

Chem. Soc. Rev., 2024, **53**, 2898–2931 | **2919**

were evaluated using the Morris water maze test. The group injected with ScNPs@RB/Ab and subjected to X-ray irradiation displayed improved cognitive function, with shorter escape latencies, increased time in the target quadrant, and more platform crossings (Fig. 20d–f). Moreover, Aβ plaque load in the cortex and hippocampus was significantly reduced, accompanied by a substantial decrease in soluble and insoluble Aβ42 levels (Fig. 20g–j). On the other hand, both ScNPs@RB/Ab and X-rays alone showed limited effects on cognitive function and Aβ deposition.

4.3.2 Radiodynamic therapy. Certain luminescent nanomaterials could produce singlet oxygen without coupling an external photosensitizer, such as copper nanoparticles, Y_2O_3:Eu^{3+}, and $BaGdF_5$:Tb^{3+}/Eu^{3+}/Sm^{3+}.[185,200,241] Taking $NaCeF_4$:Gd^{3+},Tb^{3+} as an example, the mechanism of ROS generation is as follows:[186] Under X-ray irradiation, Ce^{3+} ions are excited to the 5d orbital, transferring their energy to populate the $^5D_4$ and $^5D_3$ states of Tb^{3+} ions for green emissions. However, instead of transferring energy to Tb^{3+} ions, Ce^{3+} ions can further absorb the energy of another secondary electron generated from X-ray irradiation, leading to excitation towards the conduction band. The electrons in the conduction band will further react with O_2 to form $\bullet O_2^-$.

Since these nanosystems could produce ROS without the quenching of their luminescence, their luminescence could be used for other purposes. For example, their luminescence could be used to activate a photosensitizer for additional generation of ROS. Au NPs were able to generate hydroxyl radicals under X-ray excitation while producing luminescence at 570 nm, to excite the conjugated Rose Bengal.[233] The combined effect from both PDT and RT showed a better therapeutic effect than any of the treatments alone. Other than generating additional ROS, the luminescence generated could also be applied for imaging purposes in NIR-I and NIR-II regions.[201,242] Yang *et al.* produced NIR-II-emitting Nd^{3+}-doped black phosphorus quantum dots that produced ROS following X-ray irradiation.[242] Nd^{3+} ions, having high X-ray attenuation, absorbed X-ray and relayed the energy to BP QDs to generate ROS (Fig. 21a). Concurrently, part of the excited Nd^{3+} relaxed and emitted NIR-II luminescence peaking at 1050 nm (Fig. 21b). *In vivo* studies revealed the
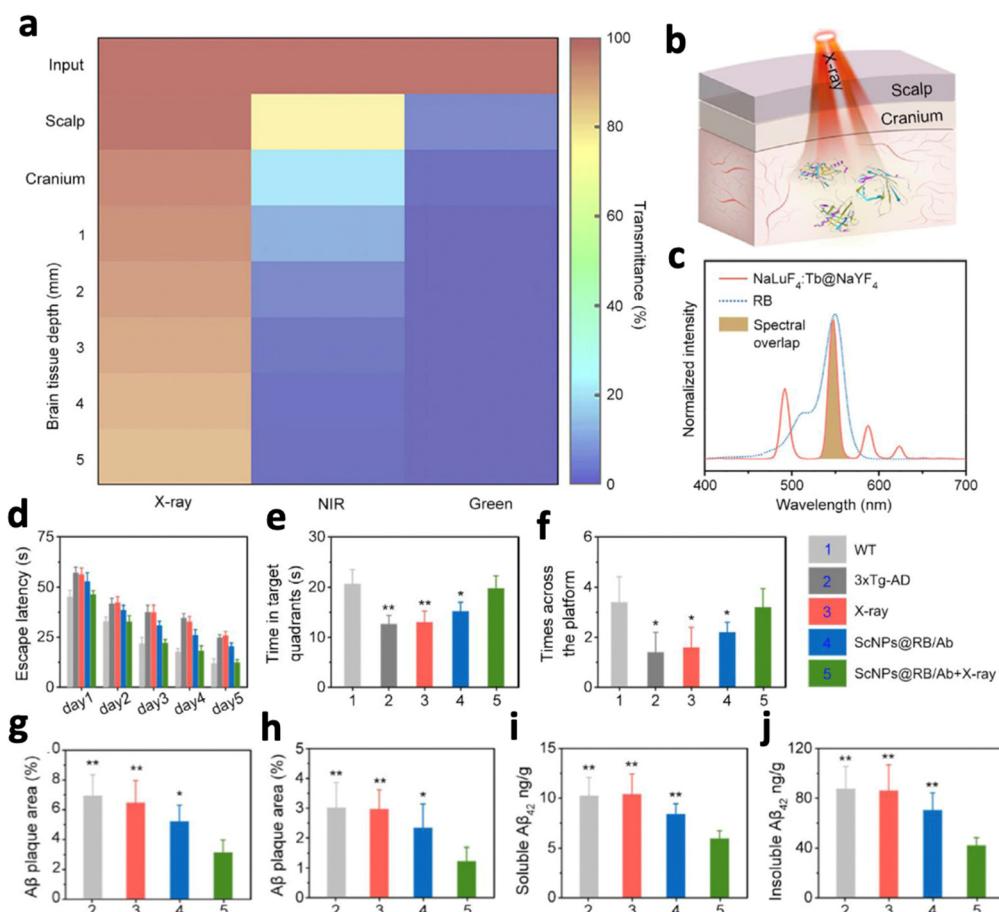
Fig. 20 (a) Transmittance of X-ray NIR and green light through the scalp, cranium and different thicknesses of brain tissue. (b) Schematic illustration for the X-ray activated photodynamic therapy for Alzheimer's disease by inhibiting Aβ aggregation in the brain. (c) Spectral overlap between X-ray activated luminescence from $NaLuF_4$:Tb^{3+} and the absorption spectrum of Rose Bengal. *In vivo* comparison of (d) escape latency, (e) time in target quadrants and (f) times across the platform of Alzheimer's disease mice model in the Morris water maze test. Quantification of Aβ plaques in the (g) cortex and (h) hippocampus, as well as (i) soluble and (j) insoluble Aβ42 levels in the brain after different treatments. Reproduced with permission from ref. 14. Copyright 2023, Elsevier.

2920 | *Chem. Soc. Rev.*, 2024, **53**, 2898–2931

This journal is © The Royal Society of Chemistry 2024
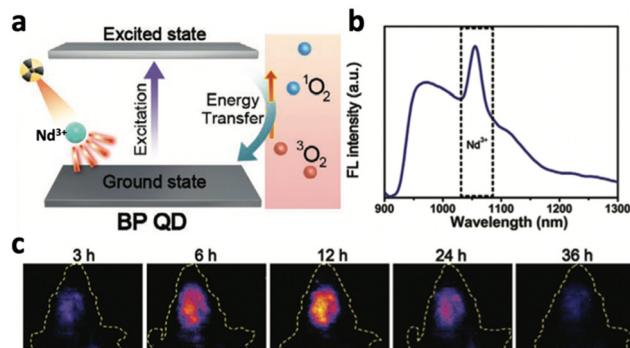
Fig. 21 (a) Schematic illustration of energy transfer from Nd^{3+} ions to BP QDs for ROS generation following X-ray irradiation. (b) NIR-II emission spectrum of Nd^{3+}-doped BP QDs. (c) Real-time NIR-II luminescence imaging of mice intravenously injected with Nd^{3+}-doped BP QDs. Reproduced with permission from ref. 242. Copyright 2022, Wiley-VCH Verlag GmbH & Co. KGaA, Weinheim.

strong NIR-II FL signals precisely located in the brain glioblastoma (GBM) site, peaking at 12 hours post-injection (Fig. 21c). This resulted in a reduction of HIF-1α and CD31 expression in the GBM region, accompanied by the suppression of intracranial GBM growth.

Radiodynamic therapy or photodynamic therapy rely on ROS generation and are often limited by the hypoxic tumour microenvironment. Without the use of ROS, $LuPO_4:Pr^{3+}$ produced UV light following X-ray irradiation to kill tumour cells through oxygen-independent processes.[187] $LuPO_4:Pr^{3+}$ converted X-rays into UVC radiation through a unique $4f^15d^1$-$4f$ transition in Pr^{3+}, resulting in a localized emission within the 220–285 nm range. UVC radiation induces a significant DNA damage primarily affecting cyclobutane pyrimidine dimers (CPDs) and 6–4 photoproducts (6-4PPs), leading to cell cycle arrest and inactivation. Due to the strong absorption of UVC photons within a few micrometers, neighboring cells near the scintillating particles are impacted while the normal surrounding tissue is spared. Remarkably, at a concentration of 2.5 mg mL^{-1} $LuPO_4:Pr^{3+}$, almost 90% of fibroblast (HFF1) cells were eradicated under 2 Gy X-ray irradiation.

4.3.3 Gas therapy. Gas therapy utilizes nearly non-toxic gasotransmitters, such as nitric oxide (NO), carbon monoxide (CO), or hydrogen (H_2) to cause apoptosis in tumour cells. Other than generating ROS, certain gaseous molecules could also infiltrate different physiological processes to cause apoptosis in tumour cells or activate immune cells.[243] For example, NO induces oxidative and nitrosative stress, mitochondrial and DNA impairment, inhibition of DNA synthesis and repair and intensified inflammatory responses.[244] Notably, X-rays carry enough energy to break bonds like S–N, which could generate NO at high concentration from compounds like *s*-nitrosothiol (SNO), showing killing effects on cancer cells.[245] However, utilising X-rays to break bonds usually requires a high X-ray dosage (> 5 Gy) administered continuously during the treatment process, which may result in unwanted side effects on healthy tissues. By leveraging the strong intensity and long afterglow of X-ray-excited PLNPs, a lower-dose X-ray-based gas therapy can be achieved. Hao *et al.* reported $ZnGa_2O_4:Mn^{2+}$

(ZGO:Mn) PLNPs conjugated with a photoresponsive NO donor, Roussin's black salt (RBS), achieving gas therapy at a low X-ray dosage (~0.9 mGy).[212] ZGO:Mn produced green persistent luminescence, activating RBS to generate sustained NO even after X-ray irradiation was turned off for 40 minutes. In addition, deep-tissue NO release reached 1.2 μM even when X-rays were shielded with 24 mm pork slices. Incubation with $4T_1$ cells resulted in a significant reduction in cell viability to 37%, much lower than that of the group incubated with ZGO:Mn only (86% cell viability).

Apart from utilising NO, Yang *et al.* designed Au-TiO_2 coated with PLNP ZnS:Cu,Co-A (Au-TiO$_2$@ZnS:Cu,Co-A) for the generation of H_2 in tumour cells, which exhibited anti-cancer and anti-inflammatory properties.[209] Under X-ray irradiation, electrons at the Au–TiO$_2$ NR heterojunction were transferred to Au NRs to undergo a reduction reaction with water to produce H_2. Following the cessation of X-ray irradiation, ZnS:Cu,Co-A produced afterglow luminescence at 578 nm. This enabled Au NRs to inject hot electrons into the conduction band of TiO_2 to catalyze H_2 generation, which is observed even 10 minutes after cessation of X-ray irradiation. Concurrently, the holes generated are captured by sacrificial agents or OH$^-$ ions, yielding reactive oxygen species. Au–TiO$_2$@ZnS showed concentration- and time-dependent cytotoxicity on MC38 cancer cells *in vitro*, as well as a 90.9% tumour supression rate *in vivo*.

Instead of solely relying on ROS generation, Hao *et al.* developed a CO-based gas therapy that could also activate anti-tumour immunity.[13] They combined $NaLuF_4:Gd^{3+},Tb^{3+}@$-$NaLuF_4$ with PhotoCORM (ScNPs-PhotoCORM), where green emission from Tb^{3+} activated PhotoCORM to generate CO and ROS up to 8 cm deep in biological tissue following X-ray irradiation. Simultaneously, CO reversed the deep tissue immunosuppressive TME and activated adaptive anti-tumour immunity (Fig. 22a). Tumour-bearing mice treated with ScNPs-PhotoCORM exhibited elevated levels of pro-inflammatory IL-6 and TNF-α, while exhibiting lower levels of anti-inflammatory cytokine IL-10 (Fig. 22b–d). Furthermore, the mice exhibited enhanced levels of interferon-γ (IFN-γ) and CD8, confirming the activation of *in vivo* adaptive anti-tumour immunity (Fig. 22e and f). Both the primary and distant tumours exhibited significant suppression in tumour growths, confirming the successful activation of deep tissue anti-tumour immunity response and TME reversal (Fig. 22g and h). To further enhance the efficacy of CO-based gas therapy, $LiLuF_4:Ce^{3+}$ and UV-photosensitive $Mn_2(CO)_{10}$ were combined.[246] UV emission from LiLuF4:Ce^{3+} following X-ray irradiation resulted in CO and MnO_2 release from $Mn_2(CO)_{10}$. MnO_2 generated hydroxyl radicals through Fenton-like activity, while depleting glutathione (GSH) to impair the cellular antioxidant defence system. *In vivo* studies with the nanosystem showed superior tumour growth control through DNA damage and inhibiting glycolysis.

4.3.4 Drug delivery. Due to the high energy of X-rays, most X-ray-excited nanomaterials produce luminescence in the UV/visible range, which is not favourable for *in vivo* monitoring of drug release.[228] Instead, the UV/visible emissions are advantageous in triggering drug release by cleaving photocleavable

This journal is © The Royal Society of Chemistry 2024

Chem. Soc. Rev., 2024, **53**, 2898–2931 | **2921**
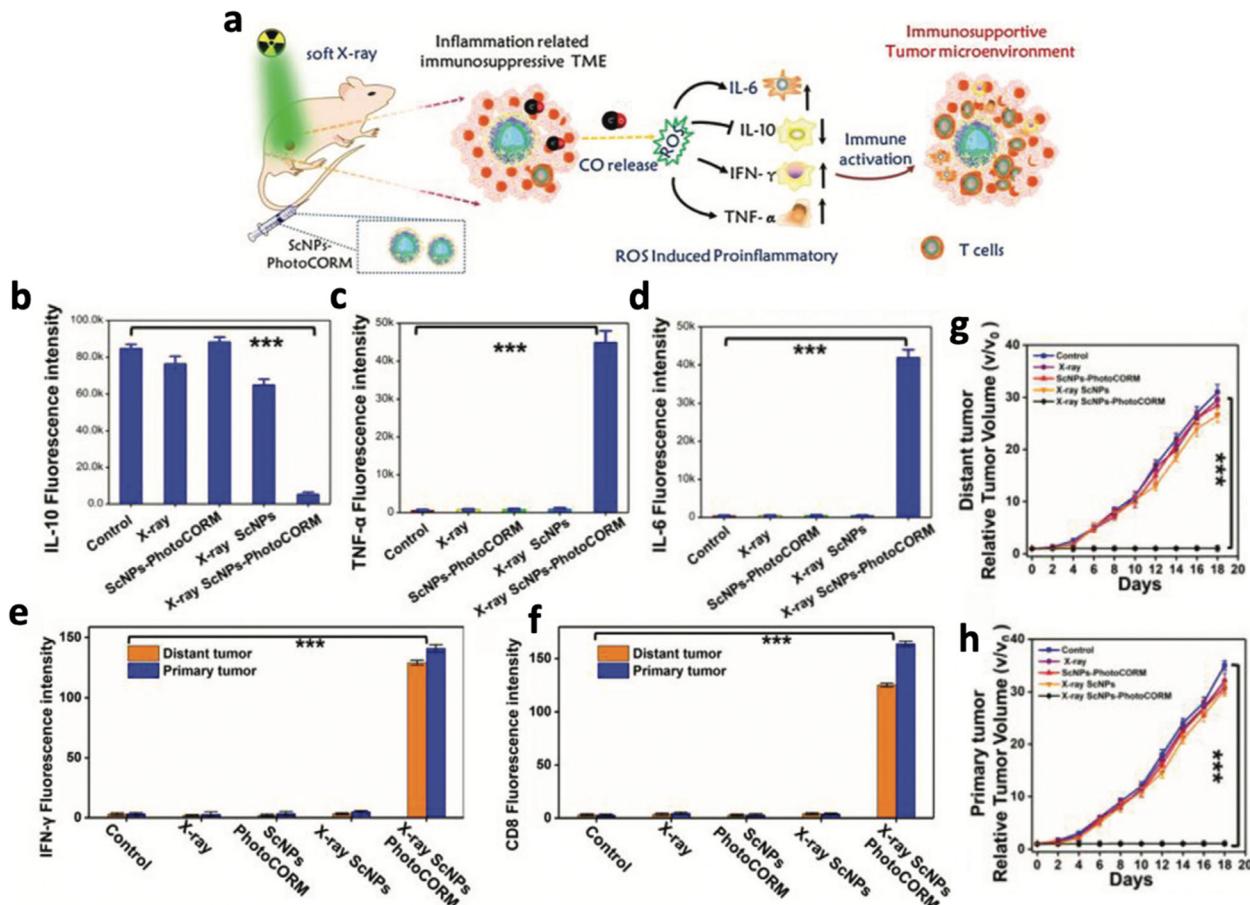
Fig. 22 (a) Schematic illustration of CO-based gas therapy which involves ROS generation and immune activation to a pro-inflammatory state. (b) Comparison of in vivo mice tumour slices of different treatment groups stained with (b) IL-10, (c) TNF-α, (d) IL-6, (e) IFN-γ and (f) CD8. Comparison of (g) primary and (h) distant tumour growth in $4T_1$ tumour-bearing mice with different treatments. Reproduced with permission from ref. 13. Copyright 2021, Wiley-VCH Verlag GmbH & Co. KGaA, Weinheim.

linkers. For example, $LiYF_4$:Ce^{3+} was conjugated with methotrexate (MTX) through photocleavable Fmoc-2-nitrophenylalanine (NPA).[188] Under X-ray irradiation, Ce^{3+} emitted UV luminescence at 305 nm and 325 nm, cleaving NPA to release methotrexate (MTX). A maximum of 84% MTX release was achieved following 6–8 Gy X-ray irradiation. Notably, in vitro studies with the AsPC-1 pancreatic cell line demonstrated that traditional chemotherapy with free MTX alone was ineffective, while conventional X-ray radiotherapy showed inhibition of cell growth with 50% inhibition (IC50) at a radiation dose of 4 Gy. On the other hand, the new nanosystem with a 10 nM MTX concentration and 30 ppm of nanoparticles achieved a superior IC50 value of 0.5 Gy. In vivo studies with pancreatic tumour-bearing mice also showed that the group treated with NP-MTX and X-ray radiation showed the most significant reduction in tumour growth after 14 days. In addition to merely triggering drug release, the UV light produced could also sensitise tumour cells simultaneously, resulting in an enhanced therapeutic effect.[247]

4.4 Strengths and weaknesses of X-ray-activated light-mediated therapy

X-ray activated luminescence deep-tissue therapy holds both promising strengths and weaknesses as a therapeutic approach. One of its primary strengths lies in its ability to penetrate deep tissues in the body, which enables the treatment in deep tissue which is challenging to access using UV, NIR or visible light. For instance, X-rays can penetrate bones, enabling light-based therapeutics in the brain through the cranium. Additionally, the use of high-energy X-ray excitation allows direct band-to-band excitation of nanomaterials, which causes highly efficient generation of UV or visible light. The vast production of UV/visible light enabled the activation of light-sensitive molecules, such as photosensitisers, photocleavable linkers which operate mostly in the UV/visible range. In addition, the highly efficient UV production could also cause direct cell damage to the target cells while minimizing healthy cell damage due to the low penetration of UV light. Compared to NIR-induced upconversion luminescence which requires the energy accumulation of several photons, X-ray-excited UV/visible emissions are much more efficient. The high luminescence efficiency also results in brighter luminescence and longer afterglow in various nanosystems.

However, there are weaknesses that accompany the application of X-ray-excited luminescence in deep tissue therapy. One significant concern is the potential for radiation-induced

2922 | Chem. Soc. Rev., 2024, 53, 2898–2931

This journal is © The Royal Society of Chemistry 2024

damage to healthy tissue. The radioactive nature of X-rays inadvertently damages the DNA of healthy cells which could cause adverse side effects and complications. In addition, since X-rays favour the generation of UV/visible light, NIR emissions from X-ray-excited nanomaterials are rarely seen, which limits their potential applications to photothermal therapy, or NIR-II deep tissue imaging and monitoring. Furthermore, X-ray-generating equipment are scarce and often costly, which limits the accessibility and availability of X-ray activated luminescence therapy.

5. Ultrasound-excited luminescence

Ultrasound, possessing deep tissue penetration and being relatively safe, has been used extensively as an imaging modality since the 1960s. Out of all the excitation methods listed before, nanomaterials that exhibit ultrasound-excited luminescence are rarer and much less studied. However, ultrasound-activated light therapy remains as one of the most promising therapeutic modality.

In this section, we will discuss 2 ways by which ultrasound can generate light through nanomaterial-mediated processes – nanomaterial-mediated sonoluminescence and ultrasound-excited mechano-luminescence, as well as their application in deep tissue therapy.

5.1 Nanomaterial-mediated sonoluminescence

Sonoluminescence, the emission of light following acoustic cavitation of microbubbles, was discovered over 2 decades ago.[11] Following ultrasound irradiation, acoustic cavitation occurs in the liquid medium, causing the generation of microbubbles that undergo rapid compression and expansion, and finally collapse (Fig. 23a). The collapse of microbubbles usually results in a temperature change in the gas over thousands of degrees in a very short time resulting in gas ionization and light emission, usually in the UV range.[248] Certain nanomaterials can also accept energy from sonoluminescence to emit at a different wavelength (Fig. 23a).

However, sonoluminescence is weak and lacks tunability in emission wavelength. Therefore, nanomaterials were used in several studies to improve the intensity and modify the emission wavelength of sonoluminescence, fostering their application in deep tissue therapy. For example, carbon nanodots were shown

Fig. 23 Schematic illustration of the mechanism of (a) nanomaterial-mediated sonoluminescence and (b) ultrasound-excited mechano-luminescence.

to alter the original blue sonoluminescence into orange.[249] The original blue sonoluminescence results from the interaction between hydroxyl free radicals (•OH) in water and the collapsing bubbles. Following the addition of carbon nanodots, they captured •OH and formed C- and O-based functional groups like –COOH bonds and CO molecules. This interaction suppressed •OH radicals and resulted in a weaker UV/blue emission. On the other hand, –COOH or C-based molecules like CO were excited by the collapse of bubbles and emitted at 610 nm following radiative recombination. Nanomaterials can also enhance the intensity of sonoluminescence. A nanoconjugate composed of protoporphyrin IX and gold nanoparticles (Au–PpIX) was able to enhance sonoluminescence at 350–650 nm by over 4 times.[250] This is because gold nanoparticles functioned as cavitation nuclei, increasing the microbubble formation. In addition, PpIX was activated by ultrasound to generate free radicals which resulted in greater sonoluminescence. Similarly, biochar-supported ZnO (ZnO-BC) nanorods also enhanced sonoluminescence by reducing the energy threshold required for bubble generation, increasing the number of nucleation sites and microbubbles that led to stronger sonoluminescence.[251]

One of the most prominent applications of nanomaterial-mediated sonoluminescence is sonodynamic therapy, where the generation of sonoluminescence causes the excitation of photosensitisers and generation of reactive oxygen species (ROS). Grebinyk et al. reported that the combination of ultrasound irradiation and 20 μM C_{60} fullerene reduced the viability of HeLa cells.[252] C_{60} fullerene exhibited a broad-band absorption from 320 to 580 nm, which overlapped with the UV-peaked broad emission spectrum of sonoluminescence. 60 s of 1 MHz ultrasound irradiation caused ROS generation and reduction in cell viability of HeLa cells to 59%, while ultrasound or C_{60} alone had negligible effects on cell viability. To reduce the distance between the site of sonoluminescence and photosensitizers, Wang et al. synthesised microbubbles with Rose Bengal as the wall (RB-MB), where the ultrasound-induced collapse of microbubbles generated sonoluminescence to directly excite Rose Bengal.[253] Under 1 MHz ultrasound irradiation, the RB-MBs exhibited enhanced ROS production compared to other control groups. In addition, RB-MBs exhibited 76.5% tumour inhibition in the HT-29 tumour mice model as a result of a more efficient energy transfer, whereas the combination of Rose Bengal NPs and ultrasound alone exhibited 49.2% tumour inhibition. Sonodynamic therapy can also be enhanced through increasing the efficiency of ROS generation of photosensitizers. Au_{144} clusters were deposited on TiO_2, acting as an electron acceptor that prevented the rapid electron–hole recombination of TiO_2.[254] Hence, •OH production was enhanced by 2 fold. The efficient electron-trapping was enabled due to the slightly lower energy level of the LUMO in Au_{144} compared to the excited state of TiO_2.

To reduce ultrasound irradiation time and enable low-background imaging/monitoring, sonodynamic therapy can also be coupled with ultrasound-induced afterglow. Recently, Pu's group developed an organic nanosystem (NCBS/DPAs SNAP) that was able to produce singlet oxygen and ultrasound-induced
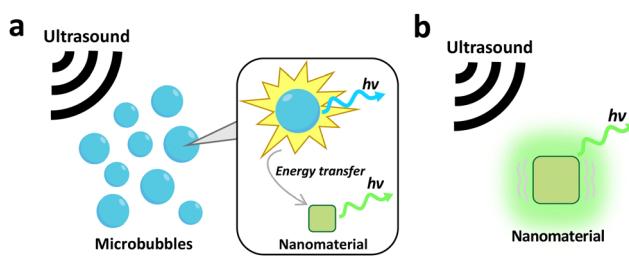
This journal is © The Royal Society of Chemistry 2024

Chem. Soc. Rev., 2024, **53**, 2898–2931 | **2923**

afterglow through dioxetane-mediated emission.[255] Under ultrasound irradiation, sonoluminescence activated the photosensitizer silicon 2,3-naphthalocyanine bis(trihexylsilyloxide) (NCBS) to produce singlet oxygen, which converted the sonoafterglow substrate dicyanomethylene-4*H*-benzothiopyran-phenoxyl-adamantylidene (DPAs) into active dioxetane substrates. NCBS absorbed the energy from dioxetane and emitted afterglow luminescence at 780 nm (Fig. 24a). Following 5 minutes of 1 MHz ultrasound irradiation, the nanosystem induced 90% cell death in $4T_1$ cancer cells. To enhance the therapeutic specificity of the nanosystem, DPAs were silenced with $ONOO^-$ responsive moieties (Pro-DPAs). This nanosystem was inactive in healthy tissues populated with M0 and M2 macrophages, while exhibiting a 3.5 fold increase in ROS generation and luminescence in a M1 macrophage-populated tumour microenvironment due to the overproduction of $ONOO^-$. An SBR of around 90 was also observed in a living mouse under 1.8 cm tissue depth, which is 4.0 and 47.4 times higher than that for photoafterglow and fluorescence, respectively. This nanosystem serves as an excellent candidate for tumour-specific sonodynamic therapy with deep tissue imaging capabilities.

5.2 Ultrasound-excited mechanoluminescence

Although nanomaterials can enhance sonoluminescence or alter its emission wavelength, there are still insufficient strategies to control sonoluminescence, as its occurrence and intensity depends on many different parameters of the liquid medium.[257]

On the other hand, ultrasound-activated mechanoluminescence depends mainly on the characteristics of the nanoparticle, which could be more easily controlled. Mechanoluminescence generally refers to the emission of light under external mechanical stress or deformation of the crystal.[12] In the nanomaterial world, it was realised that ultrasound could induce mechanical stress or deformation in nanomaterials, enabling mechanoluminescence through different mechanisms (Fig. 23b). For example, ultrasound could release electrons trapped inside $Sr_2MgSi_2O_7$: Eu^{2+},Dy^{3+} (SMSO), resulting in emission at 470 nm. When SMSO is exposed to 10 seconds of 365 nm UV irradiation, an electron from Eu^{2+} is excited to the conduction band, which is then trapped by $V_O^{\bullet\bullet}$ and $Dy_{Sr}^{\bullet}$ defects.[258] Upon 1.5 MHz ultrasound irradiation, the trapped electron is released back to the ground state of Eu^{2+}, causing luminescence peaking at 470 nm due to the $4f^65d^1$ to $4f^7$ transition of Eu^{2+}. By incorporating it with caesium lead halide quantum dots inside a polydimethylsiloxane (PDMS) pixel array, the emission wavelength can even be tuned to 515 nm (green) or 640 nm (red).

Ultrasound irradiation (1 MHz) can also induce mechanoluminescence in $SrAl_2O_4:Eu^{2+}$ (SAOE) at 525 nm without the need for UV pre-irradiation. When combined with persistent luminescent $ZnGa_2O_4:Cr^{3+}$ (ZGC) inside mesoporous silica nanoparticles (mSZ), the mechanoluminescence at 525 nm from SAOE excited ZGC, emitting afterglow at 715 nm (Fig. 24b and d).[256] The nanosystem was loaded with the drug clarithromycin (CLR) and coated with quenching polydopamine layers (ePDA).

Fig. 24 (a) Schematic illustration of the mechanism of nanomaterial-mediated sonoluminescence afterglow through generation of singlet oxygen and dioxetane intermediates. (b) Schematic illustration of the mechanism of ultrasound-excited mechanoluminescence through energy transfer between SAOE and ZGC, emitting red afterglow luminescence. (c) Schematic illustration of PLC-triggered drug release and ultrasound-activated NIR afterglow for *H. pylori* treatment and imaging. (d) Excitation and emission spectra of ZGC and the emission spectrum of SAOE. (e) Percentage release of CLR from the ePDA-coated or non-coated nanosystem alone or incubated with *H. pylori*. (f) Survival rate of *H. pylori* following treatment with different groups at different CLR concentration. Reproduced with permission from ref. 256. Copyright 2022, American Chemical Society.

2924 | *Chem. Soc. Rev.*, 2024, **53**, 2898–2931

This journal is © The Royal Society of Chemistry 2024

The presence of phospholipase C from *H. pylori* degraded the ePDA layers and released CLR while restoring the NIR luminescence (Fig. 24c). 82.4% of CLR was released following 25 hours of incubation with *H. pylori*, whereas only 15.8% of CLR release was observed in PBS (Fig. 24e). In addition, afterglow was only detected in *H. pylori* mice, and the intensity increased with increasing *H. pylori* concentrations. Incubating this nanosystem with *H. pylori* reduced cell viability to 15.3% at 6.4 μg mL^{-1} (Fig. 24f). The identical nanosystem was also applied for a photothermal/NO-based combined therapy.[259] The NIR afterglow produced under ultrasound irradiation activated PDA layers to liberate NO and induces a photothermal effect. The liberation of NO and the temperature gradient on the NPs caused them to self-propel, enhancing endocytosis into tumour cells by 2 fold. The NPs also exhibited sustained NO release for 2 hours, accompanied by an 11 °C temperature increase which persisted for 30 minutes after the cessation of ultrasound activation. This combined therapy completely halted the tumour growth after 27 days of treatment, while exhibiting the highest apoptosis rate (95.2%) and the lowest proliferation rate (8.3%) compared to other treatments.

5.3 Strengths and weaknesses of ultrasound-activated luminescence-based therapy

The utilization of ultrasound-activated phototherapy for the treatment of deep tissues presents both noteworthy advantages and limitations. Among its advantages, ultrasound possesses a superior tissue penetration depth compared to traditional UV/vis light and near-infrared (NIR) light, rendering it suitable for deep tissue applications. Importantly, ultrasound is regarded as a safer modality than X-rays as it does not involve ionizing radiation, reducing the risk of harming healthy cells. Additionally, the equipment required for ultrasound generation is simpler and more cost-effective compared to X-ray generating equipment.

However, it is important to note that ultrasound does not possess enough penetration depth compared to X-rays, especially through bone, where it experiences severe scattering. This limits the application of ultrasound-activated light therapy in areas shielded by bone, such as the brain. Despite being the most studied form of ultrasound-activated luminescence, sonoluminescence is still an unpredictable and random process. The difficulty in controlling the intensity, location and occurrence of such process makes it challenging for application in therapeutic purposes. Although ultrasound-excited mechanoluminescent nanoparticles can solve such problems, currently there are limited reports on nanomaterials that produce strong and consistent luminescence under ultrasound activation. This greatly impedes the application of such a mechanism in deep tissue therapy. Finally, although ultrasound does not cause radiation damage, it might induce unwanted cavitation in other healthy cells, which can cause unwanted tissue heating.

To widely apply ultrasound-excited luminescence in deep tissue therapy in the future, it is essential to produce low-dose ultrasound-activatable luminescent nanomaterials that rely on a controllable mechanism to produce luminescence.

6. Conclusions and outlook

Deep tissue light-mediated therapy is promising due to the precise control of therapy and its effectiveness. Much work has been performed to overcome the bottleneck of traditional light-based therapy which involves using low-penetrating UV or visible light to activate therapy. Studies on chemiluminescence-, NIR-, X-ray- and ultrasound-activated light therapy have proved sufficient specificity and therapeutic efficacy, despite having individual advantages and drawbacks. Chemiluminescence allows autofluorescence-free luminescence generation, but it lacks external control over luminescence and therapy activation. NIR enables tuneable excitation and emission wavelength that could be applied for different theragnostic purposes, *i.e.*, orthogonal excitation/emission, but its penetration depth is limited. X-rays possess the deepest tissue penetration depth and generate strong luminescence, but they cause radiation damage to surrounding healthy cells. Ultrasound possesses sufficient tissue penetration combined with limited side effects on healthy tissue, but the mode of luminescence generation is not very well controlled and limited reports on ultrasound-activatable nanoparticles are available.

Other than carrying out the therapy alone, image-guided therapy has been studied more recently. This is because it provides a modality to monitor the therapy which results in greater precision and efficiency, with the help of CT, MRI, or luminescence in the NIR-IIb/NIR-IIc spectrum. Efforts have also been made to develop ''activatable'' nanosystems that only become activated at target sites, exhibiting strong specificity when combined with external light triggering.

However, challenges still exist in deep tissue therapy with the mentioned 4 excitation modes. First of all, external irradiation using NIR, X-rays or ultrasound frequently results in unwanted irradiation on the healthy tissue, which may lead to unwanted side effects. NIR causes tissue heating and X-ray causes radiation damage while ultrasound causes unwanted cavitation that also leads to tissue heating. Therefore, since it is hard to eliminate such side effects, it is important to engineer nanosystems that can be activated by low dose of NIR, X-ray and ultrasound. Second, certain activation modes still do not yield luminescence with high intensity or efficacy, which includes chemiluminescence, sonoluminescence or certain NIR-activated luminescence. Efforts would be required to develop more controllable, efficient and brighter nanosystems following such activation. Finally, there has also been an emergence of combined therapy, such as the combination of chemotherapy and photodynamic therapy, resulting in a better therapeutic effect. In these systems, it is important to ensure that both therapies are activated by light, or activated by the specific local environment of the target cells to ensure specificity of the treatment.

Author contributions

Chung Yin Tsang: conceptualisation, writing – original draft, and writing – review and editing; Yong Zhang: conceptualisation, writing – review and editing, and supervision.

Conflicts of interest

There are no conflicts to declare.

Acknowledgements

Notes and references

1 T. J. Dougherty, C. J. Gomer, B. W. Henderson, G. Jori, D. Kessel, M. Korbelik, J. Moan and Q. Peng, *J. Natl. Cancer Inst.*, 1998, **90**, 889–905.

2 B. Simmons, R. Griffith, L. Falto-Aizpurua and K. Nouri, *J. Eur. Acad. Dermatol. Venereol.*, 2015, **29**, 1275–1279.

3 N. Fomina, J. Sankaranarayanan and A. Almutairi, *Adv. Drug Delivery Rev.*, 2012, **64**, 1005–1020.

4 B. C. Wilson and G. Adam, *Med. Phys.*, 1983, **10**, 824–830.

5 D. J. Burgess, *Nat. Rev. Cancer*, 2012, **12**, 737.

6 Y. Liu, Y. Liang, P. Lei, Z. Zhang and Y. Chen, *Adv. Sci.*, 2023, **10**, e2203669.

7 S. Bi, Z. Deng, J. Huang, X. Wen and S. Zeng, *Adv. Mater.*, 2023, **35**, e2207038.

8 Y. Chang, H. Chen, X. Xie, Y. Wan, Q. Li, F. Wu, R. Yang, W. Wang and X. Kong, *Nat. Commun.*, 2023, **14**, 1079.

9 S. Diao, J. L. Blackburn, G. Hong, A. L. Antaris, J. Chang, J. Z. Wu, B. Zhang, K. Cheng, C. J. Kuo and H. Dai, *Angew. Chem.*, 2015, **127**, 14971–14975.

10 X. Qian, Y. Zheng and Y. Chen, *Adv. Mater.*, 2016, **28**, 8097–8129.

11 M. P. Brenner, S. Hilgenfeldt and D. Lohse, *Rev. Mod. Phys.*, 2002, **74**, 425.

12 A. Feng and P. F. Smet, *Materials*, 2018, **11**, 484.

13 Y. Li, M. Jiang, Z. Deng, S. Zeng and J. Hao, *Adv. Sci.*, 2021, **8**, e2004391.

14 M. Ma, J. Wang, H. Jiang, Q. Chen, Y. Xiao, H. Yang and L. Lin, *Acta Biomater.*, 2023, **155**, 635–643.

15 Z.-F. Zhang, H. Cui, C.-Z. Lai and L.-J. Liu, *Anal. Chem.*, 2005, **77**, 3324–3329.

16 M. Vacher, I. Fdez. Galván, B.-W. Ding, S. Schramm, R. Berraud-Pache, P. Naumov, N. Ferre, Y.-J. Liu, I. Navizet and D. Roca-Sanjuan, *Chem. Rev.*, 2018, **118**, 6927–6974.

17 A. García-Campaña and W. Baeyens, *Analusis*, 2000, **28**, 686–698.

18 H. An, C. Guo, D. Li, R. Liu, X. Xu, J. Guo, J. Ding, J. Li, W. Chen and J. Zhang, *ACS Appl. Mater. Interfaces*, 2020, **12**, 17230–17243.

19 Z. Chen, Y. Tan, K. Xu, L. Zhang, B. Qiu, L. Guo, Z. Lin and G. Chen, *Biosens. Bioelectron.*, 2016, **75**, 8–14.

20 M. Wu, L. Wu, J. Li, D. Zhang, S. Lan, X. Zhang, X. Lin, G. Liu, X. Liu and J. Liu, *Theranostics*, 2019, **9**, 20–33.

21 Z. Zhou, X. Liu, L. Yue and I. Willner, *ACS Nano*, 2018, **12**, 10725–10735.

22 H. Liu, Y. Su, D. Deng, H. Song and Y. Lv, *Anal. Chem.*, 2019, **91**, 9174–9180.

23 S. Y. Yin, W. Liu, K. Zhang and J. Li, *ACS Appl. Bio Mater.*, 2021, **4**, 3490–3498.

24 L. Cai, L. Deng, X. Huang and J. Ren, *Anal. Chem.*, 2018, **90**, 6929–6935.

25 Z. Gu, A. Fu, L. Ye, K. Kuerban, Y. Wang and Z. Cao, *ACS Sens.*, 2019, **4**, 2922–2929.

26 Y. Hou, R. Han, Y. Sun, C. Luo and X. Wang, *Anal. Chim. Acta*, 2022, **1195**, 339386.

27 L. Han, Y. Li and A. Fan, *Luminescence*, 2018, **33**, 751–758.

28 Y. Wang, M. Wang, L. Han, Y. Zhao and A. Fan, *Talanta*, 2018, **182**, 523–528.

29 Z. Abolghasemi-Fakhri, M. Amjadi and J. L. Manzoori, *Spectrochim. Acta, Part A*, 2019, **216**, 85–90.

30 Y. Tian, Y. Zhang, X. Lu, D. Xiao and C. Zhou, *J. Mater. Chem. B*, 2023, **11**, 2200–2206.

31 H. Chen, F. Gao, R. He and D. Cui, *J. Colloid Interface Sci.*, 2007, **315**, 158–163.

32 F. Zheng, W. Ke, Y. Zhao and C. Xu, *Electrophoresis*, 2019, **40**, 2218–2226.

33 Y. Qi, B. Li and F. Xiu, *Spectrochim. Acta, Part A*, 2014, **128**, 76–81.

34 Y. Wu, J. Wang and H. Cui, *Anal. Bioanal. Chem.*, 2022, **414**, 367–375.

35 W. H. Chen, M. Vázquez-González, A. Kozell, A. Cecconello and I. Willner, *Small*, 2018, **14**, 1703149.

36 L. He, Z. W. Jiang, W. Li, C. M. Li, C. Z. Huang and Y. F. Li, *ACS Appl. Mater. Interfaces*, 2018, **10**, 28868–28876.

37 Z. Wang, F. Liu and C. Lu, *Biosens. Bioelectron.*, 2014, **60**, 237–243.

38 S. Bi, B. Xiu, J. Ye and Y. Dong, *ACS Appl. Mater. Interfaces*, 2015, **7**, 23310–23319.

39 Y. Sun, L. Shi, Q. Wang, L. Mi and T. Li, *Anal. Chem.*, 2019, **91**, 3652–3658.

40 J. Hassanzadeh and A. Khataee, *Talanta*, 2018, **178**, 992–1000.

41 M. Zhou, Q. Chen, A. Wang, J. Li and Y. Ma, *Luminescence*, 2019, **34**, 673–679.

42 M. Amjadi, J. L. Manzoori, T. Hallaj and M. H. Sorouraddin, *Spectrochim. Acta, Part A*, 2014, **122**, 715–720.

43 T. Hallaj, M. Amjadi, J. L. Manzoori and N. Azizi, *Luminescence*, 2017, **32**, 1174–1179.

44 E. Delnavaz and M. Amjadi, *Mikrochim. Acta*, 2021, **188**, 278.

45 J. Li, Y. Han, X. Li, L. Xiong, L. Wei and X. Cheng, *Luminescence*, 2021, **36**, 79–84.

46 Z. Lin, X. Dou, H. Li, Y. Ma and J. M. Lin, *Talanta*, 2015, **132**, 457–462.

47 Y. Haghighi Shishavan and M. Amjadi, *Luminescence*, 2022, **37**, 734–741.

48 S. Han, Z. Fan, X. Chen, Y. Wu and J. Wang, *Spectrochim. Acta, Part A*, 2017, **183**, 103–108.

2926 | *Chem. Soc. Rev.*, 2024, **53**, 2898–2931

This journal is © The Royal Society of Chemistry 2024

49 Y. Li, J. Wang, Y. Yang and S. Han, *Luminescence*, 2020, **35**, 773–780.

50 M. Amjadi, T. Hallaj and F. Mirbirang, *Mikrochim. Acta*, 2020, **187**, 191.

51 Y. H. Seo, A. Singh, H. J. Cho, Y. Kim, J. Heo, C. K. Lim, S. Y. Park, W. D. Jang and S. Kim, *Biomaterials*, 2016, **84**, 111–118.

52 H. Chen, H. Li and J. M. Lin, *Anal. Chem.*, 2012, **84**, 8871–8879.

53 R. Chen, L. Zhang, J. Gao, W. Wu, Y. Hu and X. Jiang, *J. Biomed. Biotechnol.*, 2011, **2011**, 679492.

54 S. Y. Yin, W. Liu, J. Yang and J. Li, *J. Mater. Chem. B*, 2021, **9**, 5877–5886.

55 Y. C. Chen, Y. J. Liu, C. L. Lee, K. Y. Pham, D. Manoharan, S. Thangudu, C. H. Su and C. S. Yeh, *Adv. Healthcare Mater.*, 2022, **11**, e2201613.

56 J. Wang, C. Yao, B. Shen, X. Zhu, Y. Li, L. Shi, Y. Zhang, J. Liu, Y. Wang and L. Sun, *Theranostics*, 2019, **9**, 608–619.

57 Q. Mao, J. Fang, A. Wang, Y. Zhang, C. Cui, S. Ye, Y. Zhao, Y. Feng, J. Li and H. Shi, *Angew. Chem., Int. Ed.*, 2021, **60**, 23805–23811.

58 Y. Zhou, W. Wu, P. Yang, D. Mao and B. Liu, *Biomaterials*, 2022, **288**, 121693.

59 C. Sun, Z. Wang, L. Yue, Q. Huang, S. Lu and R. Wang, *J. Mater. Chem. B*, 2020, **8**, 8878–8883.

60 P. N. Prasad, *Introduction to biophotonics*, John Wiley & Sons, 2004.

61 F. Wang, Y. Han, C. S. Lim, Y. Lu, J. Wang, J. Xu, H. Chen, C. Zhang, M. Hong and X. Liu, *Nature*, 2010, **463**, 1061–1065.

62 H. Li, E. Heydari, Y. Li, H. Xu, S. Xu, L. Chen and G. Bai, *Nanomaterials*, 2023, **13**, 219.

63 G. Chen, H. Qiu, P. N. Prasad and X. Chen, *Chem. Rev.*, 2014, **114**, 5161–5214.

64 Q. Liu, J. Tian, Y. Tian, Q. Sun, D. Sun, F. Wang, H. Xu, G. Ying, J. Wang, A. K. Yetisen and N. Jiang, *ACS Nano*, 2021, **15**, 515–525.

65 X. Wang, H. Li, F. Li, X. Han and G. Chen, *Nanoscale*, 2019, **11**, 22079–22088.

66 H. M. Gong, S. Xiao, X. R. Su, J. B. Han and Q. Q. Wang, *Opt. Express*, 2007, **15**, 13924–13929.

67 Z. Cheng, R. Chai, P. Ma, Y. Dai, X. Kang, H. Lian, Z. Hou, C. Li and J. Lin, *Langmuir*, 2013, **29**, 9573–9580.

68 R. Tian, W. Sun, M. Li, S. Long, M. Li, J. Fan, L. Guo and X. Peng, *Chem. Sci.*, 2019, **10**, 10106–10112.

69 J. Park, A. Estrada, K. Sharp, K. Sang, J. A. Schwartz, D. K. Smith, C. Coleman, J. D. Payne, B. A. Korgel, A. K. Dunn and J. W. Tunnell, *Opt. Express*, 2008, **16**, 1590–1599.

70 N. Akizuki, S. Aota, S. Mouri, K. Matsuda and Y. Miyauchi, *Nat. Commun.*, 2015, **6**, 8920.

71 S. Míguez-Lago, I. F. A. Mariz, M. A. Medel, J. M. Cuerva, E. Maçôas, C. M. Cruz and A. G. Campaña, *Chem. Sci.*, 2022, **13**, 10267–10272.

72 Y. Zhang, T. T. Shen, H. L. Zhang, A. M. Kirillov, H. J. Cai, J. Wu, W. S. Liu and Y. Tang, *Chem. Commun.*, 2016, **52**, 4880–4883.

73 F. Wang and X. Liu, *Chem. Soc. Rev.*, 2009, **38**, 976–989.

74 L. Zhang, L. Zeng, Y. Pan, S. Luo, W. Ren, A. Gong, X. Ma, H. Liang, G. Lu and A. Wu, *Biomaterials*, 2015, **44**, 82–90.

75 K. Prorok, M. Olk, M. Skowicki, A. Kowalczyk, A. Kotulska, T. Lipiński and A. Bednarkiewicz, *Nanoscale Adv.*, 2019, **1**, 3463–3473.

76 G. S. Yi and G. M. Chow, *Adv. Funct. Mater.*, 2006, **16**, 2324–2329.

77 C. Mi, J. Zhou, F. Wang and D. Jin, *Nanoscale*, 2019, **11**, 12547–12552.

78 Q. Feng, W. Zheng, J. Pu, Q. Chen and W. Shao, *Front. Chem.*, 2021, **9**, 690833.

79 H. Wang, Y. Xu, T. Pang, B. Chen, F. Xin, M. Xing, M. Tian, Y. Fu, X. Luo and Y. Tian, *Nanoscale*, 2022, **14**, 962–968.

80 J. A. Damasco, G. Chen, W. Shao, H. Ågren, H. Huang, W. Song, J. F. Lovell and P. N. Prasad, *ACS Appl. Mater. Interfaces*, 2014, **6**, 13884–13893.

81 X. Wang, K. Liu, G. Yang, L. Cheng, L. He, Y. Liu, Y. Li, L. Guo and Z. Liu, *Nanoscale*, 2014, **6**, 9198–9205.

82 J. Li, Y. Long, Q. Zhao, S. Zheng, Z. Fang and B. O. Guan, *Nanomaterials*, 2021, **11**, 1033.

83 Q. Y. Meng, B. J. Chen, S. C. Lü, J. T. Sun and X. R. Qu, *Guangpuxue Yu Guangpu Fenxi*, 2010, **30**, 1224–1228.

84 H. Niioka, S. Fukushima, M. Ichimiya, M. Ashida, J. Miyake, T. Araki and M. Hashimoto, *Microscopy*, 2014, **63**(Suppl 1), i29.

85 J. Liu, L. Huang, X. Tian, X. Chen, Y. Shao, F. Xie, D. Chen and L. Li, *Int. J. Nanomed.*, 2017, **12**, 1–14.

86 C. Wang, L. Xu, J. Xu, D. Yang, B. Liu, S. Gai, F. He and P. Yang, *Dalton Trans.*, 2017, **46**, 12147–12157.

87 S. Ryszczyńska and T. Grzyb, *Methods Appl. Fluoresc.*, 2022, **10**, 024001.

88 Y. Li, R. Wang, W. Zheng and Y. Li, *Inorg. Chem.*, 2019, **58**, 8230–8236.

89 Z. Giedraityte, M. Tuomisto, M. Lastusaari and M. Karppinen, *ACS Appl. Mater. Interfaces*, 2018, **10**, 8845–8852.

90 Y. Li, G. Bai, S. Zeng and J. Hao, *ACS Appl. Mater. Interfaces*, 2019, **11**, 4737–4744.

91 F. Huang, Y. Li, J. Liu, J. Zhang, X. Wang, B. Li, H. Chang, Y. Miao and Y. Sun, *ACS Appl. Bio Mater.*, 2021, **4**, 5695–5706.

92 S. Sekiyama, M. Umezawa, S. Kuraoka, T. Ube, M. Kamimura and K. Soga, *Sci. Rep.*, 2018, **8**, 16979.

93 Z. Zhang, Y. Yang, M. Zhao, L. Lu, F. Zhang and Y. Fan, *ACS Appl. Bio Mater.*, 2022, **5**, 2935–2942.

94 D. E. Hudson, D. O. Hudson, J. M. Wininger and B. D. Richardson, *Photomed. Laser Surg.*, 2013, **31**, 163–168.

95 C. Cao, M. Xue, X. Zhu, P. Yang, W. Feng and F. Li, *ACS Appl. Mater. Interfaces*, 2017, **9**, 18540–18548.

96 D. Zhao, X. Han, S. Wang, J. Liu, Y. Lu and C. Li, *Chemistry*, 2020, **26**, 3145–3151.

97 M. Lesniak, M. Kochanowicz, A. Baranowska, P. Golonko, M. Kuwik, J. Zmojda, P. Miluski, J. Dorosz, W. A. Pisarski, J. Pisarska and D. Dorosz, *Nanomaterials*, 2021, **11**, 2115.

98 S. Li, Q. Ma, C. Wang, K. Yang, Z. Hong, Q. Chen, J. Song, X. Song and H. Yang, *Anal. Chem.*, 2022, **94**, 2641–2647.

This journal is © The Royal Society of Chemistry 2024

Chem. Soc. Rev., 2024, **53**, 2898–2931 | **2927**

99 F. Bertorelle, K. D. Wegner, M. Perić Bakulić, H. Fakhouri, C. Comby-Zerbino, A. Sagar, P. Bernadó, U. Resch-Genger, V. Bonačić-Koutecký, X. Le Guével and R. Antoine, *Chemistry*, 2022, **28**, e202200570.

100 W. Zhang, S. Chen, P. Sun, S. Ye, Q. Fan, J. Song, P. Zeng, J. Qu and W. Y. Wong, *Adv. Healthcare Mater.*, 2022, **11**, e2200467.

101 S. Mateos, J. Lifante, C. Li, E. C. Ximendes, T. Muñoz-Ortiz, J. Yao, M. de la Fuente-Fernández, L. García Villalón, Á. M. Granado, I. Zabala Gutierrez, J. Rubio-Retama, D. Jaque, D. H. Ortgies and N. Fernández, *Small*, 2020, **16**, e1907171.

102 O. Yarema, M. Yarema and V. Wood, *Chem. Mater.*, 2018, **30**, 1446–1461.

103 J. Li, T. Guan, D. Tu, W. Lian, P. Zhang, S. Han, F. Wen and X. Chen, *Chem. Commun.*, 2022, **58**, 2204–2207.

104 T. Maldiney, A. Bessière, J. Seguin, E. Teston, S. K. Sharma, B. Viana, A. J. Bos, P. Dorenbos, M. Bessodes and D. Gourier, *Nat. Mater.*, 2014, **13**, 418–426.

105 J. L. Li, J. P. Shi, C. C. Wang, P. H. Li, Z. F. Yu and H. W. Zhang, *Nanoscale*, 2017, **9**, 8631–8638.

106 L. Song, P. P. Li, W. Yang, X. H. Lin, H. Liang, X. F. Chen, G. Liu, J. Li and H. H. Yang, *Adv. Funct. Mater.*, 2018, **28**, 1707496.

107 X. Zhao, K. C. Zhao, L. J. Chen, Y. S. Liu, J. L. Liu and X. P. Yan, *Chem. Sci.*, 2020, **12**, 442–452.

108 X. Chen, Y. Li, K. Huang, L. Huang, X. Tian, H. Dong, R. Kang, Y. Hu, J. Nie, J. Qiu and G. Han, *Adv. Mater.*, 2021, **33**, e2008722.

109 X. Qiu, X. Zhu, M. Xu, W. Yuan, W. Feng and F. Li, *ACS Appl. Mater. Interfaces*, 2017, **9**, 32583–32590.

110 L. Hu, P. Wang, M. Zhao, L. Liu, L. Zhou, B. Li, F. H. Albaqami, A. M. El-Toni, X. Li, Y. Xie, X. Sun and F. Zhang, *Biomaterials*, 2018, **163**, 154–162.

111 Z. Xue, X. Li, Y. Li, M. Jiang, G. Ren, H. Liu, S. Zeng and J. Hao, *Nanoscale*, 2017, **9**, 7276–7283.

112 R. D. Scurlock, B. Wang, P. R. Ogilby, J. R. Sheats and R. L. Clough, *J. Am. Chem. Soc.*, 1995, **117**, 10194–10202.

113 C. Xie, Y. Lyu, X. Zhen, Q. Miao and K. Pu, *ACS Appl. Bio Mater.*, 2018, **1**, 1147–1153.

114 C. Xie, X. Zhen, Q. Miao, Y. Lyu and K. Pu, *Adv. Mater.*, 2018, **30**, e1801331.

115 L. Wu, Y. Ishigaki, Y. Hu, K. Sugimoto, W. Zeng, T. Harimoto, Y. Sun, J. He, T. Suzuki, X. Jiang, H. Y. Chen and D. Ye, *Nat. Commun.*, 2020, **11**, 446.

116 G.-S. Yi and G.-M. Chow, *Chem. Mater.*, 2007, **19**, 341–343.

117 L. Wu, M. Jia, D. Li and G. Chen, *Nano Lett.*, 2023, **23**, 2862–2869.

118 T. Wang, M. Yang, J. Huang, Y. Zhao, H. Wang, S. Leng, J. Chen, G. Sun and J. Liu, *Sci. Bull.*, 2017, **62**, 903–912.

119 Y. Dai, H. Xiao, J. Liu, Q. Yuan, P. Ma, D. Yang, C. Li, Z. Cheng, Z. Hou, P. Yang and J. Lin, *J. Am. Chem. Soc.*, 2013, **135**, 18920–18929.

120 A. Xia, Y. Gao, J. Zhou, C. Li, T. Yang, D. Wu, L. Wu and F. Li, *Biomaterials*, 2011, **32**, 7200–7208.

121 N. Erathodiyil and J. Y. Ying, *Acc. Chem. Res.*, 2011, **44**, 925–935.

122 Q. Lü, A. Li, F. Guo, L. Sun and L. Zhao, *Nanotechnology*, 2008, **19**, 205704.

123 S. Dong, J. Xu, T. Jia, M. Xu, C. Zhong, G. Yang, J. Li, D. Yang, F. He, S. Gai, P. Yang and J. Lin, *Chem. Sci.*, 2019, **10**, 4259–4271.

124 X. Chen, Y. Tang, A. Liu, Y. Zhu, D. Gao, Y. Yang, J. Sun, H. Fan and X. Zhang, *ACS Appl. Mater. Interfaces*, 2018, **10**, 14378–14388.

125 A. Gulzar, J. Xu, D. Yang, L. Xu, F. He, S. Gai and P. Yang, *Dalton Trans.*, 2018, **47**, 3931–3939.

126 W. Wang, M. Zhao, L. Wang and H. Chen, *Mikrochim. Acta*, 2019, **186**, 630.

127 M. Tang, X. Zhu, Y. Zhang, Z. Zhang, Z. Zhang, Q. Mei, J. Zhang, M. Wu, J. Liu and Y. Zhang, *ACS Nano*, 2019, **13**, 10405–10418.

128 X. Chuai, Z. Liu, Y. Liu, C. He and W. Qin, *J. Nanosci. Nanotechnol.*, 2014, **14**, 3687–3689.

129 J. Zhao, Y. Hu, S. W. Lin, U. Resch-Genger, R. Zhang, J. Wen, X. Kong, A. Qin and J. Ou, *J. Mater. Chem. B*, 2020, **8**, 6481–6489.

130 J. Yin, H. Zheng, W. Zhang, L. Shen, R. Lai, L. Tian, F. Zhao and Y. Shao, *Opt. Express*, 2022, **30**, 32459–32473.

131 Y. Li, F. Li, Y. Huang, H. Wu, J. Wang, J. Yang, Q. Xiao and H. Lin, *RSC Adv.*, 2019, **9**, 18070–18075.

132 Y. Zhong, Z. Ma, F. Wang, X. Wang, Y. Yang, Y. Liu, X. Zhao, J. Li, H. Du, M. Zhang, Q. Cui, S. Zhu, Q. Sun, H. Wan, Y. Tian, Q. Liu, W. Wang, K. C. Garcia and H. Dai, *Nat. Biotechnol.*, 2019, **37**, 1322–1331.

133 D. Kang, H. J. Ahn, J. Lee, S. K. Kim, J. Pyun, C. S. Song, S. J. Kim and J. Lee, *Biosens. Bioelectron.*, 2021, **190**, 113369.

134 D. Karthickraja, G. A. Kumar, D. K. Sardar, S. Karthi, G. C. Dannangoda, K. S. Martirosyan, M. Prasath, M. Gowri and E. K. Girija, *Mater. Sci. Eng., C*, 2021, **125**, 112095.

135 T. Song, M. Zhang, Y. Liu, J. Yang, Z. Gong, H. Yan, H. Zhu, D. Yan, C. Liu and C. Xu, *RSC Adv.*, 2018, **8**, 10954–10963.

136 Z. F. Yu, J. P. Shi, J. L. Li, P. H. Li and H. W. Zhang, *J. Mater. Chem. B*, 2018, **6**, 1238–1243.

137 E. Pan, G. Bai, J. Zhou, L. Lei and S. Xu, *Nanoscale*, 2019, **11**, 11642–11648.

138 C. Cao, N. Wu, W. Yuan, Y. Gu, J. Ke, W. Feng and F. Li, *Nanoscale*, 2020, **12**, 8248–8254.

139 S. J. Kwon, G. Y. Lee, K. Jung, H. S. Jang, J. S. Park, H. Ju, I. K. Han and H. Ko, *Adv. Mater.*, 2016, **28**, 7899–7909.

140 L. M. Wiesholler, C. Genslein, A. Schroter and T. Hirsch, *Anal. Chem.*, 2018, **90**, 14247–14254.

141 D. Lu, S. K. Cho, S. Ahn, L. Brun, C. J. Summers and W. Park, *ACS Nano*, 2014, **8**, 7780–7792.

142 Y. Ji, W. Xu, N. Ding, H. Yang, H. Song, Q. Liu, H. Ågren, J. Widengren and H. Liu, *Light: Sci. Appl.*, 2020, **9**, 184.

143 Y. Zhang, J. Wang, F. Nan and Q. Q. Wang, *RSC Adv.*, 2018, **8**, 20056–20060.

144 Z. Zhang, Y. Liu, Y. Fang, B. Cao, J. Huang, K. Liu and B. Dong, *Adv. Sci.*, 2018, **5**, 1800748.

145 W. Zhang, T. Chen, L. Su, X. Ge, X. Chen, J. Song and H. Yang, *Anal. Chem.*, 2020, **92**, 6094–6102.

2928 | *Chem. Soc. Rev.*, 2024, **53**, 2898–2931

This journal is © The Royal Society of Chemistry 2024

146 J. Huang, X. Zhang, S. Li, F. Qu, B. Huang, R. Cui, Y. Liu, W. Hu, X. Yang and Y. Zhang, *Anal. Chem.*, 2023, **95**, 3761–3768.

147 A. R. Hong, J. S. Han, G. Kang, H. Ko and H. S. Jang, *Materials*, 2020, **13**, 5338.

148 T. Yu, D. M. Wei, Z. Li, L. J. Pan, Z. L. Zhang, Z. Q. Tian and Z. Liu, *Chem. Commun.*, 2020, **56**, 1976–1979.

149 Q. Wang, T. Liang, J. Wu, Z. Li and Z. Liu, *ACS Appl. Mater. Interfaces*, 2021, **13**, 29303–29312.

150 D. K. Chatterjee and Z. Yong, 2008.

151 J. Shan, S. J. Budijono, G. Hu, N. Yao, Y. Kang, Y. Ju and R. K. Prud'homme, *Adv. Funct. Mater.*, 2011, **21**, 2488–2495.

152 K. Liu, X. Liu, Q. Zeng, Y. Zhang, L. Tu, T. Liu, X. Kong, Y. Wang, F. Cao, S. A. Lambrechts, M. C. Aalders and H. Zhang, *ACS Nano*, 2012, **6**, 4054–4062.

153 K. Tezuka, M. Umezawa, T. I. Liu, K. Nomura, K. Okubo, H. C. Chiu, M. Kamimura and K. Soga, *ACS Appl. Bio Mater.*, 2021, **4**, 4462–4469.

154 S. Jin, L. Zhou, Z. Gu, G. Tian, L. Yan, W. Ren, W. Yin, X. Liu, X. Zhang, Z. Hu and Y. Zhao, *Nanoscale*, 2013, **5**, 11910–11918.

155 H. Zhao, Y. Li, X. Zhang, K. Wu, J. Lv, C. Chen, H. Liu, Z. Shi, H. Ju and Y. Liu, *Biomaterials*, 2022, **291**, 121873.

156 L. Cai, Z. Wang, B. Lin, K. Liu, Y. Wang, Y. Yuan, X. Tao and R. Lv, *Nanoscale Adv.*, 2022, **4**, 2224–2232.

157 F. Ai, Q. Ju, X. Zhang, X. Chen, F. Wang and G. Zhu, *Sci. Rep.*, 2015, **5**, 10785.

158 J. Choi and S. Y. Kim, *J. Biomater. Appl.*, 2022, **37**, 646–658.

159 D. Wang, L. Zhu, Y. Pu, J. X. Wang, J. F. Chen and L. Dai, *Nanoscale*, 2017, **9**, 11214–11221.

160 R. Lv, P. Yang, G. Chen, S. Gai, J. Xu and P. N. Prasad, *Sci. Rep.*, 2017, **7**, 13562.

161 F. S. Mackay, J. A. Woods, P. Heringová, J. Kašpárková, A. M. Pizarro, S. A. Moggach, S. Parsons, V. Brabec and P. J. Sadler, *Proc. Natl. Acad. Sci. U. S. A.*, 2007, **104**, 20743–20748.

162 G. Kuang, H. Lu, S. He, H. Xiong, J. Yu, Q. Zhang and Y. Huang, *Adv. Healthcare Mater.*, 2021, **10**, e2100938.

163 Y. Yu, Y. Huang, W. Feng, M. Yang, B. Shao, J. Li and F. Ye, *RSC Adv.*, 2021, **11**, 29065–29072.

164 N. Niu, F. He, P. Ma, S. Gai, G. Yang, F. Qu, Y. Wang, J. Xu and P. Yang, *ACS Appl. Mater. Interfaces*, 2014, **6**, 3250–3262.

165 F. Zheng, C. Wang, T. Meng, Y. Zhang, P. Zhang, Q. Shen, Y. Zhang, J. Zhang, J. Li, Q. Min, J. Chen and J. J. Zhu, *ACS Nano*, 2019, **13**, 12577–12590.

166 R. Cui, W. Sun, M. Liu, J. Shi and Z. Liu, *ACS Appl. Mater. Interfaces*, 2021, **13**, 59164–59173.

167 H. Cai, T. Shen, A. M. Kirillov, Y. Zhang, C. Shan, X. Li, W. Liu and Y. Tang, *Inorg. Chem.*, 2017, **56**, 5295–5304.

168 Y. Cao, K. Wang, P. Zhu, X. Zou, G. Ma, W. Zhang, D. Wang, J. Wan, Y. Ma, X. Sun and J. Dong, *Colloids Surf., B*, 2022, **213**, 112393.

169 Z. Wei, X. Liu, D. Niu, L. Qin and Y. Li, *ACS Appl. Bio Mater.*, 2020, **3**, 4655–4664.

170 G. Chen, R. Jaskula-Sztul, C. R. Esquibel, I. Lou, Q. Zheng, A. Dammalapati, A. Harrison, K. W. Eliceiri, W. Tang, H. Chen and S. Gong, *Adv. Funct. Mater.*, 2017, 27.

171 Y. Liu, Y. Liu, W. Bu, C. Cheng, C. Zuo, Q. Xiao, Y. Sun, D. Ni, C. Zhang and J. Liu, *Angew. Chem.*, 2015, **127**, 8223–8227.

172 J. Han, H. Xia, Y. Wu, S. N. Kong, A. Deivasigamani, R. Xu, K. M. Hui and Y. Kang, *Nanoscale*, 2016, **8**, 7861–7865.

173 J. Xu, A. Gulzar, Y. Liu, H. Bi, S. Gai, B. Liu, D. Yang, F. He and P. Yang, *Small*, 2017, **13**, 1701841.

174 J. Liu, J. Zhang, F. Huang, Y. Deng, B. Li, R. Ouyang, Y. Miao, Y. Sun and Y. Li, *Acta Biomater.*, 2020, **113**, 570–583.

175 K. Du, S. Zhao, J. Feng, X. Gao, K. Liu, X. Wang, M. Zhang, Y. Li, Y. Lu and H. Zhang, *J. Mater. Chem. B*, 2021, **9**, 7216–7228.

176 X. Chen, J. Song, X. Chen and H. Yang, *Chem. Soc. Rev.*, 2019, **48**, 3073–3101.

177 G. Song, L. Cheng, Y. Chao, K. Yang and Z. Liu, *Adv. Mater.*, 2017, **29**, 1700996.

178 I. N. Stanton, J. A. Ayres and M. J. Therien, *Dalton Trans.*, 2012, **41**, 11576–11578.

179 D. Maiti, H. Yu, B. S. Kim, M. Naito, S. Yamashita, H. J. Kim and K. Miyata, *ACS Appl. Bio Mater.*, 2022, **5**, 5477–5486.

180 B. P. Quigley, C. D. Smith, S. H. Cheng, J. S. Souris, C. A. Pelizzari, C. T. Chen, L. W. Lo, C. S. Reft, R. D. Wiersma and P. J. La Riviere, *Med. Phys.*, 2017, **44**, 5367–5377.

181 M. C. Micheletto, J. Guidelli É and A. J. Costa-Filho, *ACS Appl. Mater. Interfaces*, 2021, **13**, 2289–2302.

182 G. R. Waetzig, G. A. Horrocks, J. W. Jude, L. Zuin and S. Banerjee, *Nanoscale*, 2016, **8**, 979–986.

183 F. Ahmad, X. Wang, Z. Jiang, X. Yu, X. Liu, R. Mao, X. Chen and W. Li, *ACS Nano*, 2019, **13**, 10419–10433.

184 L. Sudheendra, G. K. Das, C. Li, D. Stark, J. Cena, S. Cherry and I. M. Kennedy, *Chem. Mater.*, 2014, **26**, 1881–1888.

185 D. Kirsanova, V. Polyakov, V. Butova, P. Zolotukhin, A. Belanova, Z. Gadzhimagomedova, M. Soldatov, I. Pankin and A. Soldatov, *Nanomaterials*, 2021, **11**, 3212.

186 X. Zhong, X. Wang, G. Zhan, Y. Tang, Y. Yao, Z. Dong, L. Hou, H. Zhao, S. Zeng, J. Hu, L. Cheng and X. Yang, *Nano Lett.*, 2019, **19**, 8234–8244.

187 M. Müller, Y. Wang, M. R. Squillante, K. D. Held, R. R. Anderson and M. Purschke, *Radiother. Oncol.*, 2018, **129**, 589–594.

188 D. Manoharan, L. C. Chang, L. C. Wang, Y. S. Shan, F. C. Lin, L. C. Wu, H. S. Sheu, W. P. Su and C. S. Yeh, *ACS Nano*, 2021, **15**, 9084–9100.

189 Q. Zhang, B. Yan, F. Lei and H. H. Chen, *Nanoscale*, 2012, **4**, 7646–7648.

190 D. Avram, B. Cojocaru, A. Urda, I. Tiseanu, M. Florea and C. Tiseanu, *Phys. Chem. Chem. Phys.*, 2015, **17**, 30988–30992.

191 M. V. Rezende, P. J. Montes, A. B. Andrade, Z. S. Macedo and M. E. Valerio, *Phys. Chem. Chem. Phys.*, 2016, **18**, 17646–17654.

192 Z. Jiang, L. He, X. Yu, Z. Yang, W. Wu, X. Wang, R. Mao, D. Cui, X. Chen and W. Li, *ACS Nano*, 2021, **15**, 11112–11125.

193 L. Q. Guan, S. Shi, X. W. Niu, S. C. Guo, J. Zhao, T. M. Ji, H. Dong, F. Y. Jia, J. W. Xiao, L. D. Sun and C. H. Yan, *Adv. Sci.*, 2022, **9**, e2201354.

This journal is © The Royal Society of Chemistry 2024

Chem. Soc. Rev., 2024, **53**, 2898–2931 | **2929**

194 H. Chen, G. D. Wang, Y. J. Chuang, Z. Zhen, X. Chen, P. Biddinger, Z. Hao, F. Liu, B. Shen, Z. Pan and J. Xie, *Nano Lett.*, 2015, **15**, 2249–2256.

195 B. Cline and J. Xie, *Methods Mol. Biol.*, 2022, **2394**, 811–822.

196 L. Zhang, X. Wang, X. Wang, X. Wang, Y. Luo, C. Tan, L. Jiang, Y. Wang and W. Liu, *Inorg. Chem.*, 2023, **62**, 6421–6427.

197 C. Yang, L. Ma, J. Maley, R. Sammynaiken, R. Feng, G. Xiang and W. Chen, *J. Biomed. Nanotechnol.*, 2013, **9**, 1827–1836.

198 Y. Osakada, G. Pratx, C. Sun, M. Sakamoto, M. Ahmad, O. Volotskova, Q. Ong, T. Teranishi, Y. Harada, L. Xing and B. Cui, *Chem. Commun.*, 2014, **50**, 3549–3551.

199 L. Luo, W. Sun, Y. Feng, R. Qin, J. Zhang, D. Ding, T. Shi, X. Liu, X. Chen and H. Chen, *ACS Appl. Mater. Interfaces*, 2020, **12**, 12591–12599.

200 S. Shrestha, J. Wu, B. Sah, A. Vanasse, L. N. Cooper, L. Ma, G. Li, H. Zheng, W. Chen and M. P. Antosh, *Proc. Natl. Acad. Sci. U. S. A.*, 2019, **116**, 16823–16828.

201 K. Kirakci, T. N. Pozmogova, A. Y. Protasevich, G. D. Vavilov, D. V. Stass, M. A. Shestopalov and K. Lang, *Biomater. Sci.*, 2021, **9**, 2893–2902.

202 K. Vanheusden, C. Seager, W. T. Warren, D. Tallant and J. Voigt, *Appl. Phys. Lett.*, 1996, **68**, 403–405.

203 Z. Wang, C. Li, L. Liu and T. K. Sham, *J. Chem. Phys.*, 2013, **138**, 084706.

204 A. Vejdani Noghreiyan, M. R. Sazegar, S. A. Mousavi Shaegh and A. Sazgarnia, *Photodiagn. Photodyn. Ther.*, 2020, **30**, 101770.

205 L. Armelao, F. Heigl, S. Brunet, R. Sammynaiken, T. Regier, R. I. Blyth, L. Zuin, R. Sankari, J. Vogt and T. K. Sham, *ChemPhysChem*, 2010, **11**, 3625–3631.

206 H. Deng, L. Lin, S. Wang, G. Yu, Z. Zhou, Y. Liu, G. Niu, J. Song and X. Chen, *Adv. Mater.*, 2019, **31**, e1903443.

207 F. Zhang, Y. Zhou, Z. Chen, M. Wang, Z. Ma, X. Chen, M. Jia, D. Wu, J. Xiao, X. Li, Y. Zhang, Z. Shi and C. Shan, *Adv. Mater.*, 2022, **34**, e2204801.

208 X. Ou, X. Qin, B. Huang, J. Zan, Q. Wu, Z. Hong, L. Xie, H. Bian, Z. Yi, X. Chen, Y. Wu, X. Song, J. Li, Q. Chen, H. Yang and X. Liu, *Nature*, 2021, **590**, 410–415.

209 Y. Wu, L. Su, M. Yuan, T. Chen, J. Ye, Y. Jiang, J. Song and H. Yang, *Angew. Chem., Int. Ed.*, 2021, **60**, 12868–12875.

210 X. Jiang, X. Gao, L. Li, P. Zhou, S. Wang, T. Liu, J. Zhou, H. Zhang, K. Huang, Y. Li, M. Wang, Z. Jin, E. Xie, W. Liu and G. Han, *ACS Appl. Mater. Interfaces*, 2023, **15**, 21228–21238.

211 Z. Xue, X. Li, Y. Li, M. Jiang, H. Liu, S. Zeng and J. Hao, *ACS Appl. Mater. Interfaces*, 2017, **9**, 22132–22142.

212 Z. Xue, M. Jiang, H. Liu, S. Zeng and J. Hao, *Biomaterials*, 2020, **263**, 120384.

213 H. Jiang, R. Wang, Q. Zhang, L. Song, X. Sun, J. Shi and Y. Zhang, *Nanoscale*, 2022, **14**, 15451–15461.

214 R. Jiang, J. Yang, Y. Meng, D. Yan, C. Liu, C. Xu and Y. Liu, *Dalton Trans.*, 2020, **49**, 6074–6083.

215 S. Zheng, J. Shi, X. Fu, C. Wang, X. Sun, C. Chen, Y. Zhuang, X. Zou, Y. Li and H. Zhang, *Nanoscale*, 2020, **12**, 14037–14046.

216 Y. Zhuang, D. Chen, W. Chen, W. Zhang, X. Su, R. Deng, Z. An, H. Chen and R. J. Xie, *Light: Sci. Appl.*, 2021, **10**, 132.

217 J. Ma, W. Zhu, L. Lei, D. Deng, Y. Hua, Y. M. Yang, S. Xu and P. N. Prasad, *ACS Appl. Mater. Interfaces*, 2021, **13**, 44596–44603.

218 L. Lei, Y. Wang, W. Xu, R. Ye, Y. Hua, D. Deng, L. Chen, P. N. Prasad and S. Xu, *Nat. Commun.*, 2022, **13**, 5739.

219 P. Pei, Y. Chen, C. Sun, Y. Fan, Y. Yang, X. Liu, L. Lu, M. Zhao, H. Zhang, D. Zhao, X. Liu and F. Zhang, *Nat. Nanotechnol.*, 2021, **16**, 1011–1018.

220 P. S. Kim, P. Zhang and T. K. Sham, *Langmuir*, 2004, **20**, 4690–4695.

221 L. Siller, S. Krishnamurthy, L. Kjeldgaard, B. R. Horrocks, Y. Chao, A. Houlton, A. K. Chakraborty and M. R. Hunt, *J. Phys.: Condens. Matter*, 2009, **21**, 095005.

222 W. Sun, T. Shi, L. Luo, X. Chen, P. Lv, Y. Lv, Y. Zhuang, J. Zhu, G. Liu, X. Chen and H. Chen, *Adv. Mater.*, 2019, **31**, e1808024.

223 L. Liu, T. K. Sham, W. Han, C. Zhi and Y. Bando, *ACS Nano*, 2011, **5**, 631–639.

224 S. G. Ryan, M. N. Butler, S. S. Adeyemi, T. Kalber, P. S. Patrick, M. Zaw Thin, I. F. Harrison, D. J. Stuckey, M. Pule and M. F. Lythgoe, *Sci. Rep.*, 2019, **9**, 19223.

225 R. Leo William, *Techniques for Nuclear and Particle Physics Experiments: a How-to Approach*, Springer, 1994.

226 Y. Osakada, G. Pratx, L. Hanson, P. E. Solomon, L. Xing and B. Cui, *Chem. Commun.*, 2013, **49**, 4319–4321.

227 D. Zhang, H. Zhang, X. Zhang, T. K. Sham, Y. Hu and X. Sun, *Phys. Chem. Chem. Phys.*, 2016, **18**, 6406–6410.

228 H. Chen, T. Moore, B. Qi, D. C. Colvin, E. K. Jelen, D. A. Hitchcock, J. He, O. T. Mefford, J. C. Gore, F. Alexis and J. N. Anker, *ACS Nano*, 2013, **7**, 1178–1187.

229 K. Kirakci, P. Kubát, K. Fejfarová, J. Martinčík, M. Nikl and K. Lang, *Inorg. Chem.*, 2016, **55**, 803–809.

230 D. Beke, M. V. Nardi, G. Bortel, M. Timpel, Z. Czigány, L. Pasquali, A. Chiappini, G. Bais, M. Rudolf, D. Zalka, F. Bigi, F. Rossi, L. Bencs, A. Pekker, B. G. Márkus, G. Salviati, S. E. Saddow, K. Kamarás, F. Simon and A. Gali, *Chem. Mater.*, 2021, **33**, 2457–2465.

231 M. Xin and W. H. Cao, *Guangpuxue Yu Guangpu Fenxi*, 2009, **29**, 2272–2275.

232 H. Chen, F. Wang, T. Moore, B. Qi, D. Sulejmanovic, S. J. Hwu, O. T. Mefford, F. Alexis and J. N. Anker, *J. Mater. Chem. B*, 2017, **5**, 5412–5424.

233 W. Sun, L. Luo, Y. Feng, Y. Cai, Y. Zhuang, R. J. Xie, X. Chen and H. Chen, *Angew. Chem., Int. Ed.*, 2020, **59**, 9914–9921.

234 H. Li, Z. Chen, Z. Sang, X. Zhang and Y. Wang, *RSC Adv.*, 2020, **10**, 43773–43782.

235 S. Clement, W. Deng, E. Camilleri, B. C. Wilson and E. M. Goldys, *Sci. Rep.*, 2016, **6**, 19954.

236 H. Chen, X. Sun, G. D. Wang, K. Nagata, Z. Hao, A. Wang, Z. Li, J. Xie and B. Shen, *Mater. Horiz.*, 2017, **4**, 1092–1101.

237 H. Wang, B. Lv, Z. Tang, M. Zhang, W. Ge, Y. Liu, X. He, K. Zhao, X. Zheng, M. He and W. Bu, *Nano Lett.*, 2018, **18**, 5768–5774.

238 M. Isikawa and E. Guidelli, *ACS Appl. Mater. Interfaces*, 2022, **14**, 324–336.

239 J. Liu, H. Wang, X. Yi, Y. Chao, Y. Geng, L. Xu, K. Yang and Z. Liu, *Adv. Funct. Mater.*, 2017, **27**, 1703832.

240 R. Sang, F. Deng, A. Engel, E. Goldys and W. Deng, *Biomed. Pharmacother.*, 2022, **155**, 113837.

241 Y. C. Chuang, C. H. Chu, S. H. Cheng, L. D. Liao, T. S. Chu, N. T. Chen, A. Paldino, Y. Hsia, C. T. Chen and L. W. Lo, *Theranostics*, 2020, **10**, 6758–6773.

242 Z. Li, C. Zhao, Q. Fu, J. Ye, L. Su, X. Ge, L. Chen, J. Song and H. Yang, *Small*, 2022, **18**, e2105160.

243 W. Fan, B. C. Yung and X. Chen, *Angew. Chem., Int. Ed.*, 2018, **57**, 8383–8394.

244 A. W. Carpenter and M. H. Schoenfisch, *Chem. Soc. Rev.*, 2012, **41**, 3742–3752.

245 F. Zhang, S. Liu, N. Zhang, Y. Kuang, W. Li, S. Gai, F. He, A. Gulzar and P. Yang, *Nanoscale*, 2020, **12**, 19293–19307.

246 Z. Du, X. Wang, X. Zhang, Z. Gu, X. Fu, S. Gan, T. Fu, S. Xie and W. Tan, *Angew. Chem., Int. Ed.*, 2023, **62**, e202302525.

247 K. Sarkar, S. E. Torregrossa-Allen, B. D. Elzey, S. Narayanan, M. P. Langer, G. A. Durm and Y. Y. Won, *Mol. Pharm.*, 2022, **19**, 2776–2794.

248 M. Ashokkumar, J. Lee, S. Kentish and F. Grieser, *Ultrason. Sonochem.*, 2007, **14**, 470–475.

249 D. Song, W. Xu, M. Luo, M. Zhang, H. Wen, X. Cheng, X. Luo and Z. Wang, *Nanoscale*, 2021, **13**, 14130–14138.

250 A. Sazgarnia, A. Shanei, H. Eshghi, M. Hassanzadeh-Khayyat, H. Esmaily and M. M. Shanei, *Ultrasonics*, 2013, **53**, 29–35.

251 P. Gholami, L. Dinpazhoh, A. Khataee and Y. Orooji, *Ultrason. Sonochem.*, 2019, **55**, 44–56.

252 A. Radivoievych, B. Kolp, S. Grebinyk, S. Prylutska, U. Ritter, O. Zolk, J. Glökler, M. Frohme and A. Grebinyk, *Int. J. Mol. Sci.*, 2023, **24**, 1020.

253 R. Hou, X. Liang, X. Li, X. Zhang, X. Ma and F. Wang, *Biomater. Sci.*, 2020, **8**, 2526–2536.

254 K. Kawamura, A. Ikeda, A. Inui, K. Yamamoto and H. Kawasaki, *J. Chem. Phys.*, 2021, **155**, 124702.

255 C. Xu, J. Huang, Y. Jiang, S. He, C. Zhang and K. Pu, *Nat. Biomed. Eng.*, 2023, **7**, 298–312.

256 D. Zhou, Z. Zhang, B. Qiu, D. Zhang, S. Xie, K. Huang and X. Li, *ACS Appl. Mater. Interfaces*, 2022, **14**, 26418–26430.

257 B. P. Barber, C. Wu, R. Löfstedt, P. H. Roberts and S. J. Putterman, *Phys. Rev. Lett.*, 1994, **72**, 1380.

258 F. Yang, H. Cui, X. Wu, S.-J. Kim and G. Hong, *Nanoscale*, 2023, **15**, 1629–1636.

259 Z. Zhang, H. Yan, W. Cao, S. Xie, P. Ran, K. Wei and X. Li, *ACS Nano*, 2023, **17**, 16089–16106.

This journal is © The Royal Society of Chemistry 2024

Chem. Soc. Rev., 2024, **53**, 2898–2931 | **2931**